Nanocomposite Hydrogels

Fracture Toughness
and Energy Dissipation Mechanisms

Master Thesis

by

Andrea Schmid, BSc

conducted at

Materials Science and Testing of Polymers at
Montanuniversität Leoben, Austria
School of Mechanical, Materials & Mechatronic Engineering at
University of Wollongong, Australia

supervision:	Ass.-Prof. Dipl.-Ing. Dr.mont. Katharina Resch, Dr. Philip Whitten
appraisal:	Univ.-Prof. Dr. Dipl.-Ing. Dr.mont. Gerald Pinter

Wollongong/Leoben, November 2013

AFFIDAVIT

I declare in lieu of oath, that I wrote this thesis and performed the associated research myself, using only literature cited in this volume.

EIDESSTATTLICHE ERKLÄRUNG

Ich erkläre an Eides statt, dass ich diese Arbeit selbstständig verfasst, andere als die angegebenen Quellen und Hilfsmittel nicht benutzt und mich auch sonst keiner unerlaubten Hilfsmittel bedient habe.

WOLLONGONG/LEOBEN, November 2013 **(Andrea Schmid)**

ACKNOWLEDGEMENTS

My profound appreciation goes towards Univ.-Prof. Dipl.-Ing. Dr.mont. Gerald Pinter (Montanuniversität Leoben) and Prof. Rian Dippenaar (University of Wollongong) for not only rendering it possible but making it so uncomplicated for me to conduct the research for my thesis in Australia whilst submitting it at my home university.

I owe my gratitude to the University of Wollongong for allowing an internal grant which enabled me to perform my research in Australia. Likewise, I express my appreciation to the Engineering Materials Institute for their generous scholarship. In addition, I acknowledge the use of facilities and assistance of Tony Romeo and David Mitchell at the UOW Electron Microscopy Centre and the use of facilities at the University of Newcastle.

Many thanks to my Australian supervisor Dr. Philip Whitten. His enthusiasm and thirst for knowledge inspired and motivated me. Reminiscing about my time of research in Australia many discussions come to my mind that challenged and enriched my thoughts.

Furthermore, I express my deepest gratitude towards Ass.-Prof. Dipl.-Ing. Dr.mont. Katharina Resch, my Austrian supervisor. Her never-ending endorsement and reassurance always escorted me!

My dear colleagues Kel, Noel, David and Thomas: Thank you so much for creating a simply awesome atmosphere in the labs! I enjoyed working next to you every day and will never forget your positive attitude. You taught me that even in the seemingly worst result of an experiment there is something positive and always something to learn from.

Dear Mama and Papa: Thank you for your endless help and encouragement throughout all my life and for always letting me know that I can rely on you! Many thanks to my siblings Christian, Johanna and Thomas for being there for me without exception. Thomas, you are and will always be a role model for me – thank you for showing me what is really important in life!

My heartfelt gratitude goes towards my fiancé, Thomas. I cannot say more than a simple 'Thank you!' for making my life so wonderful!

To everyone who contributed to this amazing, unforgettable experience in Australia: CHEERS !

ABSTRACT

Traditional hydrogels consist of organically cross-linked polymer networks that contain a high fraction of water. Due to extraordinary characteristics including outstanding transparency as well as superior swelling and de-swelling properties, they are attractive for diverse biomedical applications such as soft contact lenses. However, implementation in more sophisticated purposes such as artificial muscles or synthetic mammal tissue is limited by poor mechanical properties, in particular low fracture toughness. Substitution of organic cross-linkers by clay, a multifunctional, inorganic cross-linker results in nanocomposite hydrogels. These materials exhibit high tensile strength combined with high elongation-at-break as well as high compliance while retaining the remaining unique characteristics of hydrogels. Yet, tearing toughness of nanocomposite hydrogels has not yet been studied systematically and extensively. Therefore, the overall objective of this study was to quantify the toughness and identify active mechanisms for dissipation of energy of nanocomposite hydrogels.

Nanocomposite hydrogels were prepared by employing synthetic clay of type hectorite and monomer *N-N*-dimethylacrylamide and allowing in-situ free radical polymerization. Sample variables were clay content as well as sample thickness. For comparison also a traditional hydrogel was prepared employing *N,N′*-Methylenebis(acrylamide) as organic cross-linker.

Sample preparation was validated by different morphological characterization techniques. The exfoliation of clay into disk-shaped nanoparticles and homogeneous distribution was confirmed by X-ray diffractometry and transmission electron microscopy. Thermogravimetric analysis verified the high water content of the prepared hydrogels. Infrared spectroscopy confirmed similar polymerization processes for all hydrogels except the nanocomposite hydrogel with the smallest thickness. This is probably due to an incomplete polymerization process for this sample.

Tensile testing proved extraordinarily high values for strain-at-break for nanocomposite hydrogels beyond the crosshead travel’s limit (strain-at-break greater than 1250 %) while traditional hydrogels exhibited brittle behaviour. Storage Modulus, Shear Modulus and the number of network chains between cross-links per unit volume were derived. All these parameters increased with increasing clay content. In comparison to traditional hydrogels nanocomposite hydrogels exhibited a less stiff behaviour including a significantly higher elongation-at-break. Traditional hydrogel's material behaviour followed Rubber Elasticity Theory. However, no suitable theory describing nanocomposite hydrogel's material behaviour could be found. This might be due to the complex structure of the inorganic/organic network and the complicated interactions between clay and polymer.

Fracture toughness was determined by employing the pure shear test approach. Organically cross-linked hydrogels could not be tested due to their fragility. In contrast, nanocomposite hydrogels could quickly dissipate large amounts of energy. Extraordinarily high fracture toughness values were determined for nanocomposite hydrogels. One dissipation mechanism that was observed was pronounced blunting of the crack tip. In order to detect further dissipation mechanisms, viscoelastic properties were characterized. Step cycle testing revealed that for low to moderate true strains the ratio between elastic and plastic strain remained widely constant. However, at a certain strain, plastic strain almost completely dominated the deformation behaviour. Thus plastic deformation is presumably large in the whole sample and also close to adjacencies of a crack tip if a crack is present. Stress relaxation experiments revealed a stress relaxation time (the time at which maximal viscoelastic dissipation occurs) similar to the time necessary to rupture samples in fracture toughness tests. Thus, viscoelastic dissipation accounts for high fracture energies. Viscoelastic dissipation was additionally confirmed by dynamic mechanical analysis and rheometry measurements.

Hence, investigations revealed different mechanisms contributing to the high fracture toughness of nanocomposite hydrogels. Firstly, blunting prevents expansion of existing cracks. Secondly, plastic deformation provides absorption of energy. Thirdly, viscoelastic dissipation contributes to the superior fracture toughness.

KURZFASSUNG

Traditionelle Hydrogele bestehen aus organisch vernetzten Polymer-Netzwerken, welche einen hohen Wasseranteil beinhalten. Aufgrund außergewöhnlicher Charakteristiken wie hervorragender Transparenz und ausgezeichneten Quelleigenschaften sind diese für unterschiedlichste biomedizinische Anwendungen wie beispielsweise weiche Kontaktlinsen attraktiv. Die Anwendung dieser Materialien in Zukunftstechnologien wie etwa für künstliche Muskeln oder synthetisches, menschliches Gewebe ist derzeit aufgrund ungenügender mechanischer Eigenschaften, im Speziellen der niedrigen Bruchzähigkeit, limitiert. Durch Substituierung des organischen Vernetzers mit Clay, einem multifunktionellen, inorganischen Vernetzer, werden so genannte nanocomposite Hydrogele erhalten. Diese Materialien weisen eine hohe Zugfestigkeit in Kombination mit hoher Bruchdehnung sowie hohe elastische Nachgiebigkeit auf, während sie sämtliche übrigen einzigartigen Charakteristiken von Hydrogelen beibehalten. Über die Bruchzähigkeit von nanocomposite Hydrogelen liegen derzeit noch keine systematischen und umfangreichen Untersuchungen vor. Dahingehend sind die Hauptziele dieser Forschungsarbeit die quantitative Erfassung der Zähigkeit wie auch die Identifizierung von Mechanismen zur Dissipation von Energie der nanocomposite Hydrogele.

Nanocomposite Hydrogele wurden unter Einsatz von synthetischem Clay des Types Hektorit und von *N-N*-Dimethylacrylamid als Monomer hergestellt, wobei eine in-situ freie radikalische Polymerisation durchgeführt wurde. Variable Parameter waren dabei der Clay-Gehalt sowie die Probendicke. Um einen direkten Vergleich unterschiedlicher Hydrogel-Typen zu ermöglichen, wurde weiters ein traditionelles Hydrogel mit *N,N'*-methylenbis(acrylamid) als organischem Vernetzer hergestellt.

Die Probenherstellung wurde durch unterschiedliche morphologische Charakterisierungstechniken verifiziert. Das Abblättern von Clay in scheibenförmige Nanoteilchen und deren homogene Verteilung wurde durch Röntgendiffraktometrie und Transmissionselektronenmikroskopie nachgewiesen. Thermogravimetrische Analysen zeigten den hohen Wassergehalt der hergestellten Hydrogele auf. Infrarot-Spektroskopie bestätigte ähnliche Polymerisationsprozesse für alle Hydrogele mit Ausnahme für jenes mit der geringsten Dicke. Dies wird auf eine unvollständige Polymerisation dieser Probe zurückgeführt.

Zugversuche ergaben außergewöhnlich hohe Werte für die Bruchdehnung der nanocomposite Hydrogele (Bruchdehnungen von über 1250 %), die außerhalb des Limits des

Traversenweges der Zugprüfmaschine lagen. Im Gegensatz dazu zeigte das traditionelle Hydrogel ein sprödes Materialverhalten. Elastizitätsmodul, Schubmodul und die Anzahl der Netzwerkketten zwischen Netzpunkten pro Volumeneinheit wurden abgeleitet. Sämtliche dieser Parameter nahmen mit steigender Clay-Konzentration zu. Das Materialverhalten von traditionellen Hydrogelen wurde mit der so genannten Rubber Elasticity Theory beschrieben. Das Materialverhalten von nanocomposite Hydrogelen war mit keiner Theorie ideal beschreibbar. Dies ist vermutlich auf die komplexe Struktur des inorganisch/organischen Netzwerkes und die komplizierten Wechselwirkungen zwischen Clay und Polymer zurückzuführen.

Die Bruchzähigkeit wurde unter Anwendung von bruchmechanischen Schubversuchen ermittelt. Traditionelle Hydrogele konnten aufgrund ihrer Fragilität nicht getestet werden. Demgegenüber dissipierten nanocomposite Hydrogele sehr schnell große Mengen an Energie. Dadurch ergaben sich außergewöhnlich hohe Bruchzähigkeiten. Ein Dissipationsmechanismus war das ausgeprägte Abstumpfen der Rissspitze. Um weitere Dissipationsmechanismen zu identifizieren, wurden die viskoelastischen Eigenschaften charakterisiert.

Zyklische Stufenversuche ergaben ein weitgehend konstantes Verhältnis zwischen elastischer und plastischer Dehnung für niedrige und moderate wahre Dehnungen. Allerdings dominierte ab einer gewissen Dehnung der plastische Anteil klar das Deformationsverhalten. Daher ist davon auszugehen, dass plastische Deformation in der ganzen Probe sowie in der Umgebung der Rissspitze eines vorhandenen Risses stattfindet.

Spannungsrelaxationsversuche ergaben eine Spannungsrelaxationszeit (die Zeit, bei welcher maximale viskoelastische Dissipation auftritt) ähnlich der Versagenszeit in Bruchzähigkeitsversuchen. Daher kann angenommen werden, dass viskoelastische Dissipation signifikant zur Bruchzähigkeit von nanocomposite Hydrogelen beiträgt. Dies wurde weiters mittels dynamisch-mechanischer Analyse und Rheometrie-Messungen bestätigt.

Folglich zeigten Untersuchungen in dieser Forschungsarbeit unterschiedliche Mechanismen, die zur hohen Bruchzähigkeit von nanocomposite Hydrogelen beitragen. Erstens verhindert das Abstumpfen der Rissspitze die Ausbreitung von existierenden Rissen. Zweitens bietet plastische Deformation die Absorption von Energie. Drittens trägt viskoelastische Dissipation zu der überlegenen Bruchzähigkeit von nanocomposite Hydrogelen bei.

TABLE OF CONTENTS

CONTENTS OF GRAPHS

1 INTRODUCTION AND OBJECTIVES

Hydrogels consist of polymer networks that contain a high fraction of water. Typically, the solvated polymer network chains are covalently linked by organic cross-linkers. In many fields of our everyday life, hydrogels have become essential due to their unique characteristics. For instance their high water absorptive capacity makes them ideal for applications such as wound dressings and incontinence pads whilst their combination of permeability to moisture and oxygen with transparency is exploited in soft contact lenses. Further applications include water retention in agriculture, a carrier for drug delivery and pesticides and membranes for waste recovery and filtration. Many hydrogels are environmentally sensitive, i.e. their water content and hence size is dependent on temperature, humidity and pH of their environment. This makes them highly attractive for stimuli-response biomedical applications, as their compliance is similar to mammal tissue. Potential future applications include artificial muscles, synthetic mammal tissue and low friction bearings. However, for realising these applications further development is necessary, as conventional hydrogels are inherently fragile. The polymer is well above its glass transition with the solid being highly elastic. As there is no mechanism for significant non-elastic dissipation of energy, conventional hydrogels are susceptible to minor cracks and flaws and exhibit brittle failure.

The fragility of hydrogels limits their employment. Hence, there is strong motivation to produce tough hydrogels so that their unique combination of high compliance and high water content can be exploited. One successful synthetic approach to tough hydrogels is the substitution of traditionally organic cross-linkers employed in conventional hydrogels with inorganic cross-linkers.

It has been found that the application of clay as inorganic cross-linker leads to nanocomposite hydrogels that exhibit extraordinary characteristics including outstanding transparency, superior swelling and deswelling properties, high tensile strength combined with high elongation-at-break as well as high compliance. In contrast to organically cross-linked hydrogels the inorganic (clay)/organic (polymer)-network is formed by physical bonds. Nanocomposite hydrogels are known to exhibit a large area under their stress-strain curves. However, tearing toughness of nanocomposite hydrogels has not yet been studied systematically and extensively. Therefore, the overall objective of this study is to quantify the toughness and identify active mechanisms for dissipation of energy of nanocomposite hydrogels. Additionally, properties of nanocomposite hydrogels shall be compared to conventional hydrogels.

Focus is on developing a practical procedure for preparing nanocomposite hydrogels composed of monomer *N,N*-dimethylacrylamide (DMAA) and Laponite XLS®, acting as synthetic inorganic cross-linker. Samples of different thickness and different clay content shall be produced. Verification of sample preparation in terms of ensuring sufficient polymerization conditions and uniform distribution of clay platelets shall be performed by microscopy (transmission electron microscopy), Fourier-Transformation Infrared Spectroscopy and X-Ray Diffractometry. Moreover, focus is on comprehensive and systematic characterization of mechanical properties. In particular, low strain tensile testing and tearing toughness tests shall be conducted. It is assumed that nanocomposite hydrogels take a unique position in an Ashby-Plot displaying Young's Modulus and fracture toughness. As a consequence, the verification of the presumption of high fracture energy values shall be one of the key aspects of this study. The pure shear test approach shall be employed to quantify the toughness. Furthermore, the extent of viscoelastic and plastic deformation during deformation of nanocomposite hydrogels shall be surveyed. Visco-elasticity shall be characterized at slow time scales by stress relaxation experiments and by fast time scales by dynamic-mechanical analysis. Plastic deformation is characterized by step cycle testing.

2 FUNDAMENTALS

2.1 Polymeric Hydrogels

A gel can be classified as material in a state in between liquid and solid (Okay, 2010) or as 'solid-like' (Almdal et al., 1993). The application temperature is well above their glass transition temperature T_g. Additionally, the materials show a rubber-like elasticity. Gels consist of polymer networks (either physically or chemically cross-linked) that have been swollen by a solvent. Swelling has a high influence on mechanical properties of the gel. By nature, swelling is followed by a decrease of the number of network chains per unit cross-sectional area. As a consequence few polymer chains have to be ruptured to allow crack propagation. Furthermore, viscoelastic energy dissipation is diminished due to separation of the network (Naficy et al., 2011). Thus, conventional gels exhibit a brittle appearance accompanied by low fracture energies. Depending on the solvent in consideration gels can be classified. Examples are organogels, aerogels and hydrogels. Organogels are formed by employing an organic solvent. They are commonly used for organic pollutant adsorptions (Maatar et al., 2013). Oleogels are a special type of organogels where the solvent is an edible solvent, e.g. virgin olive oil (Lupi et al., 2013). Developments in this field aim to replace saturated fats in food industry by oleogels. Aerogels are formed by replacing any liquid solvent in a gel by air or another gas. This leads to an extremely low density (between 0.0011 to ~0.5 g/cm^3). It shall be remarked that aerogels can not only be formed by applying a polymer network as 'frame' but also by substituting the polymer by other materials (aerogel.org, 2006). Hydrogels employ water as solvent and are topic of discussion in the following paragraphs.

Hydrogels contain a three-dimensional porous network structure that enables them to carry a high fraction of water whilst remaining a solid. This is due to hydrophilic functional groups that bond water by establishing hydrogen bonds which also give them the name 'hydrophilic gels'. The polymer network is traditionally formed by employing organic cross-linkers ('traditional hydrogels', 'organically cross-linked hydrogels'). As a consequence, covalent intermolecular bonds are formed between the individual polymer chains. Organic cross-linkers typically exhibit a low functionality, typically of four. Therefore only few polymer chains can be linked by one cross-linker. If (due to an external load) a polymer chain breaks, its load is transferred to those few other chains resulting in greatly increasing their load which makes them likely to fail presently, too. The evident result is brittle behaviour of traditional hydrogels. Figure 2.1 a) schematically illustrates a conventional hydrogel. The orange dots represent cross-links. Due to the low functionality of cross-linkers only few chains are connected at each cross-link. Figure 2.1 b) displays the effect of an external tensile stress. Stretching results in rupturing of chains (marked with blue circles) that cannot be compensated by other chains.

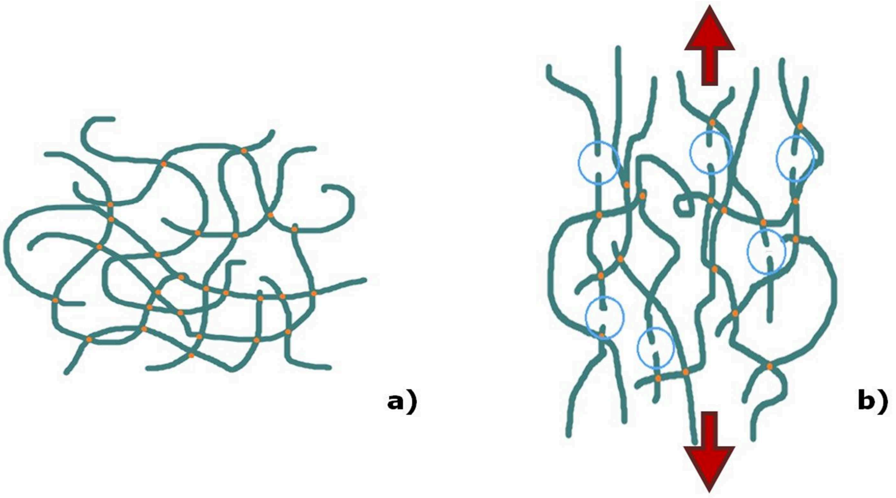

Figure 2.1: a) Schematic structure of conventional hydrogel **b)** same hydrogel under tension with rupturing chains.

As all polymer chains are connected, this type of hydrogel (in contrast to the double-network hydrogels discussed later on) can be regarded as a single molecule on the macroscopic scale (Okay, 2010). Representatives for hydrogels are those based on acrylamide type monomers such as poly(acrylamide) and poly(N-isopropylacrylamide). A common organic cross-linker is N,N'-Methylenebisacrylamide (BIS).

Hydrogels present extraordinary swelling and deswelling properties. It is reported that some hydrogels are able to absorb up to 500 times their dry weight in water and – dependent on their surrounding's humidity – slowly release it again (2009). Another key feature is that they are soft and flexible (Huang et al., 2004) and often follow the Simple Rubber Elasticity Theory which is explained in more detail in subchapter 2.2.1. The Young's Modulus typically ranges between 10^{-2} and 10^{1} kPa, depending on the cross-linker density and the degree of dilution of the monomer (Okay, 2010). Tensile strain-at-break is usually found below 30 %. Many hydrogels are extremely environmentally sensitive, i.e. they react to changes in temperature, pH-value and humidity by swelling or deswelling. Following this they are predominantly used in medical applications, e.g. in drug release systems, as carriers for proteins, as contact lenses (Li et al., 2009a) as well as matrices for repairing tissue (Hoemann et al., 2005; Hoffman, 2002; Linnes et al., 2007; Sun et al., 2012) and in particular for cell proliferation (Wu et al., 2008). Other applications include wound dressing (Linnes et al., 2007), agricultural tasks (Kasgoz et al., 2012) and chemical sensors and actuators (Guenther et al., 2007). Additionally they are used as carriers for nucleic acid in gel electrophoresis and refrigerants (Haraguchi and Li, 2006). The major utilization at the moment is their application as super absorbent materials, as for disposable diapers and absorbents for environmental spills.

Until now applications are limited due to hydrogels low mechanical properties. A particularly problematic attribute for many applications is the fragility of traditional hydrogels. In addition it has been found that traditional hydrogels exhibit the so called 'spatial gel inhomogeneity' which means that the cross-link density is heterogeneous. This inhomogeneity is predicted to lead to undesired properties. An example is the exhibition of an optical haze which is problematic regarding applications like contact lenses (Shibayama, 1998). A further disadvantage is the poor thermal stability of hydrogels (Shi Z. et al., 2011). Future applications which require an increase in properties such as fracture toughness include cell cultivation on their surface (Haraguchi et al., 2006), artificial muscles (Hellweg et al., 2000) and artificial articular cartilage (Gong et al., 2003). Other implementations could include colloid crystals (Hellweg et al., 2000) and photo responsive gels (Akashi et al., 2002). Supplementary improvement in the field of drug releasing materials (Dai et al., 2006; Lee and Fu, 2003) is desired. Therefore research aims at modifying hydrogels in order to retain the characteristic features given above whilst strengthen their toughness. In doing so, next to so called double-network hydrogels and topological gels, nanocomposite hydrogels are being developed. An Ashby Plot in Figure 2.2 compares mechanical properties (Young's Modulus and fracture toughness) of different types of hydrogels. Other material classes such as reinforced plastics, rubbers and plastics as well as metals and glasses are included in the diagram. Nanocomposite hydrogels under consideration in this thesis are believed to be close to the bubble representing double-network hydrogels regarding fracture toughness but possibly lower in Modulus. The uniqueness of this position in the Ashby Plot is a major motivation for development of nanocomposite hydrogels.

The following subchapters will review enhancements of traditional hydrogels in more detail. Initially, double-network hydrogels will be discussed. Thereafter, nanocomposite hydrogels will be discussed thoroughly.

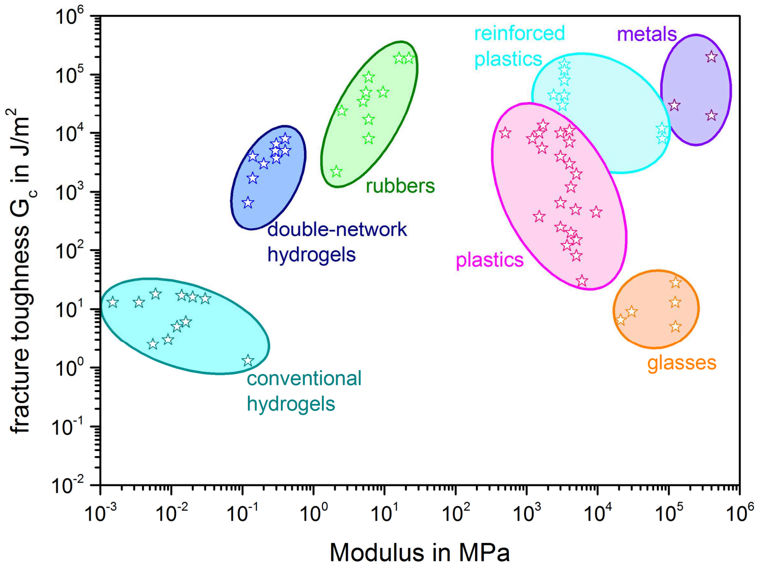

Figure 2.2: Ashby plot comparing fracture energy and Modulus of several material classes with a focus on types of gels in the style of (Naficy et al., 2011).

2.1.1 Double-Network Hydrogels

Double-network hydrogels consist of hydrophilic polymers. They exhibit two inter-penetrating networks (both organically cross-linked) that strengthen one another. Apart from entanglements the networks are independent from each other (Li et al., 2013). The combination of poly(2-acrylamido-2-methylpropanesulfonic acid) and poly(acrylamide) serves as an example (Gong et al., 2003). Other polymers used for the preparation of double-network hydrogels include poly(*N*-*N*′-dimethylacrylamide) and poly(2-hydroxyethyl methacrylate) as well as natural polymers such as collagen.

If the molar ratio of the two networks is chosen correctly (that means for the exemplary combination given above a ratio of roughly 1:20), the unification of the two networks is reported to give greatly higher mechanical properties than the single networks. Gong et al. (2003) for instance presents a double-network hydrogel exhibiting a tensile strength of 680 kPa and a stress-at-break under compression of almost 20.000 kPa. Storage Moduli between 80 kPa and 230 kPa have been reported (Fei et al., 2013). In comparison with traditional hydrogels these values are extraordinarily high. Next to the molar ratio, a ‘good’ cross-linking density is crucial to enhance mechanical properties. The first network is required to be highly cross-linked and therefore being comparativley rigid, while the second one is demanded to be loosely cross-linked and therefore being comparatively flexible (Hattori et al., 2013). High fracture energies of 100 J/m^2 to 1000 J/m^2 found for double-network hydrogels are due to their ability to create a large plastic zone by reallocating the stress to one of the networks (Seitz et al., 2009). As a consequence, there is a substantial increase in the number of covalent bonds required for rupture. In order to rupture one bond of the first network, several bonds in the second network have to rupture first.

2.1.2 Nanocomposite Hydrogels

In contrast to traditional hydrogels, nanocomposite hydrogels do not contain any organic cross-linkers. Instead, inorganic cross-linkers (most commonly clay) act as multifunctional cross-linkers (Okay, 2010) which results in a unique inorganic (usually clay) / organic (polymer)-network structure. A key difference to organically cross-linked hydrogels is that the cross-links consist of physical bonds (hydrogen bonds) instead of chemical bonds. Until now, several different combinations of monomer and clay are being developed to prepare nanocomposite hydrogels. The following paragraphs discuss different combinations of materials used for preparing nanocomposite hydrogels. Additionally a review on their characteristics and applications is given.

As far as known, the research group around Haraguchi has firstly successfully produced nanocomposite hydrogels (Haraguchi and Takehisa, 2002). Their aim has been the overcoming of weak mechanical properties in hydrogels in order to allow applications such as drug release agents, artificial muscles and cell cultivation as described above. Firstly, the composition of nanocomposite hydrogels consisting of derivatives of *N*-alkylacrylamide such as *N*-isopropylacrylamide (NIPA) as monomer and synthetic hectorite as clay has been proposed. In comparison to chemically cross-linked hydrogels of the same type, both homogeneity in structure and mechanical properties are significantly improved (Haraguchi and Takehisa, 2002). Secondly, NIPA and Laponite XLG® which is a certain type of synthetic hectorite has been employed to study effects of cross-linker content on mechanical properties. Tensile strength increases while the elongation-at-break decreased marginally with increasing clay content (Haraguchi et al., 2002). Thirdly, further effects of compositional modifications such as the polymer content on mechanical properties have been analysed. It is proposed that monomer content equals polymer content in the prepared nanocomposite hydrogel. For this study monomer NIPA has been replaced by *N,N*-dimethylacrylamide (DMAA). Both strength and Modulus are proportional to clay content and several mechanical properties are dependent on the polymer content (Haraguchi et al., 2003). Fourthly, it has been attempted to even further increase mechanical properties by increasing the clay content up to 25 mole% in 1 L of water.

Materials in use for this study have been NIPA and Laponite XLG®. A Young's Modulus of 1.100 kPa is accompanied by tensile strength of 453 kPa (Haraguchi and Li, 2006). Fifthly, the formation of the proposed physical network has been studied. By doing so it has also been shown that the only possible preparation method to generate nanocomposite hydrogels is in-situ free polymerization (Haraguchi et al., 2005). Sixthly, it has been attempted to culture cells on nanocomposite hydrogels consisting of NIPA or DMAA with Laponite XLG®. In contrast to corresponding chemically cross-linked hydrogels cell-cultivation is possible and independent of the present gel thickness. Accordingly this type of hydrogel is proposed for use in culture dishes and cell sheet engineering (Haraguchi et al., 2006). Further, NIPA and DMAA have successfully been prepared into the shape of several different geometries (Haraguchi, 2007). Self-healing of nanocomposite hydrogels consisting of the materials as given above is reported (Haraguchi et al., 2011). Swelling and deswelling characteristics are analysed and discussed. Addition of sodium ions into the network yields a reversibility in the swelling behaviour rather than irreversibility as usually present (Ren et al., 2011).

Following Haraguchis approach, several other research groups have attempted to improve hydrogels' properties, in particular mechanical properties such as tensile strength and elongation-at-break by producing nanocomposite hydrogels. Applications for proposed nanocomposite hydrogel systems are kept general and are in accordance with potential future applications as given above (Wang et al., 2011).

In order to simplify sample preparation, substitution of Laponite XLG® by Laponite XLS®, a surface-modified hectorite type that does not gel up to concentrations higher that can be reached with Laponite XLG®, has been proposed. The monomer utilized has been NIPA. Hence a further increase of clay content yielding tensile strength of 1.000 kPa is submitted (Liu et al., 2006). The same attempt has been proposed with acrylic acid (AA) as monomer resulting in good mechanical properties and improved swelling behaviour (Li et al., 2009a). So as to cheapen the material costs substitution of Laponite by a different type of hectorite (Lvjie trademark) or montmorillonite type G-105 has been suggested. Montmorillonite type G-105 is not suitable for nanocomposite hydrogel preparation but the alternative hectorite type yields either similar or better mechanical and swelling properties than Laponite (Zhang et al., 2009). Additionally studies to evaluate different monomers have been performed. When using Laponite XLS® as clay the utilization of either DMAA or NIPA as monomer gains larger Elastic Moduli than the utilization of acrylamide (AAm). On the same material combinations effects of the interaction between clay and monomer have been studied. Furthermore the existence of a physical network in the materials under consideration is confirmed (Abdurrahmanoglu et al., 2008). The system Laponite XLS® with a co-monomer of AAm and dimethylaminoethyl methacrylate has been employed to study effects of polymerization initiation. UV-initiation provides nanocomposite hydrogels with better mechanical properties (including elongation-at-break greater than 1000 %) than redox initiation (Zhu et al., 2010). Furthermore the effect of the type of initiator has been studied by comparing potassium persulfate (KPS) and Azo-bis(*iso*-butyronitrile) (AIBN) in the combination of DMAA and Laponite XLG®. Hydrogels prepared with AIBN result in better mechanical properties than those prepared with KPS (Wang et al., 2011). Combination of AAm with Laponite XLS® with particularly high clay contents yields elastic recovery of more than 96 %, elongation-at-break of 2500 % and low elastic hysteresis of less than 20 % (Zhu et al., 2006). So as to improve the response rate AAm and Laponite RD and RDS have been employed. The gained nanocomposite hydrogels yield elongations-at-break higher than 4000 % (Xiong et al., 2008) next to the desired faster response rate. A different development suggests the combination of NIPA with both Laponite XLG® and poly ethylene glycol (PEG). The amount of PEG can control mechanical and swelling properties of the gained nanocomposite hydrogels (Hu et al., 2009). Similar to that, AAm in combination with PEG, sodium montmorillonite as well as organically modified montmorillonite have been prepared. As a consequence swelling values up to 700 % in combination with good mechanical strength are exhibited (HelvacIoğlu et al., 2011). Furthermore a comparison between AAm in combination with Laponite RDS® or in combination with *N,N-(*methylene)di(acrylamide) (a chemical cross-linker) or with both of the mentioned has been performed. The resulting nanocomposite hydrogels are significantly tougher when containing Laponite RDS® (Okay and Oppermann, 2007). An investigation regarding effects of clay geometry has been carried out employing propane sulfonic acid (AMPS)-Aam copolymers. The clays under consideration have been montmorillonite, mica and halloysite. Montmorillonite yields higher mechanical strength than mica and halloysite (Kasgoz et al., 2012). Organophillic montmorillonite in the combination with AA leads to nanocomposite hydrogels with good thermal stability up to temperatures of 400 to 475 °C (Shi Z. et al., 2011).

Some investigations that particularly aim at the development of materials applicable in the biomedical sector are compiled in the following paragraph. The combination of AAm with Laponite XLS® has been investigated regarding swelling behaviour and adsorption properties. They exhibit a removal efficiency of more than 90 % regarding the adsorption of cationic dye. Applications exploiting this characteristic are not limited by the removal of dye waste but also include disposable diapers, amendments in greening and agriculture and sanitary napkins (Li et al., 2009b). Resulting from a favoured improvement of stimuli-sensitive hydrogels the preparation of a network consisting of poly((2-hydroxyethyl methacrylate)-co-(ethylene glycol methyl ether methacrylate)-co-(methacrylic acid)) and fibrillar attapulgite acting as inorganic cross-linker has been performed. This system has a greater equilibrium-swelling ratio as well as a higher response rate than corresponding chemically cross-linked hydrogels. Additionally, mechanical properties are improved. Potential applications include tissue engineering (Xiang et al., 2006). Moreover, biodegradable nanocomposite hydrogels have been developed employing Laponite XLG® in the combination with poly(trimethylene carbonate)–poly(ethylene glycol)–poly(trimethylene carbonate) macromonomers. Following this, an increase in toughness is present. This leads to potential applications as matrices for cell encapsulation as well as scaffolding structures (Sharifi et al., 2012). The attempt of developing nanocomposite hydrogels that can be shaped by processes such as injection moulding or compression moulding without loss of mechanical properties has resulted in the preparation of a system consisting of DMAA and 2-(Nethylperfluorooctane sulfonamido)ethyl acrylate (FOSA). FOSA has been shown to build nanodomains which results in material properties that allow melt processing. Applications include injectable drug delivery systems and contact lenses (Hao and Weiss, 2011). The following three investigations aim to develop controlled drug release systems. Firstly, poly-NIPA-co-allylamine (PNIPAM-co-allylamine) acting as nanoparticle in combination with PNIPAM-co-(acrylic acid) (PNIPAM-co-AA) allows temperature controlled release of drugs while exhibiting good mechanical properties (Huang et al., 2004). Secondly, when organic montmorillonite acts as cross-linker in the combination with monomer NIPA, the swelling ratio and as a consequence the drug release behaviour can be controlled by cross-linker content (Lee and Fu, 2003). Thirdly, an improvement in response rate is achieved by introducing porosity into a network. The applied materials have been monomer NIPA and cross-linker Laponite XLG®. Porosity is caused by the additional component calcium carbonate (Ma et al., 2008).

Furthermore nanocomposite gels have been developed by using other inorganic cross-linkers than clay. These include TiO_2, CdS, Au and Ag nanoparticles as well as carbon nanotubes and graphene (Das et al., 2012).

As a resume, it can be stated that nanocomposite hydrogels exhibit extraordinary mechanical, optical, as well as swelling and de-swelling properties. An increase in clay content leads to an increase of energy dissipation properties, making the gels tougher (Okay and Oppermann, 2007). Haraguchi (2002) reports strains-at-break at around 1000 % and tensile stresses of 50 to 350 kPa. The Elastic Modulus of between 1 and 25 kPa is low in comparison to double-network hydrogels while fracture toughness is predicted to be high as the work of extension is high (Haraguchi and Li, 2006; Naficy et al., 2011).

The proposed mechanism of how the inorganic/organic network is being created is described in the following subchapter.

2.1.2.1 Mechanism of Forming Clay-Nanocomposite Hydrogels with an inorganic/organic Network Structure

Figure 2.3 gives a schematic illustration of the forming mechanism of nanocomposite hydrogels. It displays how accelerator and initiator enable the monomer to graft to the clay platelets. Attachment of the former to the clay platelets is indicated by the change of colour of clay platelets. The last forming step (Figure 2.3 right) shows chain growth and entanglement of chains, leading to a network structure.

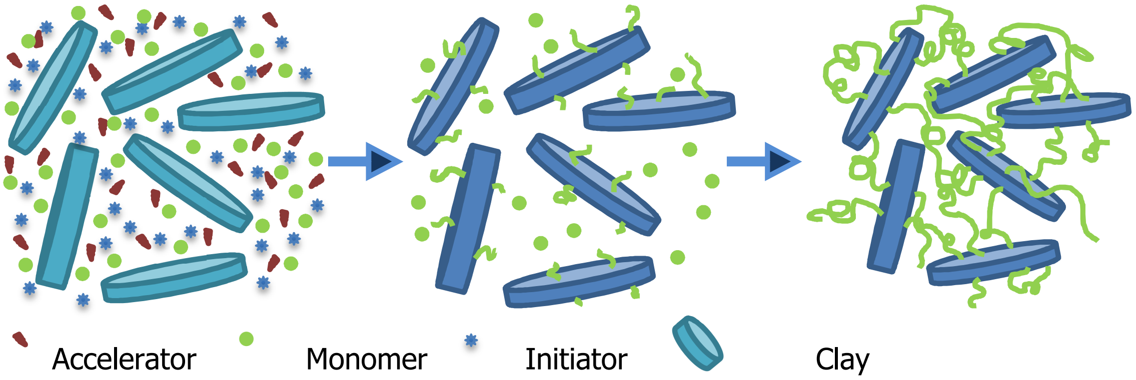

Figure 2.3: Schematic illustration of forming mechanism of inorganic/organic network; in the style of (Zhu et al., 2006).

Focus of this study as well as in literature is laid on nanocomposite hydrogels where hectorite, inorganic synthetic clay, is employed as multifunctional cross-linker. This is because hectorite seems to allow for the most desirable properties in resulting nanocomposite hydrogels when compared with other inorganic cross-linkers. However, it is not yet fully understood why hectorite functions so well as multifunctional cross-linker in nanocomposite hydrogels. Moreover, hectorite offers economic advantages over other inorganic nanoparticles such as gold. Dispersion of hectorite leads to its exfoliation into platelets with a thickness of approximately 1 nm and a diameter of approximately 25 nm

(Okay, 2010). Adding of initiator and accelerator followed by in-situ free radical polymerization results in an inorganic/organic network structure. The individual steps on how this is achieved are discussed in the following paragraphs in more detail.

Liu et al. (2006) reported that standard synthetic hectorite exhibits negatively charged surfaces and positively charged edges after exfoliation in water. It is proposed that this charge distribution leads to the formation of a 'house-of-card'-structure as shown in Figure 2.4 above. As a consequence, raised concentrations (2 wt%) of this type of clay in water lead to gel-like dispersions. Hence, it is suggested to replace standard hectorite with a surface-modified type when higher clay contents are requested. The modification changes the edges' charge from positive to negative by adhesion of an anionic poly-electrolyte. As a result, single clay platelets exhibit the same charge all over their surface which leads to electrostatic repulsion and prevents formation of a gel at moderate clay contents. Figure 2.4 (below) illustrates this behaviour.

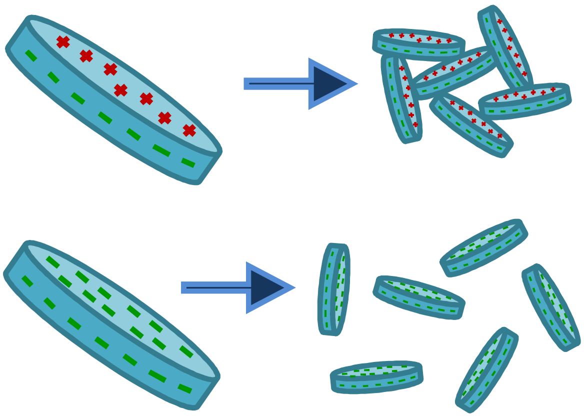

Figure 2.4: Clay exfoliation for standard hectorite **(above)** and surface-modified hectorite **(below)**; in style of (Liu et al., 2006).

The underlying polymerization technique to attain clay-nanocomposite hydrogels is in-situ free radical polymerization. It is currently the subject mechanism to synthesize polymers and is classified as addition polymerization process. One of the reasons is the simplicity of the mechanism, another is the low susceptibility to impurities compared to step growth polymerization. Even so it is vulnerable to oxygen influence as will be discussed later in this subchapter. The polymerization process involves three stages which are initiation, chain propagation and termination.

As the name suggests, free-radical polymerization is initiated by radicals. Radicals are molecules with an unpaired electron. This causes them to exhibit a high reactivity in order to gain an electron from another molecule. Radicals are often formed by the decomposition of initiators possessing a peroxo group (peroxide group) as the oxygen-oxygen bond is unstable and can – under the influence of UV-radiation, temperature or an accelerator – be split into two radicals. It is reported that the initiator potassium peroxydisulfate (potassium persulfate, molecular formula $K_2S_2O_8$, short KPS), a common initiator in free-radical polymerization, decomposes to a radical which possesses one radical and one ionic end. Figure 2.5 displays the initiator (Figure 2.5 a)) and its decomposition (Figure 2.5 b)). Decomposition can be initiated either by temperature or by the use of an accelerator.

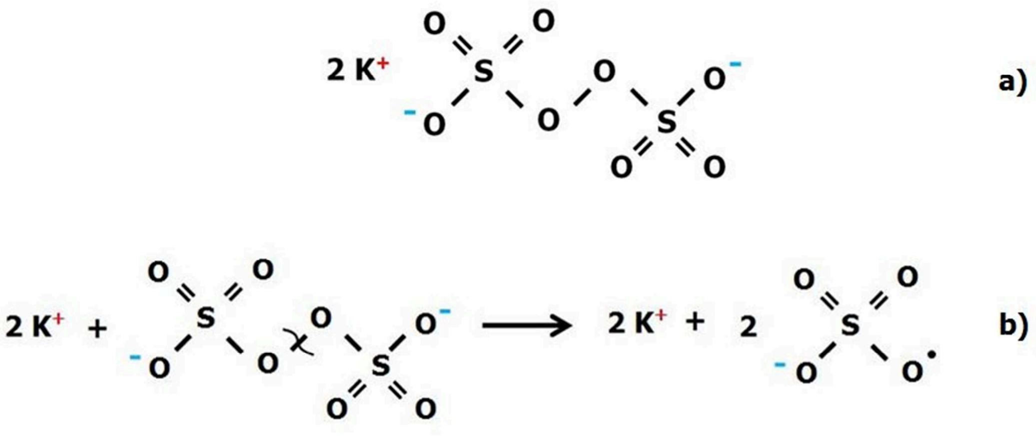

Figure 2.5: a) Initiator KPS and b) decomposition of KPS.

As monomers for which free-radical polymerization is applicable exhibit a weak carbon-carbon double bond the radical can subtract one of the pi-bonded electrons while the sigma-bond is not involved in this reaction. Figure 2.6 shows the reaction between the radical caused by decomposition of KPS and DMAA which are initiator and monomer, respectively, under consideration in this thesis.

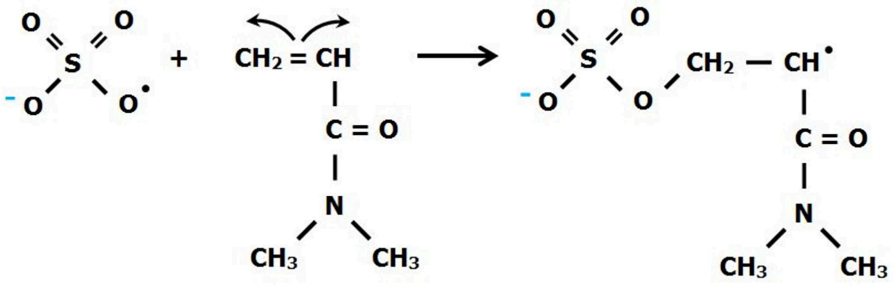

Figure 2.6: Reaction of radical with monomer DMAA.

Thus the monomer exhibits a remaining unpaired pi-electron with a high attraction to electrons from another molecule. In the case of chain propagation it reacts with the pi-electron from another monomer. By doing so the location of an unpaired electron moves to the end of the chain that starts to grow. As this process is continuously repeated a polymer chain is being built.

Chain propagation (and hence the polymerization process) is stopped by either so called 'coupling' or 'disproportionation'. Coupling describes the bonding of two radical ends of two growing chains, resulting in one long polymer chain. Disproportionation describes the transfer of the hydrogen atom that sits on the second-to-last carbon atom from one growing chain to another. The 'empty' spot on the chain which dispenses the hydrogen is replaced by a carbon-carbon double bond. Hence the result of disproportionation are two unequal polymer chains (Smeltz and Dyer, 1952).

As stated above, free-radical polymerization mechanism is susceptible to oxygen influence. While in some cases it is capable of initiating radical polymerization, it more often inhibits chain growth. The inhibition is due to reaction of oxygen-radicals to other radicals such the decomposed initiator or growing chain ends. The likelihood of this reaction compared to chain propagation is high because of the other radicals being sluggish in reaction. Hence, radical-polymerization is often conducted in an inert atmosphere which for instance can be achieved by purging a reaction chamber with nitrogen (Slugovc, 2011). It has been shown that the inhibition of certain polymerizations initiated by potassium persulfate is related to an induction period which is dependent on initiator and oxygen content (Smeltz and Dyer, 1952). The suggested reaction of oxygen with a growing PDMAA-chain is shown in Figure 2.7.

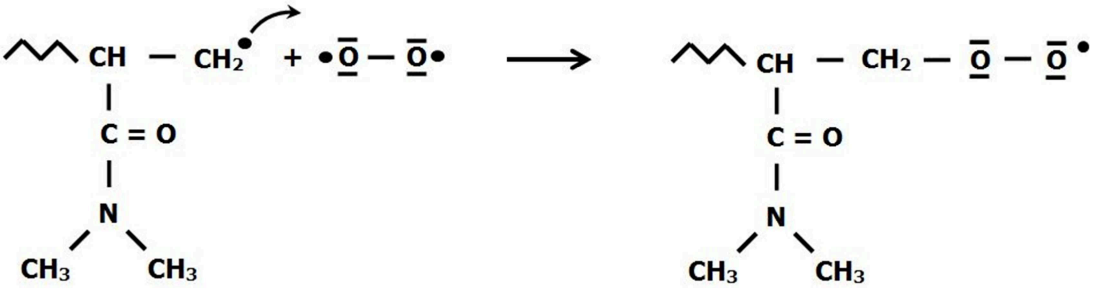

Figure 2.7: Reaction of oxygen with growing PDMAA-chain.

The role of clay has been subject to clarification in literature. According to Haraguchi et al. (2002) SO4-. and K+ evolved from the initiator are attached to the clay surface and bond the polymer chain end by ionic interaction. As a consequence, so called clay-brush particles are being built as shown in Figure 2.3 (middle). As the grafted chains grow, a physical network is being built. Additionally, coordination interactions between polymer chains and Si on the clay surface are asserted. A different reference (Li et al., 2009b) suggests that instead of purely ionic interaction also ion-dipole interactions have to be assumed – at least for the combination of clay with initiator AIBN. In any case a large number of polymer chains are grafted to each clay platelet compared to organic cross-linkers which have a functionality of three or four. Consequently, clay is referred to as multifunctional cross-linker. The number of multifunctional cross-links per unit of volume is very low compared with the number of organic cross-links (Haraguchi and Takehisa, 2002) for the same number of bonds since the effective functionality of the clay is much higher. This is followed by greater distances between the clay platelets which allow the polymer chains to be flexible in contrast to traditional hydrogels. An advantage which allows to overcome the problem of the spatial gel inhomogeneity is the possibility to prepare nanocomposite hydrogels with a very narrow chain length distribution as the clay disperses uniformly (Haraguchi et al., 2002). This is probably responsible for the improved mechanical properties although definitive evidence does not exist.

2.2 Fundamental Theories regarding Mechanical Properties of Soft Materials with Focus on Fracture Mechanics

This chapter aims at giving a fundamental understanding of mechanisms leading to mechanical properties of nanocomposite hydrogels. Several theories with the purpose of explaining material's behaviour shall be considered. Major focus is laid on the discussion of fracture mechanics as well as on stretching behaviour of nanocomposite hydrogels. A further aspect is the comparison of nanocomposite hydrogels with other material classes, in particular with filled elastomers.

2.2.1 True Elasticity Theory vs. Rubber Elasticity Theory

'Elasticity' describes material behaviour that is deformable where the deformation is totally recoverable (Flory, 1984). Two different types of elasticity have two be distinguished: the so called 'True Elasticity' (also Enthalpic Elasticity) which is derived from energetic sources compared to the so called 'Rubber Elasticity' (also Entropic Elasticity) based on entropic sources.

Glassy polymers typically follow True Elasticity Theory when very small strains are applied. Characteristic of polymers is a Poisson's ratio of about 0.3 in the glassy state (Halary et al., 2010). The Poissons's ratio describes the negative ratio between transverse strain and axial strain. Hence, a Poisson's ratio of 0.3 means that a transverse strain of 100 % is followed by contraction in width of approximately 30 %. Poly(methyl-methacrylate) (PMMA, Perspex) can be stated as a representative polymer following True Elasticity Theory at ambient temperature. Materials following True Elasticity Theory show identical linear graphs for loading and unloading components in the stress-strain curve at loads below the yield stress and can be described by Hook's Law, given Eq. 2.1.

$$\sigma_{ij} = C_{ijkl} * \varepsilon_{kl} \tag{2.1}$$

where σ_{ij} is the stress tensor with $i, j = [1;3]$ and ε_{kl} is the strain tensor with $k, l = [1;3]$. C_{ijkl} is the stiffness tensor connecting stress and strain tensor.

In contrast, Rubber Elasticity Theory can be applied to polymer networks well above their T_g, where polymers typically exhibit a Poisson's ratio of about 0.5, implying that they are (nearly) incompressible. A representative material following this theory is cross-linked natural rubber as the theory's name suggests. The theory was first introduced by Flory (Akagi et al., 2011) as an attempt to describe a non-Hookean elastic material behaviour. Several assumptions are made in order to approximate the stress-strain relation: Firstly, Gaussian statistics are assumed to be valid to calculate the distribution of end-to-end distances of polymer chains. Secondly, local and macroscopic deformations are assumed to be affine, which was first proposed by Flory in the Affine Model Theory (Flory, 1953). Thirdly, the Poisson's ratio is fixed at a value of 0.5. The theory presumes no imperfections in the network. The basis for the calculation is the Second Thermodynamic Law, determining that entropy has to be maximized (Flory, 1984). Physically, this means that the force to stretch a polymer chain is equal to a decrease in entropy. The polymer chain will strive for recoiling back into its original average shape as soon as the stress is released in order to increase entropy. The result of the theory is that for tensile deformations cross-linked rubbers follow the relation given in Eq. 2.2 (Akagi et al., 2011).

$$\sigma = \mathrm{G} * (\lambda - \frac{1}{\lambda^2}) \tag{2.2}$$

where λ is the extension ratio and G is the elastic Shear Modulus (Halary et al., 2010). Thus, plotting σ against $(\lambda - \frac{1}{\lambda^2})$ results in a linear graph with slope G. The Young's Modulus, E, is readily obtained by the relationship given in Eq. 2.3.

$$E = 2 * G * (1 + \nu) \tag{2.3}$$

where ν represents the Poisson's ratio. As Rubber Theory directs a Poissons' ratio of 0.5 this relationship always leads to the approximation $E = 3 * G$. Applying Simple Rubber Elasticity Theory to evaluate data allows the estimation of the number of network chains

n between cross-links per unit volume of rubbery materials. This is due to the relationship given in Eq. 2.4.

$$\mathrm{G} = \mathrm{k} * \mathrm{T} * \mathrm{n} \tag{2.4}$$

where T is the absolute temperature. The cross-link density μ (number of cross-links per unit volume) depends on the functionality of the cross-linking sites. It has been shown to be equal to $\frac{n}{2}$ for a functionality of four (Treloar, 2005). The theory only describes polymers that are highly flexible and cross-linked, including physical cross-links as for thermoplastic elastomers. For instance, it applies to a thermoplastic like PMMA well above its T_g for short time scales. Most polymers do not perfectly follow Rubber Elasticity Theory. Reasons for this are discrepancies from various assumptions made to establish Simple Rubber Elasticity Theory such as perfect networks (e.g. no loose chain ends) and affine deformation. As indicated above, strain-induced crystallization and non-Gaussian deformation at higher strains are not predicted by Simple Rubber Elasticity Theory. However it shall be remarked that these only provide for deviations at high strains.

2.2.2 Mooney-Rivlin Theory

Attempts to predict a more accurate relation between applied stress and strain than Rubber Elasticity Theory is capable of have resulted in various other theories. The observation of higher stresses than predicted by Simple Rubber Elasticity Theory for some rubbers at low strains is one evident discrepancy of real material behaviour from this theory. The Mooney-Rivlin Theory – serving as an example for alternative theories and subject of discussion in this subchapter – modifies the relationship between stress and strain known from Rubber Elasticity Theory by adding an additional term. It shall be pronounced that although additional interaction between chains is assumed, the term is not found upon any molecular model. Thus, the Mooney-Rivlin Theory is a semi-empirical theory. It takes network defects such as intramolecular loops and loose chain ends into account which is an improvement compared to Rubber Elasticity Theory. Furthermore, deformation is assumed to be non-affine in this theory. That means that not all cross-linking sites move by the same amount during deformation. However it only applies to low to moderate strains. Mooney and Rivlin assume the material to be isotropic in the unstrained state and to exhibit a Poisson’s ratio of 0.5 (Treloar, 2005). Details and derivations for this semi-empirical theory can be found in (Halary et al., 2010). Flory

(1984) states, that the Mooney-Rivlin formulation is inadequate for compression and biaxial strain. For uniaxial tension the theory results in the relation as given in Eq. 2.5:

$$\sigma = 2 * \left(C_1 + \frac{C_2}{\lambda}\right) * \left(\lambda - \frac{1}{\lambda^2}\right) \qquad (2.5)$$

C_1 and C_2 are called 'elastic constants' and are gained from evaluating experimental data by fitting a curve to the found reduced stress as a function of $\frac{1}{\lambda}$. C_1 is due to entropic forces in the network (bonded interactions) while C_2 is due to non-bonded interactions (Eichinger, 1990). The Shear Modulus G can be derived by the calculation given in Eq. 2.6:

$$\mathrm{G} = 2 * (C_1 + C_2) \qquad (2.6)$$

Converting Eq. 2.5 to the form given in Eq. 2.7 shows the reduced stress, which is independent of λ, on the left side. Plotting the reduced stress as a function of $\frac{1}{\lambda}$ gives a linear graph with slope $2 * C_2$ and intercept $2 * C_1$ for materials following this theory. In particular systems it is found that instead of a linear graphs curves with either an upwards or a downwards slope or both are found. The slope of the graph can directly be interpreted as softening (downwards) or hardening (upwards) effects (Carlsson et al., 2010).

$$\frac{\sigma}{\lambda - \frac{1}{\lambda^2}} = 2 * \left(C_1 + \frac{C_2}{\lambda}\right) \qquad (2.7)$$

2.2.3 Mullins Effect and Payne Effect

As the nanocomposite hydrogels under consideration display a structure similar to filled elastomers, their properties will be compared in this study. Natural rubber filled with carbon black and poly(dimethylsiloxane) (PDMS) filled with silica are amongst the most investigated in this material class. When comparing neat elastomers to filled elastomers three major differences are evident: Filled elastomers typically exhibit a higher Modulus, a higher toughness and a greater ability of dissipating energy. Characteristic effects that describe this higher dissipation of energy are the Payne Effect as well as the Mullins Effect which are briefly described in the following (Halary et al., 2010). When applying a cyclic load at constant frequency to a material, the Payne Effect describes the rapid decrease of the Storage Modulus in the range of small strains (typically smaller than 100 %). After this drop the Storage Modulus reaches a new plateau. Simultaneously the Loss Modulus exhibits a maximum. The effect is displayed in Figure 2.8. The Payne Effect is dependent on temperature, filler content and filler distribution. There are several theories aiming to explain the reason for this phenomenon. Most of them consider the effect to be related to the fracture and recovery of the filler network.

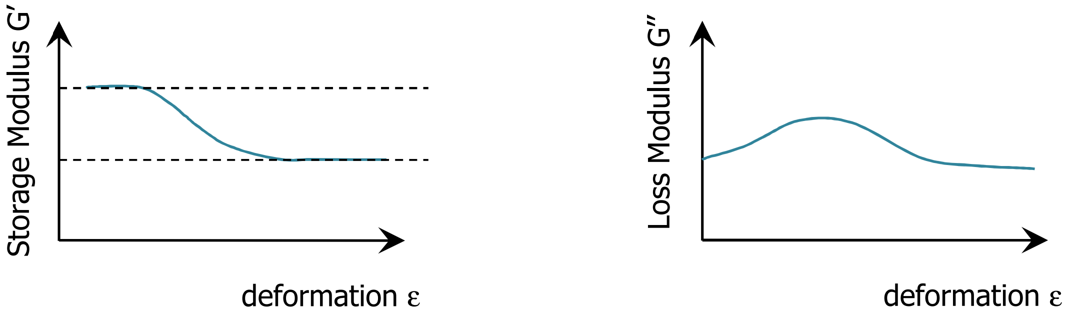

Figure 2.8: Payne Effect.

In contrast to the Payne Effect the Mullins Effect regards strains larger than 100 %. It describes the hysteresial behaviour of filled elastomers. When loading a sample until a certain strain ε_1 followed by unloading, a hysteresis will appear. When loading again, the current loading curve will have a lower stress level than the first one. However, it will intersect it at strain ε_1. Figure 2.9 illustrates the Mullin's Effect by displaying a first loading A until point P_1, followed by unloading B. A second loading is displayed as C and intersects with the first loading at P_1. Bueche (1960) associates the effect to the debonding of polymer chains from fillers. It is proposed that chains that are just about to debond or break contribute the most to the material's Modulus at the present strain. Bueche postulates a debonding of the shortest polymer chains at the first loading. As these do not contribute to the elastic force in the following loading cycle, the stress level is lowered. At a strain larger than at the first loading, longer polymer chains are subjected to the stress and are at this stage primarily responsible for the material's Modulus. This results in the merging of the first with the second curve.

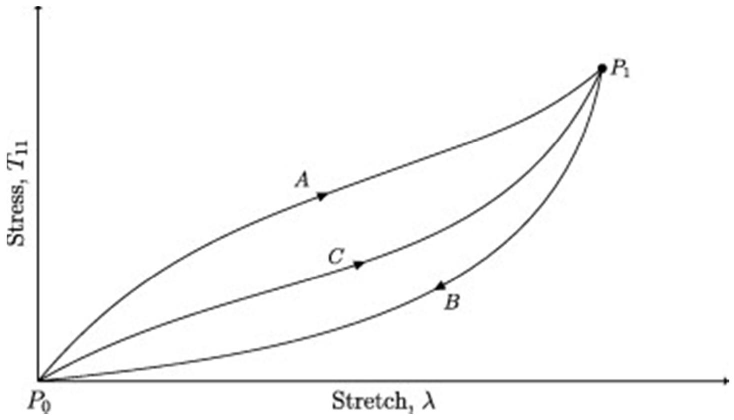

Figure 2.9: Mullins's Effect (Rickaby and Scott, 2013).

2.2.4 Fracture Mechanical Approaches

As little research has been done on fracture mechanics of gels in particular, this chapter aims to give a summary of what is known about the fracture behaviour of soft polymers/elastomers. The concepts for fracture behaviour of hydrogels are believed to be similar as they consist of a polymer network well above T_g. Before describing theories for fracture behaviour, the terms 'toughness' and 'fracture toughness' shall be discussed briefly.

Giving a clear definition of 'toughness' is hardly possible as literature gives many different ones. One of the most common ways to estimate toughness is to integrate the stress-strain curve until fracture obtained by tensile testing. The area under the curve specifies the energy that can be absorbed by a sample before breaking (Center, 2012; Lever, 2000) and is also called 'work of fracture' (Ashby et al., 2007). This approach usually assumes that the material is flawless. As the integration of the stress-strain curve leads to single-point data it cannot be distinguished between a material exhibiting high strength and low ductility and a material exhibiting low strength and high ductility. Several factors influence a rubber's toughness such as its molecular weight and its cross-linking density (ASM International, 2003). Using the term toughness is often misleading since different values and properties are referred to by it, e.g. impact toughness.

In contrast to 'toughness' the term 'fracture toughness' is clearly defined: it determines the energy or stress that is absorbed when a crack propagates. It is defined by either an energy-parameter (critical energy release rate G_c) or a stress-parameter (critical stress-intensity factor K_c) dependent on the approach used for its determination. The parameters G_c and K_c, which are material parameters, can be transformed into each other. Fracture mechanics assumes cracks or flaws to be present in a material. These are taken into account when determining the critical parameters G_c or K_c. At present G_c and K_c can only be found by experimental approaches for most materials, for instance by employing the Compliance Method for G_c. K_c is typically determined by analysing the force-displacement curve. For elastomers G_c can be predicted as will be explained in more detail in a following subchapter. In contrast to tensile strength, fracture toughness parameters allow to determine a critical defect size under specified loading conditions. Industrial application exploits this knowledge to define non-destructive analysing techniques necessary to detect critical flaws. In addition, fracture toughness parameters are employed for material development. In mechanical engineering finite element modelling

(FEM) is often used to analyse stress-concentrations, expressed as stress-intensity factor K. This factor K is then compared with the critical factor K_c.

G- and K-approaches are continuum theories which do not take a material's microstructure into account. As a consequence, G_c and K_c can be locally different from the bulk properties. Further it has to be remarked that fracture mechanics as discussed above is only valid for linear elastic material behaviour with the expansion of small scale yielding. Other fracture mechanic concepts as Elastic-Plastic Fracture Mechanics or Post-Yield Fracture Mechanics can be applied for other material behaviours (Anderson, 2005).

The following subchapters delve into attempts of describing mechanical behaviour of soft materials. An introduction to the origins of fracture mechanics is followed by a discussion of the Lake and Thomas Theory as well as by the presentation of discrepancies of real material behaviour from this theory.

2.2.4.1 Griffith Criterion

As far as known, Griffith (Griffith, 1921) was the first one to introduce a criterion to determine whether instant crack growth would occur in a material with initial crack size a. His theory is fully based on an energy balance and results in the Griffith Criterion displayed in Eq. 2.8:

$$-\frac{\partial E_{el}}{\partial a} > \gamma_s * \frac{\partial A}{\partial a} \tag{2.8}$$

where E_{el} is the stored elastic energy, ∂A is the surface created by crack growth ∂a and γ_s is the surface free energy per unit area of the material (Gdoutos et al., 2003; Rivlin and Thomas, 1953). The left term of Eq. 2.8 is also referred to as the strain energy release rate G while the right term is the critical strain energy release rate G_c. Griffith assumes that the only energy necessary to initiate crack growth is energy being used to create new surface area. In order to allow minor plastic deformation near to the surface and close to the crack tip, γ_s is extended by a plasticity term. With this expansion this criterion works well for many materials. However, it cannot be applied directly to describe fracture mechanics for elastomers as this material class exhibits significant deformation near the crack tip.

2.2.4.2 Lake and Thomas Theory

One major discrepancy from the Griffith Criterion that can easily be observed is that while Griffith assumes that there is no (large) deformation prior to failure, cross-linked rubbers exhibit the opposite. Another discrepancy is that according to Lake and Thomas (1967) elastomers do not exhibit crack propagation for deformations below a critical value even in the presence of a flaw as they blunt. So as to transfer the Griffith Theory to elastomers, the Lake and Thomas Theory was established (Gdoutos et al., 2003). In order to give a quantitative measure of the stresses at the crack tip for a sample that is held at constant extensions a term called tearing energy T, given at Eq. 2.9 is introduced. E determines the stored elastic energy while A determines the crack's surface area.

$$\mathrm{T} = -\frac{\partial E}{\partial A} \qquad (2.9)$$

T is dependent of the crack growth. According to Gdoutos et al. T represents the strain energy release rate G. Extrapolation of the crack growth ∂A as a function of T makes it possible to determine a limit value T_0 below which no crack growth occurs. In doing so Lake and Thomas calculate the crack growth limit of elastomers, independent of sample geometry and size, i.e. T_0 is a material property. It is stated that the value is determined by the molecular structure of the elastic material.

However, it has been found that T_0 is considerably higher than calculated surface energies. This, according to Lake and Thomas (1967), is due to the fact that '*in order to break mechanically a particular bond in a chain it is necessary to subject all other bonds lying in the same chain to virtually the breaking force*'. Additionally adjacent polymer chains are only deformed elastically. The energy balance expressed in Griffith's criterion for ideally brittle materials states that the decrease in elastic strain energy is followed by an increase in surface energy. For elastomers the argument given above results in the fact that in this energy balance other forms of energy (most importantly plastic deformation of the material near close to the crack tip) have to be added at the side of the surface energy. Elastomers and gels that can be described by this deviation of the Griffith's criterion (e. g. PDMS without fillers) are still brittle in that they fail well below the yield stress and are not tolerant even of small flaws.

2.2.4.3 Dissipation of Energy in Viscoelastic Materials

It has to be pronounced that reaching energies of T_0 is followed by limited crack growth only. Unstable crack growth only occurs at a much higher energy, the so called Catastrophic Tear Strength T_C (Lake and Thomas, 1967). The reason is thought to be the hysteresial behaviour of rubbers which reduces the stress at the crack tip. The absence of ideal elasticity leads to dissipation of energy. Thus the extent to which T_0 and T_C differ from each other depends highly on the viscoelastic properties of the elastomer in question. A consequence of this effect is that in contrast to T_0, T_C as well as the tensile strength is dependent on temperature and strain rate. The main features determining the viscoelastic behaviour are firstly the chemical structure and secondly the three-dimensional network which both prevent flow. Viscoelasticity means that the material combines elastic with viscous properties. A purely elastic material deforms instantly at the application of an external force; when the force is released it retrieves its original state again instantly. In contrast, purely viscous materials deform linearly with time at the application of an external force.

Bueche and Alpin (1964) have reported that fracture behaviour of elastomers can be described by their creep curve, i.e. the behaviour under a constant load. Their theory suggests that at the very front of a crack tip a thin filament is positioned which is exposed to a certain stress (that is assumed to be about two to three magnitudes higher than the nominal stress). As the filament ruptures, the crack grows at the amount of the filament thickness. Bueche and Alpin suggest that the time necessary for this growth is dependent on the retraction of this filament and in addition on the reaction of the adjacent filament which is then exposed to a higher stress. Bueche and Alpin expect that the time necessary to fracture a specimen is simply the product of the time taken to rupture one filament multiplied by the number of filaments in the crack's layer. As they estimate a very high number of filaments, they conclude that the time for a single filament fracture is very small and the viscoelastic response therefore much faster than the response of the whole specimen. With these assumptions and the application of the Mooney-Rivlin formulation discussed above, they are able to determine an elastomer's strain-at-break as well as stress-at-break from its creep function.

Two known mechanisms for viscoelastic dissipation of energy are strain-hardening as well as blunting. These mechanisms are subject of discussion in the following paragraphs.

Strain-Hardening as a Viscoelastic Phenomenon

At high strains some elastomers exhibit a feature called strain-hardening. Strain-hardening means that at high strains the material stiffens significantly (Mark et al., 2013). This can be shown in a stress-strain curve, as shown in Figure 2.10.

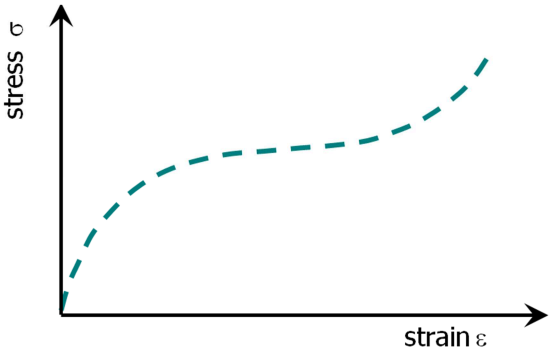

Figure 2.10: Stress-strain curve for a strain-hardening material; in style of (Miyaji et al., 2001).

Strain-hardening describes the increase of stress necessary to stretch a material after reaching its yield strength. Elastomers often show softening before strain-hardening occurs. This is displayed by the decrease of the slope in the stress-strain curve at lower strains (left part of diagram in Figure 2.10).

One common mechanism in strain-hardening of isotactic materials is strain-induced crystallisation. However this mechanism is not present in atactic materials. Another mechanism leading to strain-hardening is related to polymer chains reaching their extensibility limit (no longer Gaussian). Stretching a material to low or moderate strains leads to orientation (change of configuration). Once the molecules lie in the direction of the force additional strain can only be gained by stretching the chain bonds as well as changing the bond angles (Horgan and Saccomandi, 2006). This is induced by significantly higher stresses. Figure 2.11 shows a schematic graph for the potential energy as a function of interatomic distance. Without external load the bond length corresponds to the equilibrium bond length having the lowest potential. While stretching, however, the distance of atoms from each other is increased which is equal to a higher potential energy (shifting to the right on the graph in Figure 2.11). The equivalent is valid for a change in bond angle.

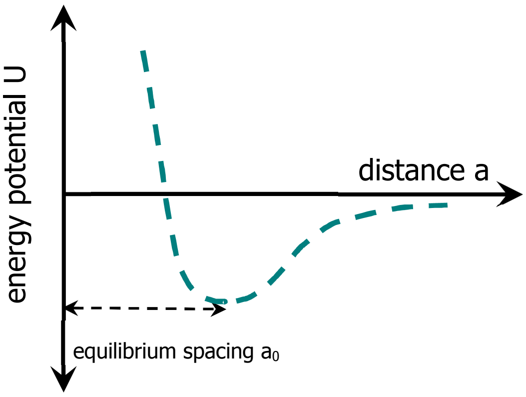

Figure 2.11: Energy Potential as a function of interatomic distance; in style of (M. F. Ashby and Jones, 2012).

It has further been proposed that strain-hardening is caused by the fact that elongation of the bulk material is not linearly proportional to single chain elongation while stretching, meaning that the deformation is non-affine (Carrillo et al., 2013). It is suggested that for polymeric networks certain so called deformation regimes exist. According to this, the chains deform linearly with small external deformations but deform non-linear with larger external deformations. This is because for small deformations the chains can freely stretch (called 'worm-like') while at larger deformations they reach their extensibility limit.

It is believed that strain-hardening contributes to polymer's fracture toughness in terms of orientating polymer chains in front of the crack tip. As described in subchapter 2.2.4.2 in order to allow for crack propagation all chains lying in the cracks plane have to be broken. Hence it is believed that due to previous orientation of the chains perpendicular to the crack plane the number of chains per unit crack area is increased. Therefore higher energies are required to allow crack growth.

Blunting as a Viscoelastic Phenomenon

For some materials an increase of an external load leads to large deformation instead of an increase in the stress level at the crack tip. This phenomenon is called blunting. The deformation due to blunting refers to the displacement of the crack flanks and needs to be separated from plasticity in the process zone ahead of the crack tip. As the stress field in front of the crack tip is dependent on the curvature of the crack tip it is affected by blunting. An illustration of this relationship is shown in Figure 2.12. An increase of the crack diameter thus leads to a higher energy necessary to achieve crack propagation (i.e. blunting yields higher fracture toughness) (Lillie and Gosline, 2002). It shall be remarked that the stress field in front of the crack/notch is a three-dimensional one while Figure 2.12 for simplicities sake only displays the stress in the direction of the crack propagation.

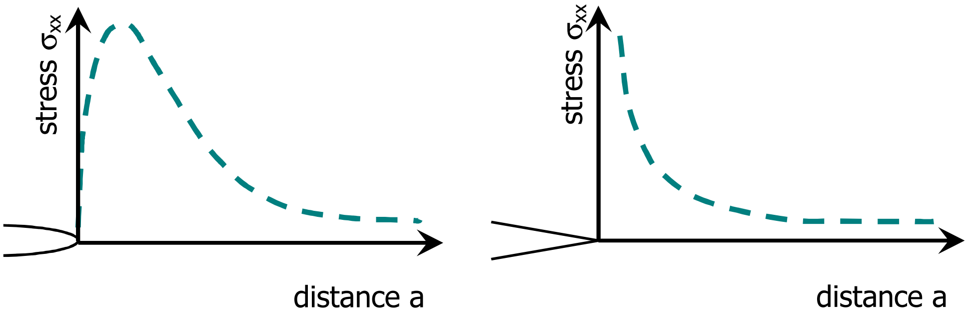

Figure 2.12: Stress field in front of a notch (left) and in front of a crack (right).

Hui et al. (2003) found that a crack blunts if the cohesive stress is more than approximately double the material's Young's Modulus. This is reasoned by the fact that the stress in a material is then governed by its Modulus instead of its strength. If in contrast the cohesive stress is smaller than the Modulus, the stress level at the crack tip is increased in incremental steps until reaching the cohesive stress which is followed by crack propagation. However, even if blunting occurs, a crack will eventually propagate. It has been shown that this can be due to one of the following mechanisms: Small voids inside the material can turn into internal cracks (Gent and Wang, 1991) or micro-cracks can be initiated which then propagate (Hui et al., 2003).

2.2.4.4 Methods to characterize Fracture Toughness of Soft Materials

Typically, soft materials are capable to be elongated to very large extents in comparison with other materials. Thus, special techniques to determine their fracture toughness have been developed. The three most common tests are the trouser tear test, the single-edge crack test, and the pure shear test. Specimen geometries are depicted in Figure 2.13 a) for the trouser tear test, b) for the single-edge crack test and c) for the pure shear test. As depicted, specimens used for the trouser tear test are cut in the middle further than half of the specimen length. The so generated 'legs' are subsequently pulled in opposing directions. As for the single-edge crack test the cut is positioned in the middle of the specimen. The force is applied vertical to the crack. The outcome of each of the tests is the critical strain energy release rate (or tearing energy) G_c, which is a material constant and therefore has to be independent of the sample geometry. It shall be noted however, that in contrast of the independency of sample geometry G_c it is often dependent on temperature and on strain rate. For double-network hydrogels G_c has been shown not to be dependent strain rate (Yin et al., 2013) and on temperature.

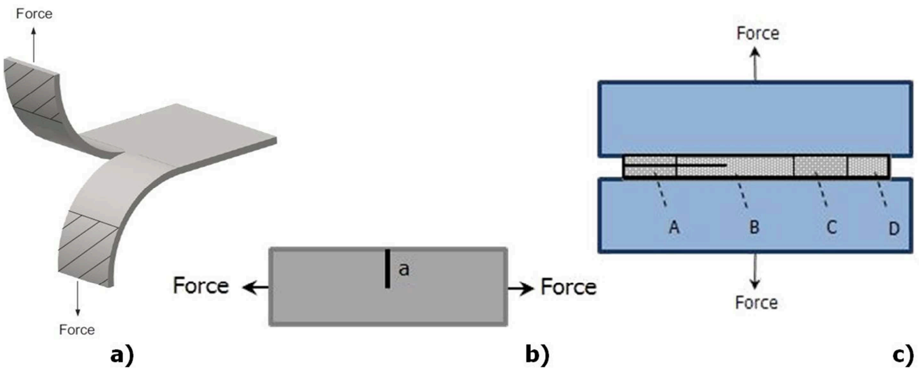

Figure 2.13: Specimen geometry for fracture toughness tests **a)** trouser tear test; in the style of (2007), **b)** single edge notch test, **c)** pure shear test.

Both, trouser tear test and single-edge notch test are unsuitable when the strain-at-break is large. In this case fracture cannot be obtained as common tensile testing machines have a limited crosshead travel that is reached before the specimen breaks. Hence, the major advantage of the pure shear test compared with the trouser leg test and the single-edge notch test is that a minor crosshead travel is necessary. As the pure shear test according to (Sun et al., 2012) will be employed in this study to determine fracture toughness parameters for prepared nanocomposite hydrogels, it shall be discussed in more detail.

The test was first introduced by Rivlin and Thomas (1953) with the basic requirement of the specimen geometry to have a large ratio between initial width and length. The sample geometry including suggested dimensions (Sun et al., 2012) is displayed in Figure 2.14. As a consequence of this large ratio it is assumed that width remains constant under tensile deformation. Following, stretches in directions x (direction of force), y (direction of width) and z (direction of thickness) can be defined as $\lambda_x=\lambda$, $\lambda_y=1$ and $\lambda_z=1/\lambda$.

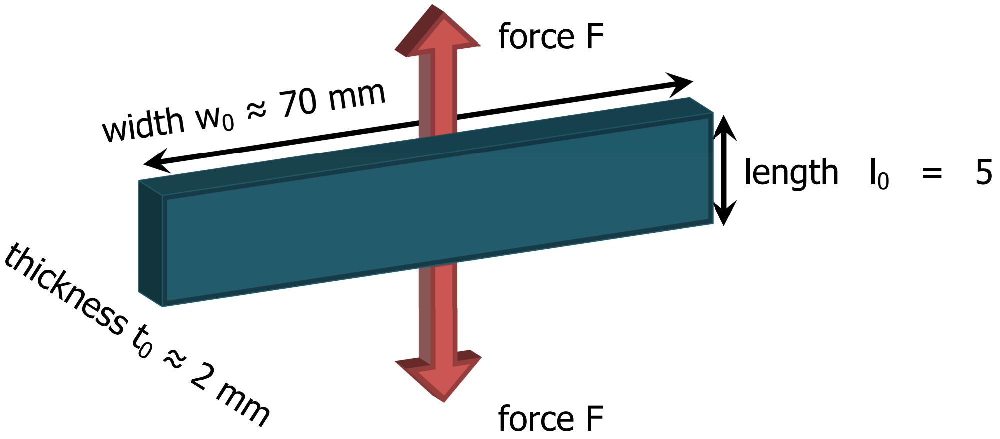

Figure 2.14: Specimen geometry including dimensions for pure shear test.

As shown in Figure 2.13 c) a specimen is divided into four specific regions. Zone A is believed to be a relaxed region, zone B to be in a complex stress state while Zone C is a pure shear region. Zone D is assumed to be almost a pure shear region, too. Rivlin and Thomas (1953) postulate that as deformation occurs, zone B does not change its stress state but simply shifts by a growing zone A and a decreasing zone C. As a consequence, crack propagation is accompanied by the conversion of material from a pure shear state to a relaxed state. A further assumption of the theory is that the specimen deforms only in length and thickness while the width stays undeformed as mentioned above. The theory results in calculation for G_c as given in Eq. 2.10:

$$G_c = W_0 * l_0 \tag{2.10}$$

where W_0 is the elastic energy density in the pure shear region that can be obtained from the load-displacement curve and l_0 as the initial sample length (Halary et al., 2010). Sun et al. (2012) found that G_c is independent of the crack length. They suggested performing the test by using a pair of specimen, one notched and one unnotched. In the proposed test the load-displacement curve of the notched specimen is recorded until extension-at-break s_c. Thereafter, the load-displacement curve of the unnotched specimen to an extension longer than the extension-at-break s_c – from the notched sample – is recorded. The value utilized for calculating the fracture toughness parameter is the area $U(s_c)$ under the load-displacement curve of the unnotched sample until s_c. Fracture energy values are then calculated as given in Eq. 2.11.

$$G_c = \frac{U(s_c)}{l_0 * b_0} \tag{2.11}$$

where l_0 is the initial sample length and b_0 is the initial sample width. Exemplary load-displacement curves for unnotched and notched samples are shown in Figure 2.15 above and below, respectively, to illustrate the approach.

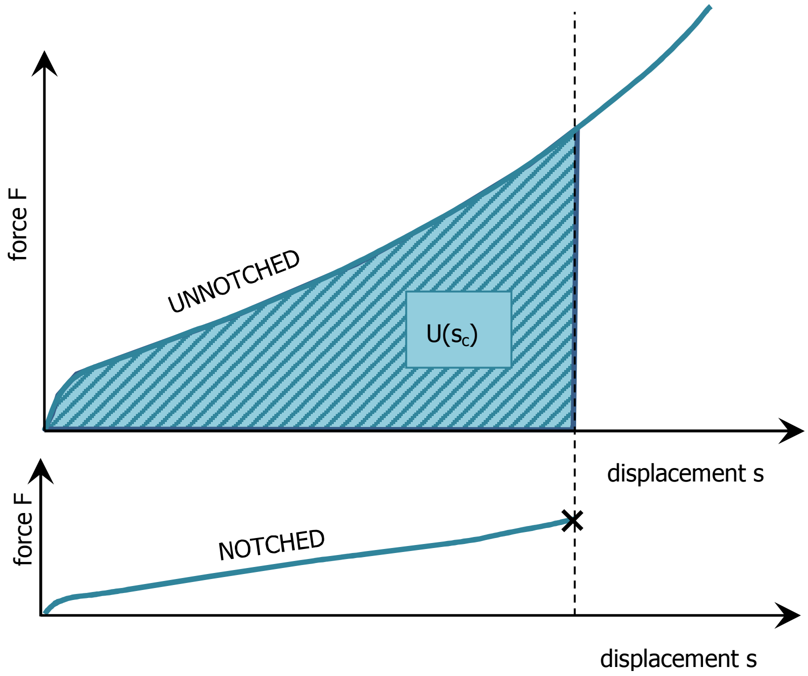

Figure 2.15: Evaluation of pure shear test.

3 METHODS

3.1 Materials

Within this study polymer-nanocomposite hydrogels are prepared. The nanofiller consists of clay which acts as an inorganic cross-linker. Samples consisting of different thickness and clay contents as well as hydrogels with an organic cross-linker are studied. The monomer used is *N,N*-Dimethylacrylamide from Sigma-Aldrich Co. LLC (St. Louis, Missouri). Clay of type Laponite XLS®, a synthetic hectorite, was generously given from Rockwood Additives Ltd. (Princeton, NJ). *N,N'*-methylenebis(acrylamide) (BIS) (Sigma Aldrich Co, LLC, St. Louis, Missouri) is employed as organic cross-linker. Potassium persulfate (KPS) from Sigma Aldrich Co. LLC (St. Louis, Missouri) is used as initiator. *N,N,N',N'*-tetramethylethylenediamine (TEMED) from Sigma-Aldrich Co. LLC (St. Louis, Missouri) is used as accelerator. Water used in sample preparation is pure water (Elix 3 Water Purification System, EMD Millipore Corporation, Billerica, MA; Product Water Resistivity > 5 – 15 MΩ∗cm).

Chemicals that were discarded but used in the process development of sample preparation include a different type of clay, Laponite XLG® (Rockwood Additives Ltd., Princeton, NJ) as well as a different type of monomer, *N*-Isopropylacrylamide (Wako Pure Chemicals Industries Ltd., Osaka, JP). Table 3.1 lists sample identity of prepared materials given by the type of cross-linker and cross-linker concentration. In general sample thickness is 2 mm. In order to study effects of thickness in sample preparation as well as mechanical performance additional samples with a thickness of 1 mm and 3 mm are prepared for medium clay concentration of 9 mole% per L water.

One specific goal of this study is the development of a methodology for sample preparation. A detailed depiction of the development is given in subchapter 4.1. The following paragraphs only outline the resulting sample preparation:

X g of clay is added to 19.5 mL of precooled pure water, forming an opaque solution. The mixture is continuously stirred in an ice bath with a magnetic stirrer with at least 300 rpm. Afterwards 4 mL of monomer is added. After at least one hour (when the mixture turns transparent indicating the dispersion of clay) 30 µL of accelerator and 2 mL of an aqueous solution of initiator are added. Thereafter, the solution is poured into a polypropylene (PP) bag with a funnel. The bag is subsequently squashed between two slightly precooled glass slides and fixed with clips. Different plastic spacers are used to control the thickness of the samples (1 mm, 2 mm and 3 mm). Next, this system is placed in a chamber where oxygen is instantly removed by a vacuum pump followed by filling the chamber with nitrogen gas. The step of evacuating the chamber and feeding with nitrogen is repeated several times. In-situ free radical polymerization is allowed to proceed for roughly 55 h at ambient temperature. After the polymerization all samples are stored in airtight containers to avoid drying out. The PP-films are removed by peeling after cutting alongside the edges directly before testing the materials.

Table 3.1: Features of used materials.

Sample	**Cross-linker**	**Cross-linker Content**	**Thickness of prepared Samples**
-	**-**	**mole% per l water**	**mm**
NC 7	Clay	7	2
NC 9	Clay	9	2
NC 11	Clay	11	2
NC 13	Clay	13	2
NC 9_THIN	Clay	9	1
NC 9_THICK	Clay	9	3
OR 9	BIS	9	2

3.1.1 Preparation of Test Specimen

Specimens used for Fourier-transformation infrared spectroscopy are prepared by drying the samples at ambient temperature for about one week after peeling the PP-film on both lower and upper side.

Specimens used for X-ray diffractometry are prepared by freeze-drying the samples at -50 °C for approximately 48 h after peeling the PP-film on both lower and upper side. The samples are then ground with mortar and pestle.

Specimens used for transmission electron microscopy are prepared by freeze-drying the samples at -50 °C for approximately 48 h after peeling the PP-film on both lower and upper side. Afterwards the specimens are sectioned using a Leica Ultra-Cut 7 microtome (Leica Microsystems Pty Ltd, Wetzlar, D) with glass knives to yield ultrathin films of about 70 - 90 nm thickness.

Specimens used for rheometry measurements are round test pieces with a diameter of 20 mm gained by using a punching die. As to achieve neat cuts the upper side of the PP-film is removed before punching the specimen. The lower side of the PP-film is only removed directly before placing the specimen between the plates of the rheometer.

Specimens used for dynamic mechanical analysis are pairs of rectangular shaped test pieces (13 mm x 16 mm) gained by cutting using an especially sharp pair of scissors. As to achieve neat cuts, the upper side of the PP-film is removed before cutting the specimen. The lower PP-film is only removed directly before mounting the specimen in the device. Organic cross-linked specimens are cut by using razor blades instead of scissors.

Specimens used for low strain measurements as well as for stress relaxation experiments are shaped as dumbbell test pieces according to ISO 27:2011 (Type 2) gained by using a punching die. As to achieve neat cuts, the upper side of the PP-film is removed before cutting the specimen. The lower side of the PP-film is only removed directly before mounting the specimen into the grips of the tensile testing machine.

Specimens used for fracture toughness testing applying the trouser tear test approach are rectangular shaped test pieces (7.5 mm x 50 mm) with a cut in the middle (30 mm) gained by cutting using a punching die with a slit. The specimen geometry is depicted in Figure 2.13 in the previous chapter. Specimens used for fracture toughness testing applying the pure shear test approach are rectangular shaped with dimensions of 25 – 30 mm x 70 mm. In order to obtain straight cuts of the given length (70 mm) a guillotine is used.

3.2 Characterization of Microstructure, Composition and Morphology

So as to study microstructure, composition and morphology of prepared nanocomposite hydrogel samples and hence verify to the quality of sample preparation process, X-ray diffractometry, thermo-gravimetric analysis, transmission electron microscopy and infrared spectroscopy are conducted. The latter two are additionally performed on organically cross-linked samples considered in this thesis.

3.2.1 X-Ray Diffractometry

In order to survey clay exfoliation in the stirring process of the sample preparation, X-ray diffraction (XRD) is performed using a GBC instrument and CuK_{α}-radiation with a graphite monochromator. Scans are performed between 1.8 and 10 degrees at 0.5 °/min with a step size of 0.02°. Samples are dispersed on low background oriented quartz substrates. The scans are conducted at 30 mA and 40 kV. Testing is performed on samples NC7, NC9, NC11, NC13 and pure clay.

3.2.2 Transmission Electron Microscopy

In order to verify the sample preparation, the exfoliation as well as distribution of clay, transmission electron microscopy (TEM) is carried out using a JEM 2011 TEM (Jeol Ltd., JP). Images are obtained with 50,000, 100,000 and 150,000-fold magnifications. The voltage is set to either 120.000 kV or 200.000 kV. Microscopy is performed on samples NC7, NC9, NC11, NC13 and OR9.

3.2.3 Infrared Spectroscopy

In order to study the composition of prepared nanocomposite and traditional hydrogels and clay, Fourier-transformation infrared (FT-IR) spectroscopy is conducted using an IR Prestige-21 FTIR Spectrophotometer (Shimadzu Corporation, JP). Scans are performed in an interval of wavenumbers between 4000 cm^{-1} and 500 cm^{-1}. Each gained spectrum is an average of 30 scans. All hydrogel samples are analysed employing the technique of attenuated total reflectance (ATR-mode). This technique is chosen because it is suitable for thick films. Samples exhibit a thickness of approximately 0.5 to 1 mm after the drying process. Additional measurements on the pure clay as received are performed in transmission mode employing the KBr-technique. Hence, the powdery clay is mixed with Kaliumbromide (KBr) before performing spectroscopy.

It is assumed that the preparation of samples with different thickness results in changes in the polymerization process which leads to different side- and/or end groups. FT-IR is performed to compare sample composition by detecting functional groups. A comparison between individual spectra aims to qualitatively identify similarities and differences between analysed samples. Additionally, spectra of nanocomposite hydrogels and of an organically cross-linked hydrogel are compared. Spectroscopy is performed on samples NC7, NC9, NC11, NC13, NC9_THIN, NC9_THICK and OR9, on a sample polymerized in air without the exclusion of oxygen as well as on clay as received.

3.2.4 Thermo-gravimetric Analysis

In order to examine the composition (water content) of the prepared hydrogel samples as well as the water content of the clay, thermo-gravimetric analysis (TGA) is performed on a Q500 device from TA Instruments (New Castle, DE). The heating profile for samples NC7, NC9, NC11 and NC13 is a constant heating rate of 2 °C/min starting at ambient room temperature up to 145 °C in a nitrogen atmosphere. The initial specimen weight is between 15 and 25 mg. The heating profile for measurements of the pure clay as received is a constant heating rate of 3 °C/min, followed by an isothermal hold time at 600 °C for 15 min.

3.3 Characterization of Mechanical Properties

In order to study the mechanical performance of nanocomposite hydrogels and to compare mechanical characteristics to organically cross-linked hydrogels mechanical testing is performed, including low strain tensile testing and fracture toughness testing. The measurements are carried out employing a tensile testing machine (Instron 5566, Instron Pty Ltd., VIC).

3.3.1 Low Strain Tensile Testing

'Low strain' tensile testing is performed at a constant crosshead speed of 100 mm/min. The axial strain is recorded employing a video extensometer (Advanced Video Extensometer 2663-821, Instron Pty Ltd., VIC). The video extensometer detects two identification marks by the use of contrast (either bright in front of a dark background or vice versa) and records their displacement while testing. The experimental set-up is displayed in Figure 3.1 including a specimen with white identification marks.

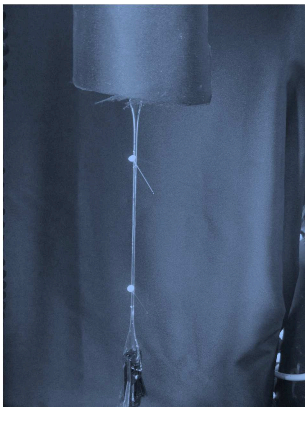

Figure 3.1: Experimental set-up necessary to apply video extensometer.

As nanocomposite hydrogels considered in this study are completely unsusceptible to flaws two white needles are inserted into the specimen. The surrounding of the tensile testing machine is covered by black cloth to achieve a dark background. The clamps used for conducting low strain tensile testing are displayed in Figure 3.3 a). Screws can be tightened to adjust the clamping pressure as desired and thus allow adequate mounting for the specimen. At least three specimens are tested for each sample and averaged for evaluation. The Young's Modulus is gained from the slope of a linear fit in the stress-strain curves between 0 % and 5 % strain as this is believed to represent the linear elastic region. As samples are assumed to be comparatively homogeneous as well as isotropic, the relationship given in Eq. 3.1 is employed to calculate the Shear Modulus G from the Young's Modulus E.

$$G = \frac{E}{2*(1+\nu)} \tag{3.1}$$

where ν is the Poisson's ratio and approximated with 0.5. Diagrams displaying tensile stress as a function of $(\lambda - \frac{1}{\lambda^2})$ where λ is the elongation ratio are compiled. They are referred to as 'Rubber Elasticity Plot'. Rubber Elasticity Plots are employed to estimate the number of network chains between cross-links per unit volume and the Shear Modulus. Diagrams displaying the reduced stress as a function of either λ or $\frac{1}{\lambda}$ are compiled and referred to as 'Mooney-Rivlin Plots'. The molecular mass M_c of the strands between cross-link sites is calculated both theoretically and from experiments and thereafter compared. The equations used for the experimental estimation is given in Eq. 3.2 while the one used for theoretical calculation is given in Eq. 3.3.

$$M_c = \frac{\rho*\varphi*N_A}{n} \tag{3.2}$$

where ρ is the density and is estimated as 1 g/cm^3, φ is the volume fraction of polymer in the hydrogel and is estimated from synthesis and n is the number of network chains per unit volume and is gained from low strain tensile testing by applying Simple Rubber Elasticity Theory. N_A is Avogadro's Number and is approximately 6.022*10^{23} per mole.

$$M_c = \frac{1}{2} * \frac{x_{monomer}}{x_{cross-linker}} * mm_{monomer} \tag{3.3}$$

where $x_{monomer}$ stands for the moles of monomer, $x_{cross-linker}$ stands for the moles of cross-linker and $mm_{monomer}$ is the molar mass of the monomer. The equation is based on a cross-link functionality of 4. This is true for the organic cross-linker but unknown for the clay under consideration. As regardless of this uncertainty the given equation is employed for nanocomposite hydrogels, a fault in the calculation has to be expected. Calculations regarding molecular weight are carried out for samples NC9 and OR9.

Low strain tensile testing is performed on samples NC7, NC9, NC11, NC13, NC9_THIN, NC9_THICK and OR9.

3.3.2 Fracture Toughness Testing

Fracture toughness tests according to the trouser tear test are performed at a crosshead speed of 100 mm/min.

Fracture toughness tests according to the pure shear test are performed at a crosshead speed of 2 %/min. The test set-up and evaluation is performed according to the pure shear test as explained in detail in subchapter 2.2.4.4. The clamps used are displayed in Figure 3.3 b). At least six specimen of each material are tested, three with a notch and three without a notch. It is then decided which of the obtained curves are valid. Validity in this sense is given when the curves show sufficient smoothness since this represents little slippage of the material. Figure 3.2 schematically displays valid and invalid curves.

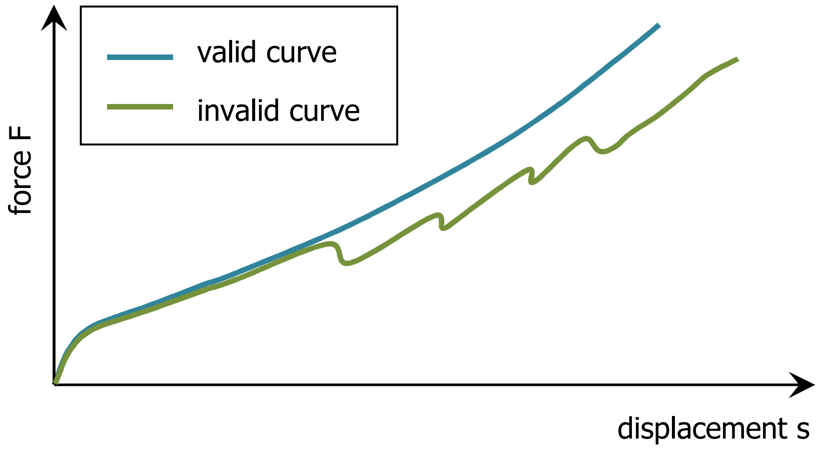

Figure 3.2: Schematic representation of valid (blue) and invalid (green) curves from fracture toughness testing.

These curves are averaged and utilized for evaluation according to (Sun et al., 2012) in order to determine the fracture toughness parameter G_c. The standard deviation of the average is calculated as a measure of scattering. Testing is performed on samples NC7, NC9, NC11 and NC13.

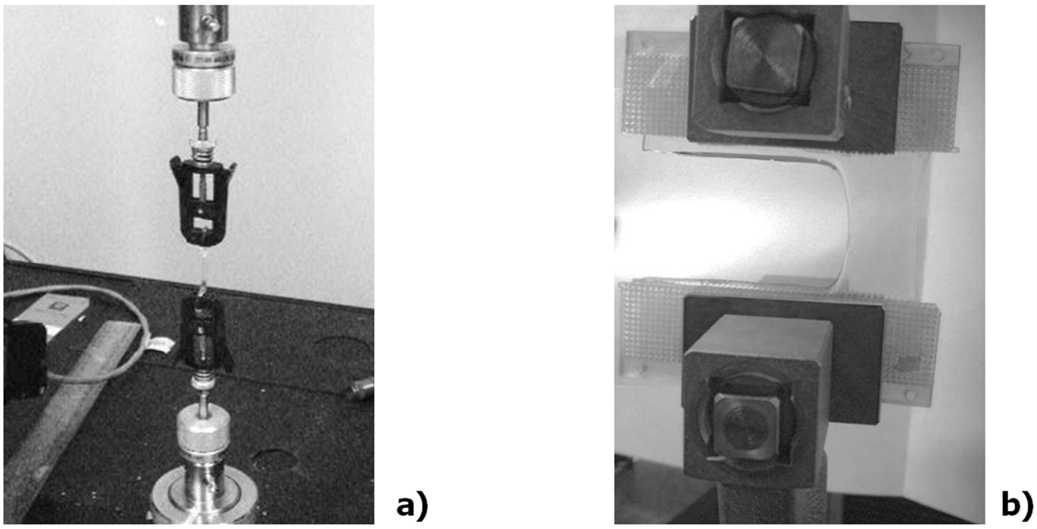

Figure 3.3: Clamps for **a)** low strain measurements and **b)** for fracture toughness testing.

3.4 Characterization of Viscoelastic Properties

As described in subchapter 2.2.4 the viscoelastic properties of elastomers play a crucial role when describing their fracture behaviour. A physical network, as sustained in this thesis by employing clay as a multifunctional cross-linker and thus providing ionic interaction, is expected to strengthen the gel. This is due to its ability of dissipating energy resulting from its distinct viscoelasticity (Hao and Weiss, 2013). For this reason in the present study, step cycle testing and stress relaxation experiments are conducted. It shall be noted that the effects of creep and stress relaxation experiments are similar with the latter favoured for distance controlled instruments. As the tensile testing machine available is distance controlled, stress relaxation experiments are chosen to be performed instead of creep experiments. Furthermore, dynamic mechanical analysis as well as rheometry testing is performed.

3.4.1 Step Cycle Testing

Step cycle testing is performed on a tensile testing machine (Instron 5566, Instron Pty Ltd., VIC) at a crosshead speed giving a strain-rate of 0.5 %/s. Specimens are loaded to a strain ε_1 (25 %), followed by an unloading cycle to 0 kpa stress. In the subsequent loading cycle the specimen is loaded to a strain ε_2 that is 25 % higher than before. Again, unloading to 0 kPa stress follows. This procedure is continued up to a strain of 400 %. The resulting stress-time profile is shown in Figure 3.4. The axial strain is recorded with a video extensometer as analogously explained in the previous subchapter for low strain tensile testing.

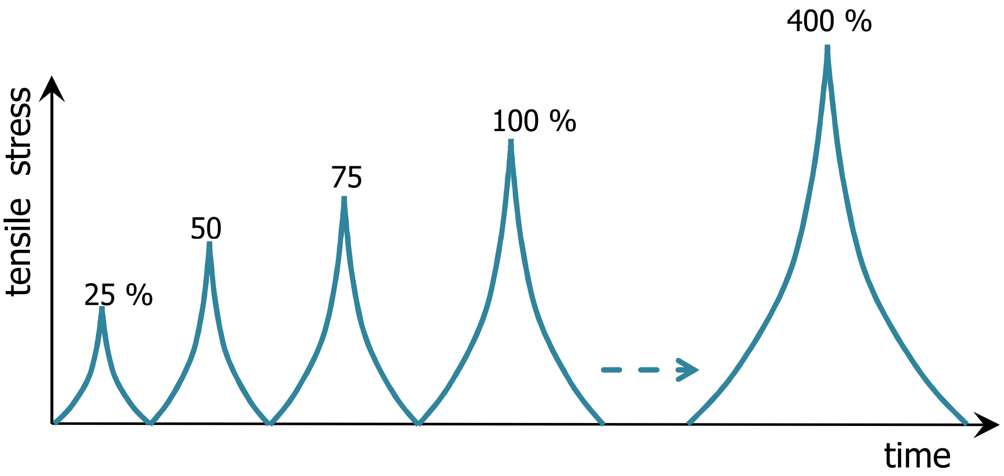

Figure 3.4: Loading profile for step cycle tests with numbers on top representing the strain.

Sometimes – depending on the initial distance between the pins – the pins exceed the view field of the video extensometer at high strains which is followed by the abruption of the measurement. Hence, evaluation is only exerted on data up to 350 %. Since the test takes several hours and nanocomposite hydrogel samples are susceptible to drying out on air, all specimens are coated with silicone oil after mounting in the tensile testing clamps. At least two specimens are tested for each sample and a representative result is chosen for evaluation. Testing is performed on samples NC7, NC9, NC11, NC13 and NC9_THICK. It shall be remarked that the strains that give the measuring profile refer to the crosshead strain. In contrast all evaluation is performed by using the video axial strain as it is recorded with a higher accuracy than the crosshead strain.

Step cycle testing is used to determine the ratio between elastic and plastic deformation. Evaluation is conducted according to Hong et al. (2004). From the tensile testing data a true stress-strain curve (σ_{true} as a function of ε_{true}) is obtained by using Eq. 3.4 and 3.5.

$$\varepsilon_{true} = \ln\left(1 + \frac{\varepsilon}{100}\right) \tag{3.4}$$

$$\sigma_{true} = \sigma * \left(1 + \frac{\varepsilon}{100}\right) \tag{3.5}$$

where ε is the engineering/technical strain in % and σ is the engineering/technical stress. From this curve the total strain for each loading cycle is readout and split into elastic and plastic strain fractions as exemplarily shown in Figure 3.5 for the second cycle. Elastic strain as well as plastic strain is then plotted as a function of total strain.

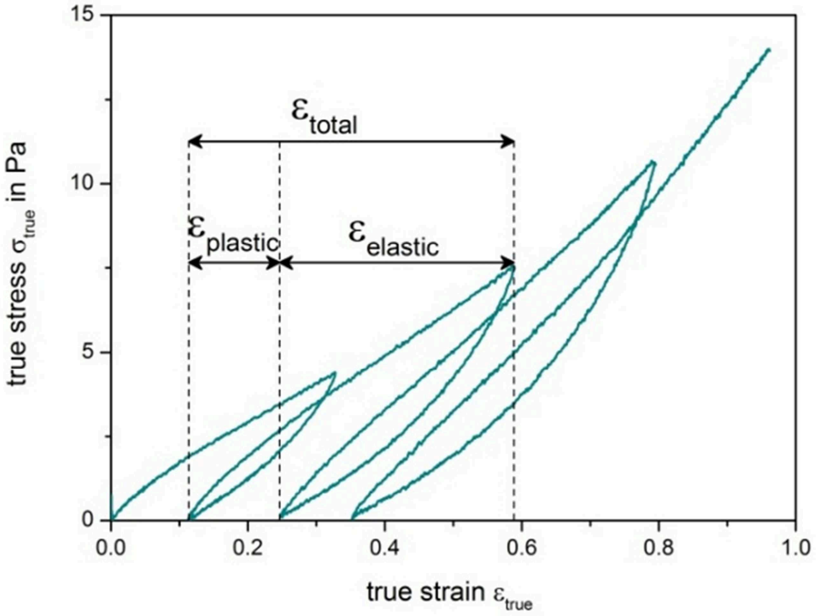

Figure 3.5: Evaluation of step cycle testing.

So as to compare results from step cycle testing with uninterrupted loading and unloading, additional testing is performed on sample NC11. The sample is once stretched to 350 % strain, followed by unloading to 0 kPa stress. Test conditions are equal to step cycle testing. Three specimens are tested.

3.4.2 Stress Relaxation Experiments

Stress relaxation experiments are performed on a tensile testing machine (Instron 5566, Instron Pty Ltd., VIC). Samples are stretched to 100 % at a constant crosshead speed of 100 mm/min. The strain is then held constant for approximately 25 min, while the tensile stress is recorded as a function of time. Evaluation of stress relaxation data employs a two-element Kelvin model as shown in Eq. 3.6 to fit the stress σ as a function of time t.

$$\sigma(t) = \sigma_\infty + \sigma_1 e^{\left(\frac{-t}{\tau_1}\right)} + \sigma_2 e^{\left(\frac{-t}{\tau_2}\right)} \tag{3.6}$$

where σ_∞ is the tensile stress at infinite time, σ_1 and σ_2 represent $E_1 * \varepsilon_0$ and $E_2 * \varepsilon_0$, respectively, τ_1 and τ_2 are the relaxation times for short and long relaxation processes, respectively. E_∞, E_1 and E_2 represent Relaxation Moduli and ε_0 represents the initial stretch. Nanocomposite hydrogels are evaluated regarding relaxations times τ_1 and τ_2 and regarding Relaxation Moduli E_∞, E_1 and E_2. It has been reported that for physically crosslinked gels similar to the ones considered in this thesis, rearrangements in the structure due to decoupling of chains from the nanodomains contribute to the stress relaxation of the network (Hao and Weiss, 2011). The shorter the stress relaxation time the faster energy can be dissipated. This relationship connects relaxation times with fracture toughness. At least three specimens are tested for each sample and averaged for evaluation. Testing is performed on samples NC7, NC9, NC11, NC13 and NC9_THICK.

3.4.3 Dynamic Mechanic Analysis

DMA measurements are performed on a solids analyzer DMA (RSA-G2, TA Instruments, DE). Strain sweeps are performed to determine the linear-viscoelastic region at 1 Hz and ambient temperature. Subsequent frequency sweeps are conducted at 1 % strain in the frequency range from 0.01 Hz to 100 Hz at ambient temperature. Shear sandwich clamps are employed. To avoid slipping, samples with thickness 2 mm are squashed in shear sandwich clamps with 1 mm spacing, samples with thickness 3 mm are squashed in clamps with 2 mm spacing. At least three specimens are tested for each sample. A representative is chosen for evaluation. Evaluation is performed regarding Storage Modulus, Loss Modulus and loss factor each as function of frequency. Testing is performed on samples NC7, NC9, NC11, NC13, NC9_THICK and OR9.

3.4.4 Rheometry Measurements

Rheometry measurements are performed on an AR-G2 device (TA Instruments, DE). The set-up is a parallel plate configuration where a sand-blasted stainless steel plate is employed as upper plate and a stainless steel Peltier plate is employed as lower plate that additionally controls the temperature. The gap width is set accordingly to the sample thickness. For 3 mm thick samples the gap is set to about 2.6 mm, for 2 mm thick samples to about 1.6 – 1.7 mm and for 1 mm thick samples to about 0.7 mm. It is aimed to achieve a normal force of about 15 N when lowering the upper plate to the gap width in order to keep test conditions as comparable as possible for all samples. Strain sweeps are performed to determine the linear-viscoelastic region at 1 Hz and 25 °C. Subsequent frequency sweeps are conducted at 10 % strain and 1 % for nanocomposite hydrogels and organically cross-linked gels, respectively. Temperature is held constant at 25 °C. Evaluation is performed regarding Storage Modulus, Loss Modulus and loss factor each as function of frequency. Additional strain sweeps are performed at 1 Hz in a strain range from 0.01 % to 1000 % strain to study the Payne Effect. At least three specimens are tested for each sample and averaged for evaluation. Evaluation is performed regarding Storage Modulus, Loss Modulus and loss factor, each as function of strain. Samples tested are NC7, NC9, NC11, NC13, NC9_THICK and OR9.

4 RESULTS

In this chapter the results of the project are discussed. Firstly the development of an appropriate sample preparation technique is addressed. Additionally, different analytical characterizations verify the chosen preparation process. Secondly, mechanical properties will be discussed with a focus on viscoelasticity and fracture toughness. Moreover, this chapter aims to point out similarities and differences in material behaviour between nanocomposite hydrogels and neat and filled elastomers.

4.1 Sample Preparation of Nanocomposite Hydrogels

The following section aims to discuss the development of a sample preparation technique for preparing nanocomposite hydrogels with clay as cross-linker. Furthermore, a variation to produce samples with an organic cross-linker instead of clay is given.

The tasks of the development of the sample preparation are in principle the following:

- selection of suitable raw materials (solvent, monomer, cross-linker, initiator, possibly accelerator)
- development of stirring process
- confirmation of suitable polymerization conditions
- establishment of a mould
- development of the moulding process

Hydrogels per definition contain water as solvent which makes the choice of solvent inapplicable. As a first approach, following examples stated in literature *N*-isopropylacrylamide (NIPA) is chosen as monomer while Laponite XLG® is chosen as an inorganic cross-linker (Haraguchi and Li, 2006). Laponite XLG® is a synthetic hectorite containing 59.5 % SiO_2, 27.5 % MgO, 2.8 % Na_2O and 0.8 % Li_2O. It soon becomes evident that PNIPA exhibits a lower critical solution temperature (LCST) in water at 30 °C (Haraguchi et al., 2005; Haraguchi et al., 2002) which is problematic. It has been reported that the LCST is highly dependent on its surrounding, e.g. on hydrophilic co-monomers (Overstreet et al., 2013). For a polymer the LCST describes a coil-globule transition. This means that below this temperature the polymer chains form flexible coils while above it the polymer forms compact globules. As a result it is expected that a non-constant room temperature might highly influence mechanical properties of the samples. The room temperature of the testing laboratory varies between 17 °C and 25 °C which is believed to be problematic as results would not be reproducible. Additionally it has been reported that the synthesis of NIPA-clay hydrogels is highly sensitive on temperature. This implies a significant complication for the practical performance of the preparation process: During the whole process temperature strictly has to be held at 0 °C (Ma et al., 2008). However, as oxygen has to be excluded throughout the polymerization process in order not to react with the monomer, this is hardly possible to realize. The influence of oxygen is theoretically described in subchapter 2.1.2.1 and studied using FT-IR analysis. The results are discussed in subchapter 4.2.2.

As a second approach, the monomer is substituted by *N′,N*-dimethylacrylamide (DMAA). For this monomer no LCST is described. An additional positive effect regarding the simplicity of sample preparation is that in contrast to NIPA which is a powder, DMAA is present as a liquid. Potassium persulfate is chosen as initiator as it is a very common initiator especially for polymerizations in water. Initially it is aspired not to use any accelerator in order to keep the procedure as simple as possible. Potassium persulfate also decomposes at elevated temperatures (Lin, 2001). It is attempted to distribute the clay in pure water before adding monomer and other components. It was determined that the output of the mixing process should be a liquid solution so as to be able to mould it in arbitrary shapes without bubbles. As simple mixing of water and clay at ambient temperature with a magnetic stirrer results (at least for clay contents higher than 2 mole%) in a very viscous gel-like solution containing many air-bubbles, various different methods are essayed. Firstly, temperature is varied: Higher temperatures up to 50 °C achieved by stirring with a magnetic stirrer on a heated plate as well as lower temperatures close to 0 °C achieved by conducting the stirring in an ice-bath do not show any different results than at ambient temperature. Another attempt to prepare a bubble-free solution is to freeze the water/clay-mixture with the magnet before starting to stir. Then stirring is carried out while unfreezing from bottom to top which is meant to prevent the formation of air-bubbles. However, also this approach leads to a very viscous solution with many bubbles, unsuitable to be moulded. Secondly, the stirring device is exchanged by substituting the magnetic stirrer with an overhead stirrer equipped with rotor blades in order to apply higher forces. However, the mixture stays very viscous resulting in the rotor blades to cavitate. Furthermore, instead of physically stirring, the mixture, containing all components and positioned in a flat container serving as mould, is placed in an ultrasonic bath. No sufficient distribution of the components can be achieved by this approach. Thirdly, appealed by literature no stirring at all is applied. Wang et al. (2009) suggested that many clay types can be exfoliated by letting time pass. However, even after weeks it is found that the clay is still not completely dispersed as is displayed in Figure 4.1. Fourthly, the monomer is added at the same time as clay as it is stated in literature that certain types of monomer interact with the clay/water mixture whereby the formation of a gel is hindered (Haraguchi et al., 2005; Haraguchi and Takehisa, 2002). However, this prohibition of gelation does not take place for the combination of Laponite XLG® and DMAA.

Figure 4.1: Clay-water mixture: After several weeks without stirring clay is not fully dispersed in water.

None of the methods results in a solution which is capable of being poured into a mould without imperfections such as bubbles. Thus the cross-linker Laponite XLG® is exchanged by a slightly modified product, Laponite XLS®. The chemical composition of Laponite XLS® is very similar to Laponite XLG®. Laponite XLS® contains slightly less SiO_2 and instead 4.1 % P_2O_5. While Laponite XLG® even at low contents of approximately 2 mole% per 1 L water forms a gel when mixed with water, Laponite XLS® does not exhibit this behaviour up to much higher contents of about 15 mole% per 1 L water. This effect is caused by the surface-modification of Laponite XLS®. Due to the negative charges on both surface and edges, clay particles repel each other and are hence not as likely to gel as Laponite XLG®. The effect is explained in more detail in subchapter 2.1.2.1. As before, the first approach is to simply stir Laponite XLS® in pure water by the use of a magnetic stirrer. A solution can be obtained up to clay contents of about 15 mole% in 1 L of water. Changes of temperature do not affect the exfoliation-behaviour of this clay, different from what is reported for clays (Kroon et al., 1998). Instead, it is found that the distribution of clay is not dependent of temperature. In order to prevent the monomer from beginning to polymerize during the mixing process, stirring is carried out at approximately 0 °C, realized by the use of an ice-bath. After roughly one hour of continuous stirring, the clay is completely distributed as evident by a change of the solution from turbid to clear. As this clay/monomer combination seems to be appropriate this choice of chemicals is maintained. Throughout the whole stirring process the vessel is closed. This is because it was found by weighing, that without a lid material is being lost, which is believed to be due to evaporation of monomer. By closing the vessel, a saturated atmosphere is created in the vessel which prevents evaporation.

Polymerization shall be ensured to be as complete as possible. Thus the solution containing all components in use (solvent, monomer, cross-linker and initiator) is poured into a simple container with a flat bottom and placed in an oven. The oven is connected to a vacuum pump as well as to nitrogen gas. Temperature is set to 70 °C, according to the decomposition of the initiator at about that temperature. Oxygen is removed by evacuating the oven, followed by purging with nitrogen gas. Evacuation and purging is repeated several times. Polymerization is allowed to take place for eight hours. The resulting sample exhibits a brownish colour accompanied by the presence of numerous bubbles of a size up to approximately 1 mm. Probably temperature is too high and thus yielding degradation of the polymer directly after or while being created. The temperature is therefore reduced to about 60 °C. However, although clear samples are obtained, a significant amount of bubbles is rather present. Presumably bubbles are caused by boiling water as the phase diagram for water yields a significant reduction of boiling point in presence of vacuum. Though, as the water is not pure but mixed with monomer, initiator and clay, no exact number for the boiling point can be given. In order to find out at which pressure bubbles occur, the vacuum pump is turned on while watching the material through a window in the oven door with a torch. It is evident that bubbles form at roughly 20 inHg. Hence, for the following attempts, the vacuum pump is stopped at about 10 inHg. However, after removing the samples from the chamber the brownish colour is present. Additionally the samples exhibit odours similar to those emanating from the monomer. It is thus concluded that (unpolymerized) monomer is still present in the samples. Variation of polymerization time does not improve the results as the brown colour is always observed. This leads to the conclusion that the current approach of triggering the initiation of the polymerization by applying temperature is not suitable. Alternatively, an accelerator (*N,N,N′,N′*-Tetramethylethylenediamine, TEMED) is employed for polymerization. Transparent, flexible material with almost no bubbles is obtained. It has been expected that the gels should be transparent and colour free. Thus, the final polymerization conditions are firstly the utilization of a chamber where the exclusion of oxygen is obtained by evacuating and purging with oxygen, secondly the employment of accelerator, thirdly a polymerization temperature of approximately 25 °C and fourthly a polymerization time of roughly 55 h.

For moulding the materials, several approaches are essayed. First, two glass slides with a rubber spacer are employed. However, the material sticks greatly to it which makes it hardly possible to remove it without damage. Second, a Teflon-coated cake tin is tested. The result is a strong bond between hydrogel and coating followed by partial removal of coating from the cake tin when the material is peeled off. Due to polytetrafluoroethylene's (PTFE) high resistance to van de Waals forces, Teflon is assumed to be a suitable material for the present purpose. Ergo, various brands of Teflon cake tins are tested, with the result of none of them being sufficient in the way that the hydrogels stick strongly to them. The reason to test different brands is the suspicion that items sold under the tradename 'Teflon' contain different amounts of PTFE. Another disadvantage is that cake tins seldom exhibit sharp edges. In order to control the sample thickness by measuring the volume in an open container, it is necessary to know the exact cross-section. This is hardly possible for cake tins. Thirdly, polypropylene (PP) boxes are tested. The peeling is found to be easier, but the surface is not completely smooth (e.g. printing on the opposite side leaving marks on surface from injection moulding). A smooth surface is necessary to allow attainment of valid test specimens such as dumbbell specimens. Fourthly, a polystyrene petri-dish is employed as a mould. Again, the sample sticks to the mould. Also a petri-dish which is coated with silicone oil is tested. Removing of the material is found to be relatively easy with the big disadvantage that the silicone oil leaves marks on the sample surface. In order to lower the silicone oil's viscosity it is diluted with Tetrahydrofurane (THF) and applied as a coating on a glass petri-dish as previously done. It is found that due to the high surface tension the layer does not distribute evenly and furthermore remains or possibly reacts with the sample. A further approach designs two glass slides that are covered with polyethylene foils. A PP frame of 2 mm in thickness builds 'walls' with the purpose of preventing outflow of the material. However, the foils form creases and additionally the solution flows into holes between 'walls' and glass slides.

A moulding technique that allows easy removing of samples with a flawless surface is found as described in the following paragraph. The mixture is poured into a very smooth PP bag bought from a packaging company. In order to ensure smooth and even sample surfaces the bag is squeezed between two glass slides. The distance between the glass slides which defines the sample thickness is regulated by gluing spacers in the correct thickness (1 mm, 2 mm and 3 mm) between the glass slides. The composition is fixed by big binder clips. Figure 4.2 illustrates the set-up.

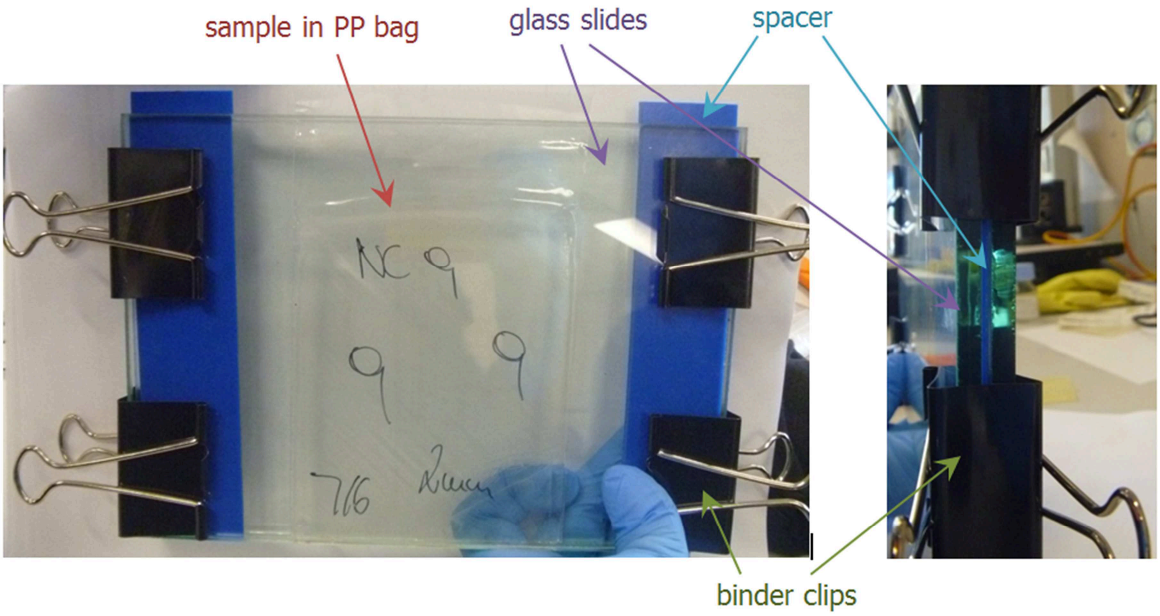

Figure 4.2: Mould used for sample preparation.

The preparation of the sample with the organic cross-linker is carried out analogously with the only difference of exchanging clay with the organic cross-linker. In order to study the effect of oxygen on the polymerization, additional samples are prepared without the step of evacuating the chamber and purging with nitrogen.

4.2 Investigation and Approval of Sample Quality

In order to approve the applied processing procedure in terms of sample quality, FT-IR spectroscopy, XRD and TEM are applied. The results are discussed in the following.

4.2.1 Visual and Tactile Assessment

The prepared samples are investigated in regard to their visual and tactile characteristics. Figure 4.3 shows images of prepared nanocomposite hydrogels. In the left an adequate sample prepared following the procedure above is shown. The sample is transparent and exhibits few small bubbles that are interpreted as being negligible. In the right an inadequate sample prepared following discarded attempts is shown. The sample exhibits low transparency. It is evident that the sample deforms plastically during removal from the mould. The colour is brownish and is getting slightly stronger with time.

The visual assessment of the samples which are found to be adequate results in the following observations: All nanocomposite hydrogel samples regardless of thickness and clay content are equally transparent. They exhibit very small and few bubbles that are rated as not significant. The traditionally cross-linked hydrogel sample OR9 shows a transparency similar to the nanocomposite hydrogels. The number of bubbles present in this material is higher. All samples exhibit a very smooth surface.

Figure 4.3: Comparison of samples with adequate (left) and inadequate (right) sample preparation.

The tactile assessment of the samples shows that the nanocomposite hydrogel samples with thickness 2 mm and 3 mm feel relatively non-sticky. It is found that the stickiness increases with decreasing clay content. In comparison to the samples with a thickness of 2 mm and 3 mm, the sample with 1 mm thickness feels very sticky when touching the surface. As discussed above, sample material has to be peeled from surrounding PP-films before testing. The peeling of 1 mm thick samples is very hard and often not possible. It is found that while the preparation of 2 mm and 3 mm thick samples is very reproducible, the 1 mm thick samples vary highly in quality, partly resulting in the just stated stickiness. This is probably due to an incomplete polymerization. The following assumptions lead to this theory: Firstly it is assumed that oxygen disturbs the polymerization process. Secondly it is assumed that keeping the components at ice bath temperature prevents the monomer from starting to polymerize during stirring. The major difference between thin and thick samples in the preparation process is the amount of thermal mass that is filled into the plastic bags as explained in the previous chapter. Warming-up of the thinner material presumably happens comparatively fast. This results in a more rapid start of the polymerization. As a consequence, polymerization already happens while the material is still surrounded by oxygen – resulting in shorter polymer chains – due to the fact that it takes some time to place the arrangement in a chamber, evacuate it and purge it with nitrogen. As for the 2 mm and 3 mm thick samples the larger thickness is assumed to keep the material from warming-up for a period long enough to exclude oxygen before polymerization begins.

When squeezing nanocomposite hydrogel samples between fingers or pressing the thumb into them, they appear soft. After removal of pressure, they retain their original shape and without remaining indentation marks. Softness seems to increase with decreasing clay content. In contrast, sample OR9 feels hard when it is squeezed between fingers and instantly crumbles when it is rubbed between fingers.

4.2.2 Spectroscopic Analysis - Infrared Spectroscopy

Figure 4.4 to Figure 4.6 show spectra gained from FT-IR analysis. The ordinate does not exhibit a scale as only qualitative evaluation is performed. Hence no numbers are given for transmission. Figure 4.4 shows the spectra gained from FT-IR measurements for samples NC9, OR9 and pure clay. The peaks around 1000 cm^{-1} and 650 cm^{-1} are attributed to the Si-O and Si-O-Si bonds, respectively (Haraguchi et al., 2010). Thus they are directly ascribed to the clay. This is in agreement with the presence of these peaks in spectra of pure clay and sample NC9 and the absence of these peaks in the spectra of sample OR9. The absorption band at about 3420 cm^{-1} is interpreted as O-H stretching vibration. Since the clay has not been dried before the performance of spectroscopy, the large peak at 3420 cm^{-1} is attributed to remaining water in the clay. The peak at about 1620 cm^{-1} is interpreted as amide I band or as C=C stretching vibration, while that at about 1500 cm^{-1} is assumed to be an amide II band (Wang et al., 2011). As both peaks arise from the monomer this is in agreement with the presence of these peaks in spectra of both samples NC9 and OR9. An additional peak in spectra of samples NC9 and OR9 is at 617 cm^{-1} which is attributed to an amide IV band and is hence associated to the monomer. As all peaks that might be independent of clay are overlain by clay or water in clay, normalization of hydrogel spectra is not possible. Hence, no quantitative evaluation can be performed.

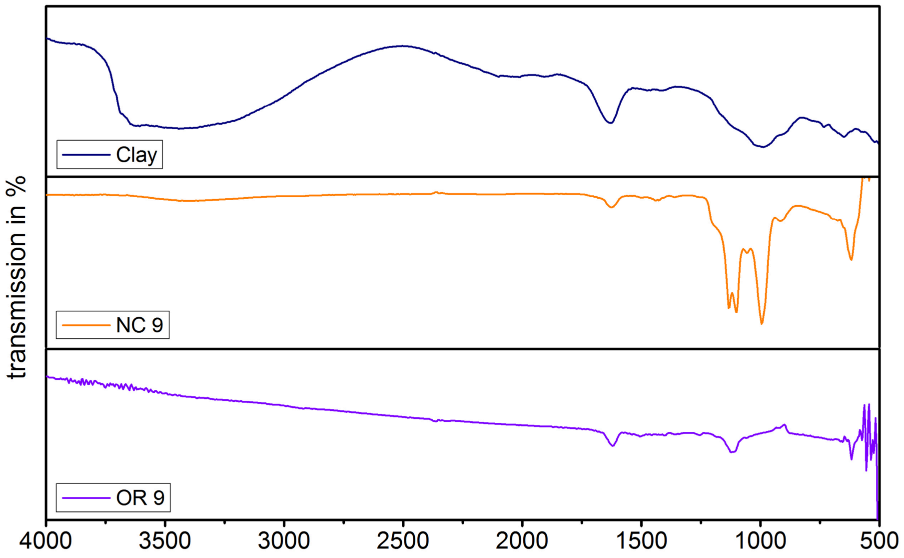

Figure 4.4: FT-IR spectra of pure clay, samples NC9, OR9.

Figure 4.5 shows FT-IR spectra of samples NC7, NC9, NC11 and NC13. No significant effect of the clay content on the general curve progression is discernible. The similarity of the spectra can be taken as indication for a nearly equal polymerization process resulting in the same functional groups. The only noteworthy discrepancies are discernible between wavelengths of 1000 cm^{-1} and 1200 cm^{-1}. Samples NC7 and NC11 exhibit a peak at 1000 cm^{-1} with a shoulder between 1030 cm^{-1} and 1140 cm^{-1}. In the spectrum of samples NC9 and NC13 this shoulder is substituted by a double-peak. However, no explanation for this appearance can be given. The difference in the size of the peaks – in particular of the remarkable peak at 1620 cm^{-1} – can be disregarded as no normalization of the spectra was performed.

The visual and tactile assessment of prepared nanocomposite hydrogel samples is followed by the assumption that sample NC9_THIN reacts with oxygen during the polymerization process and hence exhibits a lower molecular weight than the other nano-composite hydrogels. It is believed that oxygen reacts to radical ends of the growing polymer chains as well as to the radicals originating from the initiator. Chemical equations showing the reaction mechanism between the growing polymer chain and oxygen are given in subchapter 2.1.2.1. For the clarification of the hypothesis about oxygen influence, an additional sample (NC9_AIR) is prepared. The polymerization of sample NC9_AIR is performed in air, i.e. without excluding oxygen.

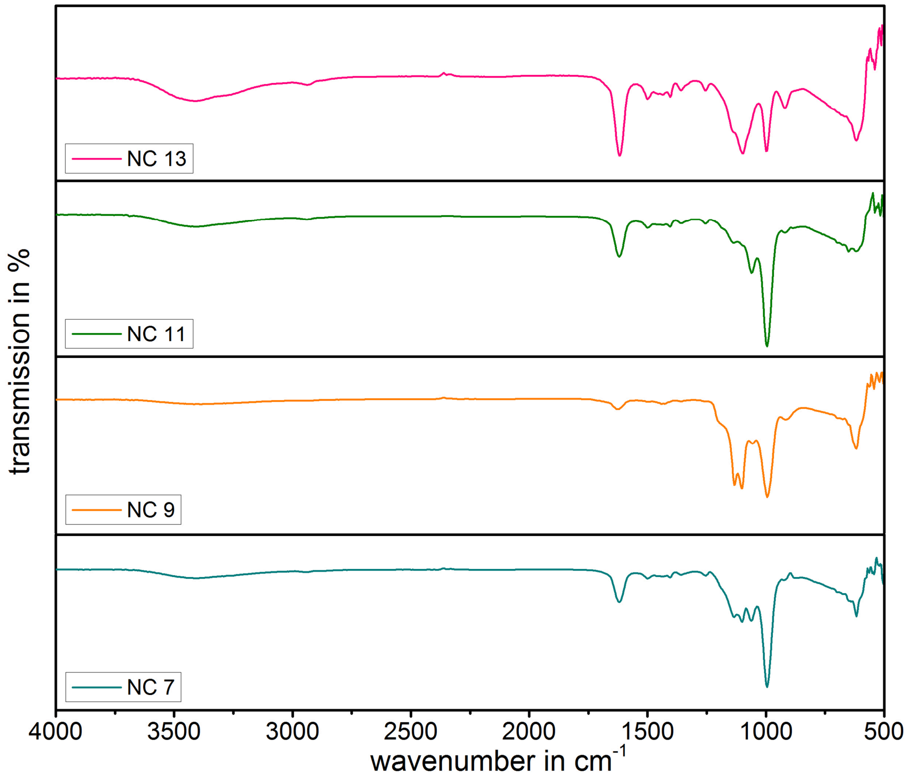

Figure 4.5: FT-IR spectra for samples NC13, NC11, NC9, NC7.

Figure 4.6 shows FT-IR spectra of samples NC9, NC9_THICK, NC9_THIN and NC9_AIR in order to discuss influence of sample thickness combined with oxygen influence. As described above the peak at 3420 cm^{-1} is interpreted as O-H stretching vibration. This peak is particularly distinct for samples NC9_THIN and NC9_AIR. Probably this peak arises from clay for samples NC9 and NC9_THICK, however it is intensified by the additional influence of oxygen for samples NC9_THIN and NC9_AIR. It is concluded that additional OH-end groups are formed by the reaction of oxygen in the polymerization process. Further, for both sample NC9_AIR and sample NC9_THIN a peak at about 1600 cm^{-1} occurs that is not present for other nanocomposite hydrogel samples. However the peak is partly overlain by other peaks. Hence, it cannot distinctly be attributed to a certain vibration. Additionally the absorption at around 800 cm^{-1} is equal for both NC9_THIN and NC9_AIR. This peak might be caused by a tertiary alcohol, in particular by the deformation vibration of C-O. This supports the assumption that the polymerization process is sensitive to oxygen. No significant discrepancies between spectra of sample NC9 and NC9_THICK are perceptible other than the double-peak of sample NC9 described above. Thus, any effects caused by increasing sample thickness to more than 2 mm are either not present or not strong enough to be detectable in FT-IR spectroscopy.

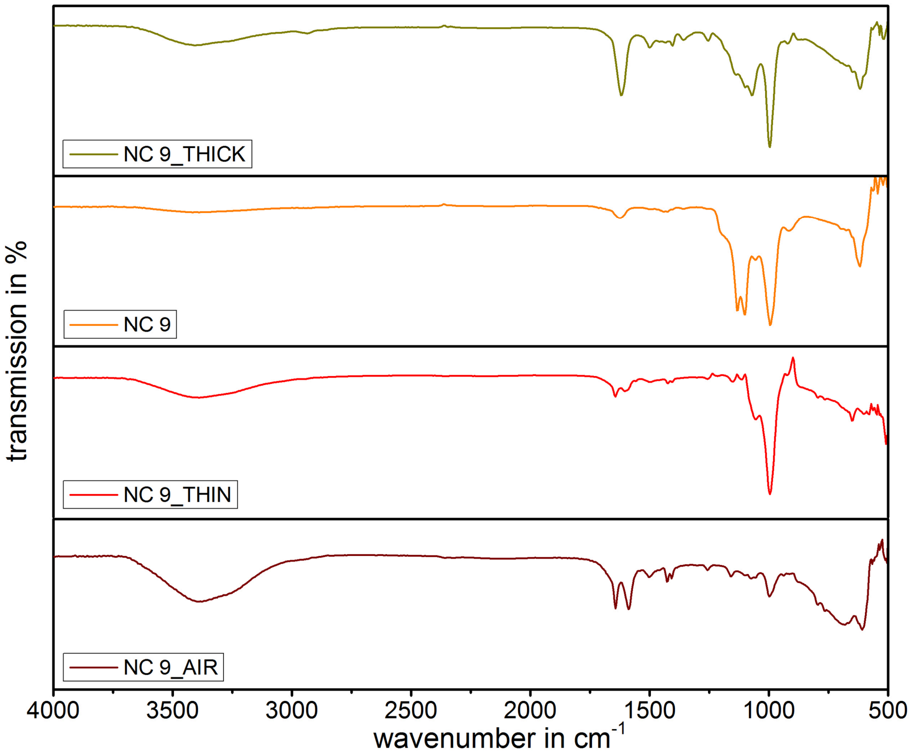

Figure 4.6: FT-IR spectra for samples NC9_THICK, NC9, NC9_THIN, NC9_AIR.

4.2.3 Thermo-gravimetric Analysis (TGA)

Figure 4.7 a) shows weight in % as a function of temperature for the samples NC7, NC9, NC11 and NC13 determined by TGA. The decrease in weight is attributed to the evaporation of physically bound water in the samples. At 80 °C a plateau is reached, indicating water to be evaporated. The residual mass represents the polymer/clay network. Water content of all samples is around 72-75 %.

Figure 4.7 b) shows weight in % as a function of temperature for pure clay as received from the company determined by TGA. For clay no plateau is reached. The weight continuously decreases with increasing temperature. However, physically bonded water (approximately 12 %) is evaporated below 100 °C. After the evaporation of physically bound water the initially large slope of the curve promptly declines. Thus, above approximately 100 °C the curve decreases only slightly. As it is believed that chemically bound water (crystal water) would evaporate rapidly within a small temperature range, the further decreasing of weight cannot be interpreted as a continuing evaporation of water. Instead the decline is probably attributed to the dehydroxylation of clay as reported for several other types of clay and clay-like minerals (Mielenz et al., 1953). As mentioned above, the decrease of weight after evaporation of physically bound water is absent for nanocomposite hydrogels. This difference between pure clay and clay that is part of the nanocomposite hydrogel network has to be associated with complex interactions between clay and polymer. However, no detailed explanation can be given.

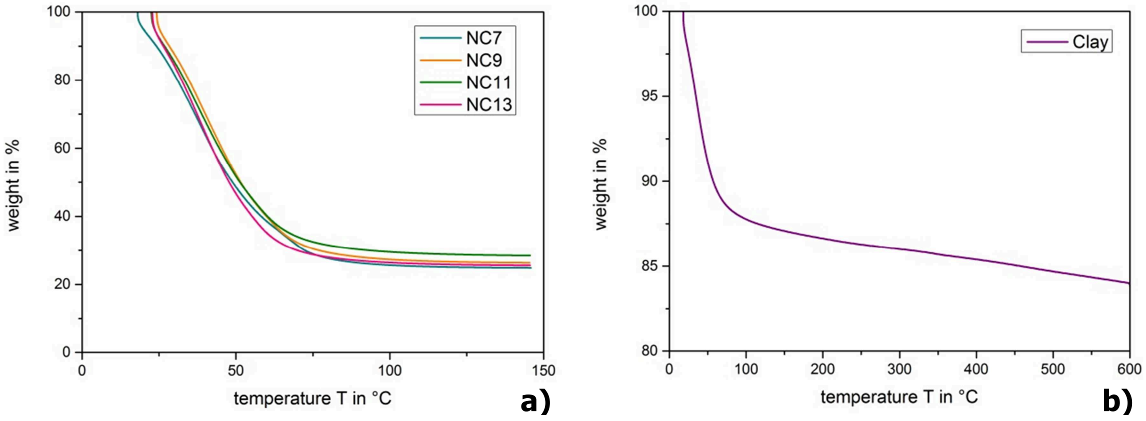

Figure 4.7: Weight as a function of temperature for **a)** samples NC7, NC9, NC11, NC13 and **b)** pure clay.

4.2.4 Morphological Analysis

In order to study the structure and morphology of prepared nanocomposite and organically cross-linked hydrogel samples XRD and TEM is conducted. The major aim of this subchapter is to discuss exfoliation and uniform distribution of clay.

4.2.4.1 X-Ray Diffractometry

Figure 4.8 shows XRD-spectra of the samples NC7, NC9, NC11 and NC13 as well as of pure clay as received. The clay exhibits a diffraction band (peak) with a centre at about 6.5 °. According to the Bragg’s Law the basal spacing of the clay is about 1.4 nm, corresponding to the peak at 6.5 °. All nanocomposite hydrogel samples show a similar curve. The different levels in intensity might be related to the grade of coarseness that is gained by grinding the samples to powder. No diffraction bands are present in the measured scattering angle range. Thus it is concluded that clay in the hydrogel samples does not layer regularly but instead exfoliates and disperses randomly.

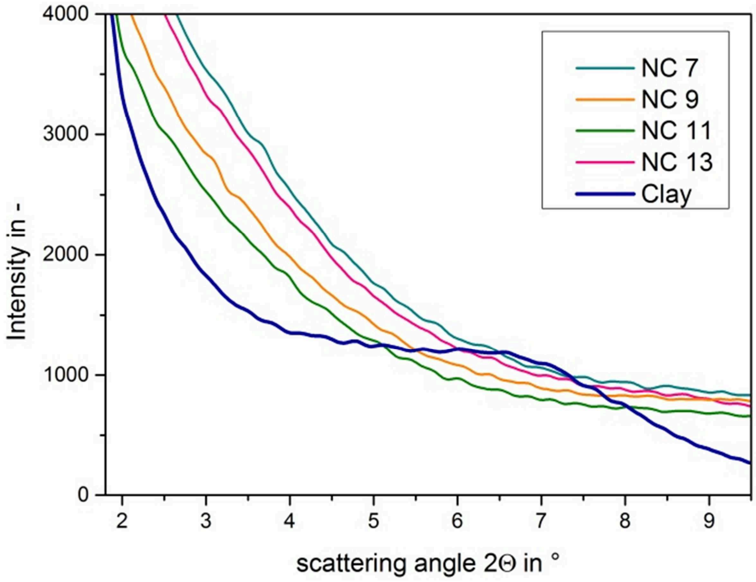

Figure 4.8: XRD-spectra of samples NC7, NC9, NC11, NC13, pure clay.

4.2.4.2 Transmission Electron Microscopy

Figure 4.9 a) to e) show TEM-images of samples OR9, NC7, NC9, NC11 and NC13 with a magnification of 100,000. No particles are evident in sample OR9 as displayed in Figure 4.9 a). In contrast, all nanocomposite hydrogel samples exhibit particles of longish shape with a length of approximately 20 to 30 nm and a thickness of approximately 1 to 1.5 nm. Hence, it is assumed that the particles displayed are exfoliated clay sheets. This is in accordance with findings in literature (Haraguchi et al., 2005) where the clay is reported to be disk shaped with a diameter of 30 nm and a thickness of 1 nm. Thus it can be concluded that by means of the developed sample preparation for nanocomposite hydrogels, clay is exfoliated sufficiently and dispersed uniformly. No significant differences between samples NC7, NC9, NC11 and NC13 which are displayed in Figure 4.9 b) to Figure 4.9 e) can be found. As the samples vary in specimen thickness (between 70 and 90 nm) and hence clay particles from different depths can be seen, no statement about the amount of clay particles per unit volume can be made. Due to the high sensitivity of charging and the low stability in the electron beam no images with higher magnifications (allowing more accurate measurements on clay platelets) are recordable.

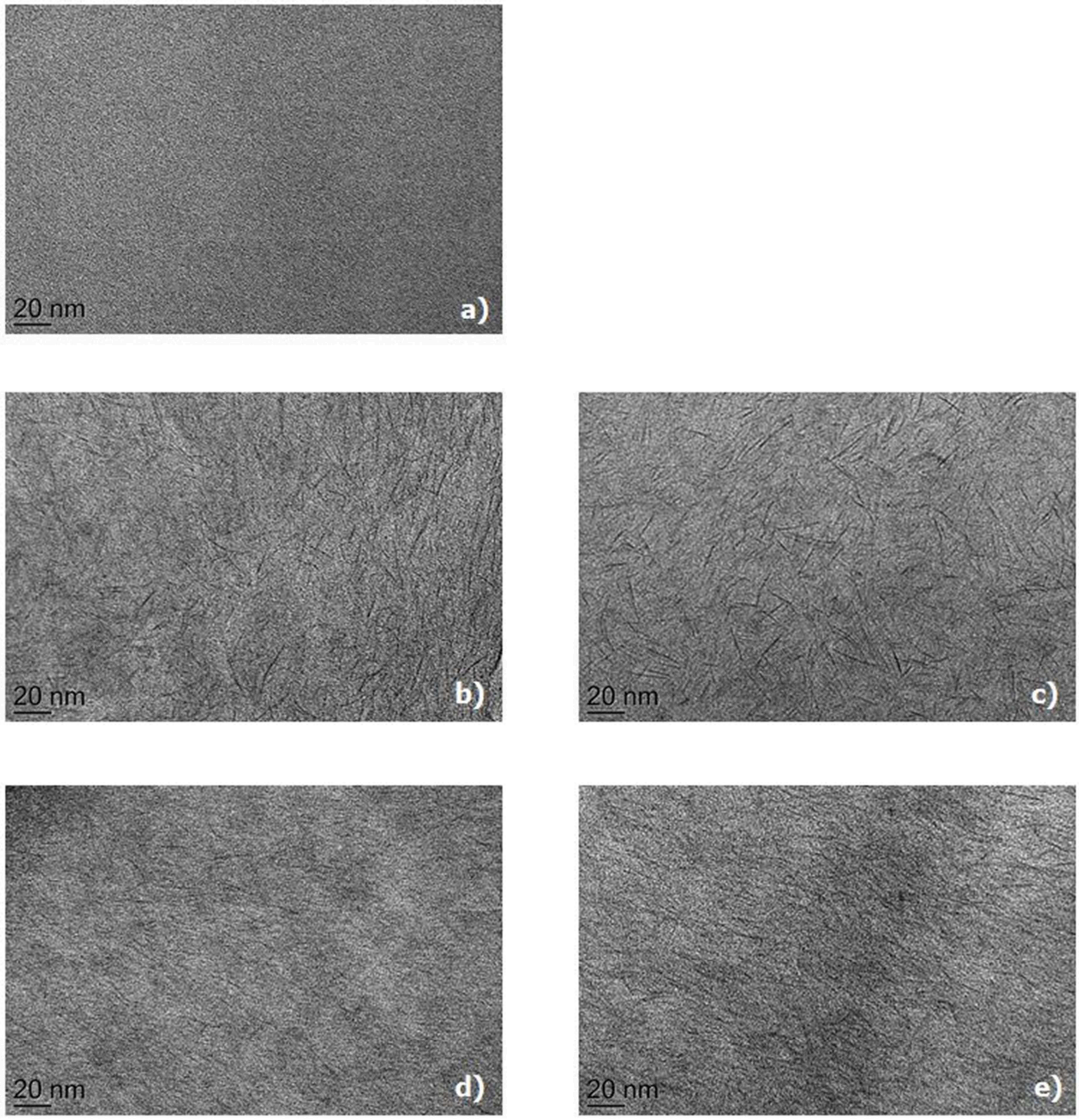

Figure 4.9: TEM-images of a) OR9, b) NC7, c) NC9, d) NC11, e) NC13.

No final proof can be given that structures observed in dehydrated samples (as utilized for imaging here) equal those in hydrated samples. However, it is naturally assumed that during drying the clay platelets would not move further apart. A possible approach to obtain TEM-images of the structure equal to the hydrated state would be the exertion of cryo-microtoming followed by cryo-electron microscopy. Following this technique, samples are cooled with liquid nitrogen and then sectioned into ultrathin films. While positioning the samples in the microscope chamber and performing imaging they are constantly cooled at liquid-nitrogen. Therefore, evaporation of water is prevented and structures are hindered from collapsing. This technique could not be applied in this study as necessary appliances for this purpose were not available.

4.3 Characterization of Mechanical Properties

In order to describe mechanical properties of nanocomposite hydrogels as well as to compare them to mechanical properties of organically cross-linked hydrogels, tensile testing and fracture toughness testing is performed. The following subchapters discuss material properties such as Young’s Moduli and fracture toughness. Several theories to describe the hydrogel’s material behaviour are applied and evaluated.

4.3.1 Low Strain Tensile Testing

The following paragraphs discuss results obtained from low strain tensile testing. Low strain in this case means that the tests are stopped when the sample is strained beyond the limit of the video extensometer, typically between 300 % and 400 % if no rupture occurs prior to that (which is the case for all nanocomposite hydrogel samples except sample NC9_THIN). The results are discussed regarding the hydrogel’s mechanical properties such as the Young’s Modulus and the stress at a defined strain as well as regarding similarities or discrepancies from the Simple Rubber Elasticity Theory and the Mooney-Rivlin Theory. Additional calculations regarding the number of network chains per unit volume between cross-links are conducted. As to show proof of the reproducibility of low strain tensile testing, Figure 4.10 exemplarily displays three stress-strain curves of sample NC11. It can be seen that up to approximately 200 % the curves absolutely overlap each other. Also at larger strains the curves are very similar.

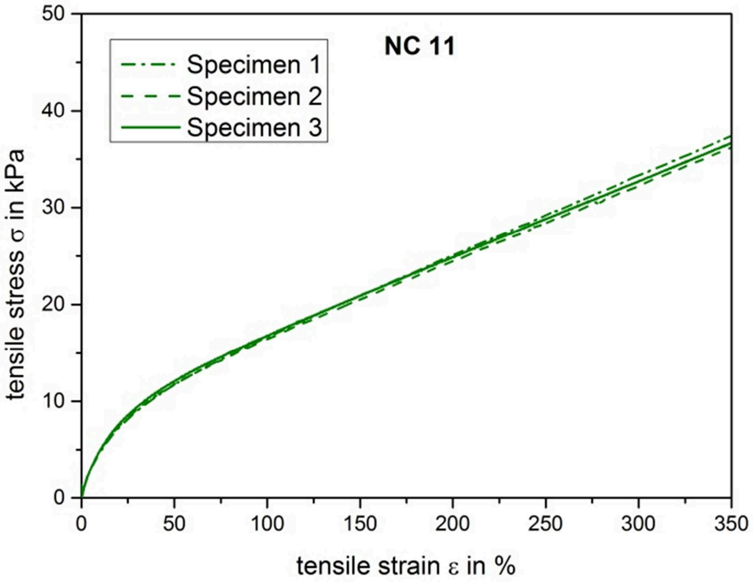

Figure 4.10: Exemplary curves displaying reproducibility of low strain tensile testing.

Figure 4.11 a) shows the stress-strain curves for samples NC7, NC9, NC11 and NC13. With increasing clay content higher stress levels for the same strains are reached. It has to be remarked that the Elastic Modulus for soft materials is commonly evaluated by conducting dynamic mechanical analysis (DMA) instead of tensile testing. Therefore the values shall only be used to compare the samples prepared for this thesis among each other. An increase of clay content leads to higher values for the Young's Modulus. The Young's Moduli (also compiled in Table 4.1) are 31 kPa and 38 kPa for samples NC7 and NC9, respectively, and 58 kPa and 99 kPa for samples NC11 and NC13, respectively. These values are in good agreement with results reported in (Haraguchi et al., 2002) and (Haraguchi and Li, 2006) for nanocomposite hydrogels composed of a similar type of clay (Laponite XLG®) and monomer NIPA. However, the stress at a strain of 350 % ranging from 17 kPa for sample NC7 to 42 kPa for sample NC13 is lower than for the hydrogel referred to above. This hydrogel is stated to exhibit stresses at the same strain (350 %) of approximately 50 kPa and 140 kPa for samples with clay contents equivalent to NC5 and NC10, respectively. The Shear Modulus is derived from the Young's Modulus of the samples. The gained values which are also given in Table 4.1 are 10 kPa and 13 kPa for samples NC7 and NC9, respectively, and 19 kPa and 33 kPa for samples NC11 and NC13, respectively. For all nanocomposite hydrogel samples with a thickness of 2 mm the elongation at failure is greater than the travel of the crosshead. This elongation corresponds to a strain of approximately 1250 %. As no fracture occurs for nanocomposite hydrogel samples under consideration, the area under the stress-strain curve cannot be calculated. However, this area and thus toughness of these samples are predicted to be high.

Figure 4.11 b) shows the stress-strain curves for samples NC9, NC9_THIN and NC9_THICK. Sample NC9_THICK exhibits a marginally higher stress level than sample NC9 at strains larger than 50 %. This is probably caused by sample preparation. As discussed in previous subchapters 4.2.1 and 4.2.2 sample thickness presumably influences the polymerization process. The preparation of a sample with a comparably large thickness of 3 mm presumably yields a slightly higher molecular weight than the preparation of samples with a thickness of 2 mm. Another possible reason for the discrepancy is different ratio of width to thickness. The variation of this ratio might lead to a change in the deformation mechanics. Sample NC9_THIN exhibits a completely different stress-strain curve. Within the first 25 % of strain a comparatively steep increase in tensile stress of about 7 kPa is exhibited. This is followed by a significant reduction in the slope of the stress-strain curve. Between 50 % and 350 % the stress only increases by 1.4 kPa, which is interpreted as viscous flow. This is an indicative of few or no stable cross-links since it is assumed that a cross-link requires a minimum molecular mass. In contrast to all other nanocomposite hydrogel samples, for sample NC9_THIN fracture is observed within the limitation of the crosshead travel. It has to be stated that standard ISO 37:2011 regulates specimen geometries for tensile testing. As sample NC9_THIN exhibits a thickness of 1 mm its specimen's width and length are demanded to exhibit half of the dimensions of the size of all other specimens with a thickness of 2 mm or 3 mm. Nonetheless this may not have any effect on the shape of the stress-strain curve (provided that the stress state is equal). Probably the procedure for sample preparation is not appropriate for the sample geometry with a thickness of 1 mm. This is in agreement with the tactile assessment of sample NC9_THIN as described in subchapter 4.2.1. Discussion and interpretation of this observation is also given in more detail in this subchapter. The results are in agreement with results gained from FT-IR spectroscopy as discussed in subchapter 4.2.2. As sample NC9_THIN exhibits lower mechanical properties and a much lower toughness than all other nanocomposite hydrogel samples it is excluded from any further mechanical testing and evaluation.

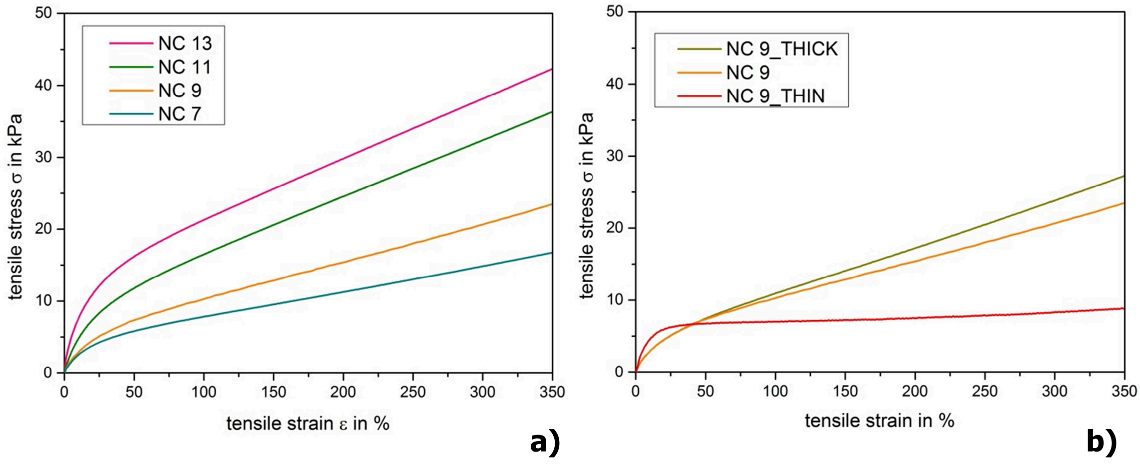

Figure 4.11: Stress-strain curves **a)** for samples NC7, NC9, NC11, NC13 **b)** for samples NC9, NC9_THIN, NC9_THICK.

Figure 4.12 shows the stress-strain curve for sample OR9. In contrast to all nanocomposite hydrogel samples with a thickness of 2 mm or 3 mm fracture occurs within the limit of the video extensometer. The strain-at-break is approximately 10 % while the stress-at-break is approximately 30 kPa. In contrast to the other samples, the Young's Modulus of 380 kPa is evaluated by the slope of the whole curve. The derived Shear Modulus is 126 kPa (see also Table 4.1). The comparison to sample NC9 reveals that the Young's Modulus of sample OR9 is approximately an order of magnitude higher than that of sample NC9.

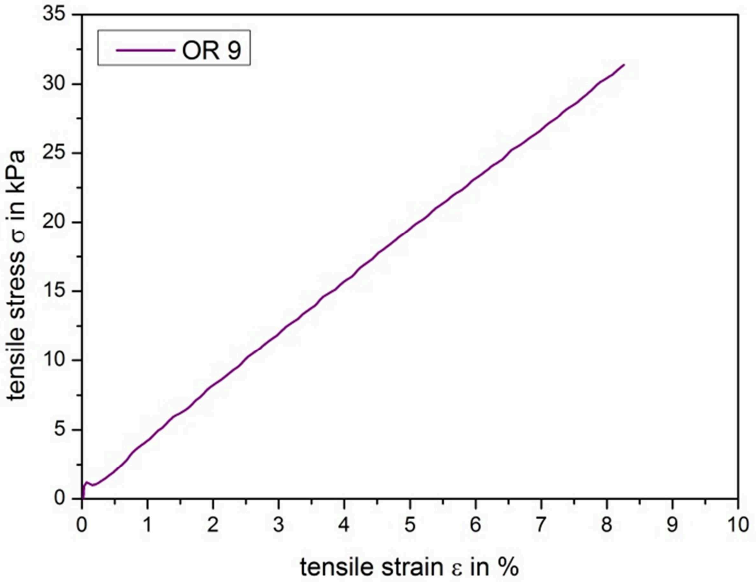

Figure 4.12: Stress-strain-curve for sample OR9.

Figure 4.13 a) shows the Rubber Elasticity Plot for samples NC7, NC9, NC11 and NC13. Materials following Rubber Elasticity Theory exhibit a linear relationship between stress and $(\lambda - \frac{1}{\lambda^2})$, where λ is the elongation ratio. However, none of the nanocomposite hydrogels investigated within this study shows a linear relationship. Instead, a bi-linear curve with a relatively sharp bend at $\left(\lambda - \frac{1}{\lambda^2}\right) \approx 0.5$ is exhibited. Hence, Rubber Elasticity Theory is not fully suitable to describe the nanocomposite hydrogel's material behaviour, although the curve displays linear regions. This curve is split into two consecutive linear graphs with different slopes. The Shear Modulus is estimated employing the first part $(0 < \left(\lambda - \frac{1}{\lambda^2}\right) < 0.4)$ while the number of network chains per unit volume between cross-links is estimated by employing the second part $(1 < \left(\lambda - \frac{1}{\lambda^2}\right) < 4)$. Results for the Shear Modulus and the number of network chains are given in Table 4.1. In analogy to the Young's Modulus, an increase of the clay content leads to higher values for the Shear Modulus. The Shear Modulus is about 7 kPa and 9 kPa for samples NC7 and NC9, respectively and 15 kPa and 21 kPa for samples NC11 and NC13, respectively. The number of network chains increases with increasing clay-content and ranges between $7.5*10^{17}$ and $1.9*10^{18}$ per cm^3. An exemplary corresponding calculation is given in the appendix. The number of chains per unit volume is approximately one to two magnitudes lower than in the similar system mentioned above and reported in (Haraguchi et al., 2002).

Figure 4.13 b) shows the influence of sample thickness on the Rubber Elasticity Plot using samples NC9 and NC9_THICK. The plots almost equal each other. Thus, no significant effect of the sample thickness on the applicability of the Rubber Elasticity Theory is discernible. The number of network chains between cross-links and the Shear Modulus is $1.8*10^{18}$ per cm^3 and 9 kPa, respectively, for sample NC9_THICK.

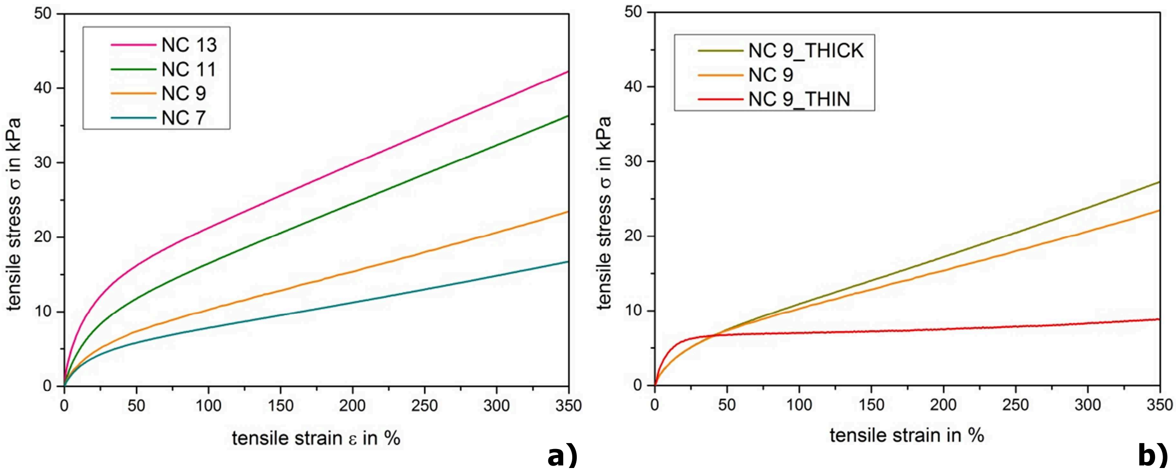

Figure 4.13: Rubber Elasticity Plot **a)** for samples NC7, NC9, NC11, NC13 **b)** for samples NC9, NC9_THICK.

Figure 4.14 shows the Rubber Elasticity Plot for sample OR9. In contrast to the nanocomposite hydrogels this sample displays a linear relationship between stress and $\left(\lambda - \frac{1}{\lambda^2}\right)$. The correlation coefficient for a linear fit is 0.999 when the small irregularity at the very left side of the curve is excluded, implying an almost ideal linearity. Therefore sample OR9 follows the Simple Rubber Elasticity Theory. Evaluation regarding Shear Modulus and number of network chains per unit volume is conducted by employing the whole graph. Results are given in Table 4.1. The Shear Modulus is approximately 136 kPa while the number of network chains is approximately $3.3 * 10^{19}$ per cm^3. Both values are about a magnitude higher than those for the nanocomposite hydrogel samples. As Rubber Elasticity Theory readily describes the material behaviour of organically cross-linked hydrogels such as considered in this thesis no further theories are applied on sample OR9.

In order to compare average molecular masses of polymer strands between cross-links found from experiment with values found from theoretical calculation, samples NC9 and OR9 are evaluated using Eq. 3.2 and 3.3 as explained in subchapter 3.3.

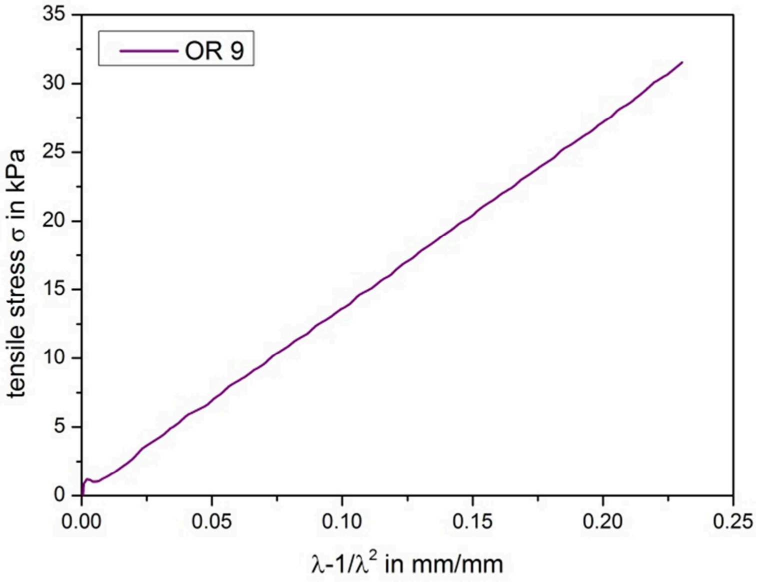

Figure 4.14: Rubber Elasticity Plot for sample OR9.

The estimation of the molecular mass from synthesis and experiment requires some assumptions: Firstly, it is assumed that monomer fraction equals polymer fraction in the prepared hydrogel. This is justified by the expectation that on the one hand not all monomer will react but on the other hand not all polymer participates in the network structure and is supported by literature (Haraguchi et al., 2003). Secondly, the hydrogels are assumed to exhibit a density of 1 g per cm^3 as they contain about 80 % of water by volume. Also the clay is assumed to exhibit a density of 1 g per cm^3 as specified by the manufacturer. Thirdly, the number of chains per unit volume is found from experiment after application of Simple Rubber Elasticity Theory. This is valid for sample OR9 but questionable for sample NC9. Resulting molecular weights for samples NC9 and OR9 are given in Table 4.2 while corresponding calculations are presented in the appendix. As the monomer content is identical for all prepared samples and the cross-linker content in moles is equal for both sample NC9 and sample OR9, the theoretical calculation of the molecular mass of polymer chains between cross-links yields the same result for the mentioned samples. However, as previously mentioned, an underlying assumption for the applied equation is a functionality of four of the cross-linker under consideration. This can only be taken for granted for the organic cross-linker in sample OR9. In contrast, clay probably exhibits a much higher functionality. Results are given in Table 4.2.

Table 4.1: Properties of hydrogels found from low strain tensile testing.

Sample	**Young's Modulus** (gained from Stress-Strain Curve)	**Shear Modulus** (gained from Young's Modulus)	**Shear Modulus** (gained from Rubber Elasticity Plot)	**Number of Network Chains per Unit Volume** [1] (gained from Rubber Elasticity Plot)
-	**kPa**	**kPa**	**kPa**	**cm^{-3}**
NC7	31	10	7	$7.5 * 10^{17}$
NC9	38	13	9	$1.1 * 10^{18}$
NC11	58	19	15	$1.7 * 10^{18}$
NC13	99	33	21	$1.9 * 10^{18}$
NC9_THICK	36	12	9	$1.4 * 10^{18}$
OR9	378	126	136	$3.3 * 10^{19}$

Table 4.2: Molecular weight of polymer chains between cross-links.

Sample	**Molecular Weight of Polymer Chain between Cross-links**	
	from Theory	**from Experiment**
-	**g / mole**	**g / mole**
NC9	1100	86800
OR9	1100	3000

The large molecular weight calculated from experiment for sample NC9 in comparison with the considerably lower number for sample OR9 suggests that the chains between cross-links in the nanocomposite hydrogel are significantly longer and hence more flexible

---

[1] The curves utilized for the calculation of the number of network chains per unit volume displayed two almost linear regions with a different slope. In order to calculate the number of network chains per unit volume the second linear region $(1 < \left(\lambda - \frac{1}{\lambda^2}\right) < 4)$ was employed.

than in the organically cross-linked hydrogel. This supports the presumption of a particularly high fracture toughness of nanocomposite hydrogels under consideration in this thesis as a proportionality between fracture toughness and the square route of the molecular weight is reported (Lake and Thomas, 1967). The relationship originates in the assumption that energy is stored in each bond between cross-links which is dissipated during crack propagation. Thus, high molecular weight yields a high amount of stored energy. Further it is concluded that many of the clay platelets do not act as active cross-linkers. Instead the functionality is predicted to be high in comparison to the organic cross-linker. The comparably low molecular weight of sample OR9 is in good accordance with its brittle and fragile appearance. In contrast the high value for NC9 is in agreement with its flexible appearance. The theoretically calculated molecular weight for sample NC9 differs in more than a magnitude from the molecular weight gained from experiment. In contrast, they are of the same order of magnitude for sample OR9. This implies that the assumption of functionality four applied for the theoretical approach is inadequate for the clay under consideration.

Figure 4.15 a) displays the Mooney-Plot for samples NC7, NC9, NC11 and NC13 which refers to the reduced stress $\sigma^* = \sigma/(\lambda - \frac{1}{\lambda^2})$ as a function of the inverse elongation ratio. The samples do not exhibit a linear Mooney-Plot over the whole displayed range of $\left(0.2 < \frac{1}{\lambda} < 1\right)$. Hence, the material behaviour can not completely be described with the Mooney-Rivlin Theory, especially not at low strains. However, the samples do exhibit rubber elasticity in the range of $\left(0.2 < \frac{1}{\lambda} < 0.7\right)$. The steep increase of the reduced stress at low extensions (and hence high inverse extensions; $\left(0.7 < \frac{1}{\lambda} < 1\right)$) is interpreted as softening of the material (Carlsson et al., 2010). Therefore, at strains corresponding to $\left(0.7 < \frac{1}{\lambda} < 1\right)$ an additional term contributes to the modulus, which cannot be explained by the elasticity of polymer chains or the interaction between polymer chains (Smith, 1967). For filled elastomers a similar increase is reported to be due to polymer-filler interactions. Stress-softening can be a consequence of stress-induced filler cluster breakdown (Meissner and Matějka, 2000). For nanocomposite hydrogels as considered in this study the increase is probably due to a combination of polymer-clay interactions and clay-clay interactions.

Figure 4.15 b) displays the Mooney-Plot for samples NC9 and NC9_THICK. The curves almost overlap each other and no significant discrepancies are perceptible.

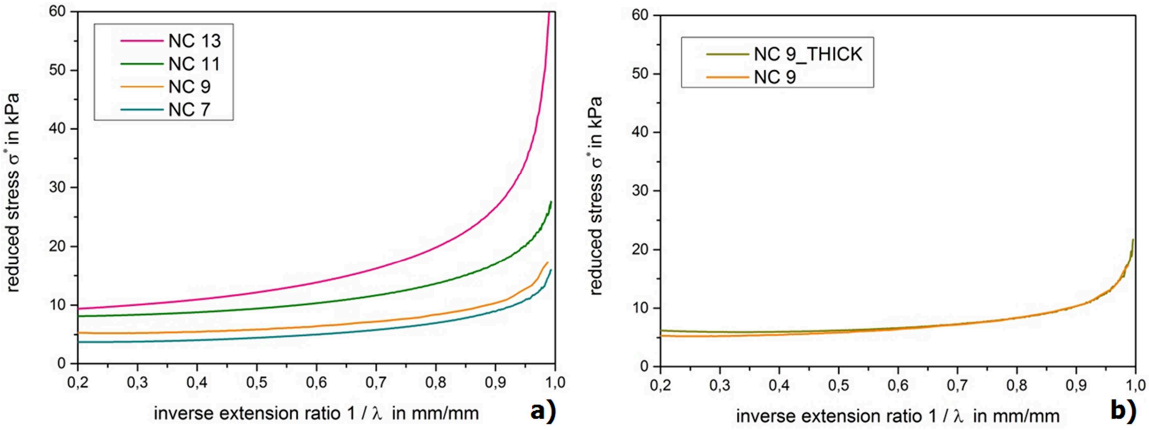

Figure 4.15: Mooney-Plot **a)** for samples NC7, NC9, NC11, NC13 **b)** for samples NC9, NC9_THICK.

A different approach to evaluate data according to the Mooney-Rivlin Theory is to plot the reduced stress $\sigma^* = \sigma/(\lambda - \frac{1}{\lambda^2})$ as a function of the extension ratio. For nanocomposite hydrogel samples considered in this thesis hyperbola of the form given in Eq. 4.1 can be fitted.

$$\sigma^*(\lambda) = A + \frac{B}{\lambda - C} \tag{4.1}$$

Fitting is performed for each specimen, which yields parameters A, B and C. The major aim of fitting hyperbolas to the data is to create comparable parameters. Hence, A, B and C are averaged for each sample and listed in Table 4.3.

Table 4.3: Fitting parameters A, B, C for Mooney-Rivlin Theory according to Eq. 4.1.

Sample	**A**	**B**	**C**
-	**kPa**	**kPa**	**mm/mm**
NC7	3.4	1.2	0.8960
NC9	5.0	0.9	0.8447
NC11	7.6	2.1	0.8888
NC13	8.9	3.4	0.9048
NC9_THICK	5.9	0.6	0.9610

The resulting hyperbolas are displayed in Figure 4.16 a) for samples NC7, NC9, NC11 and NC13 and in b) for samples NC9 and NC9_THICK.

The interpretation of the curves is equal to the discussion brought forward for the original Mooney-Plot. The linear plateau reached at an extension ratio of about 2 mm/mm is even more apparent than in the original Mooney-Plots. Deviations from linearity at small extension ratios are particularly obvious.

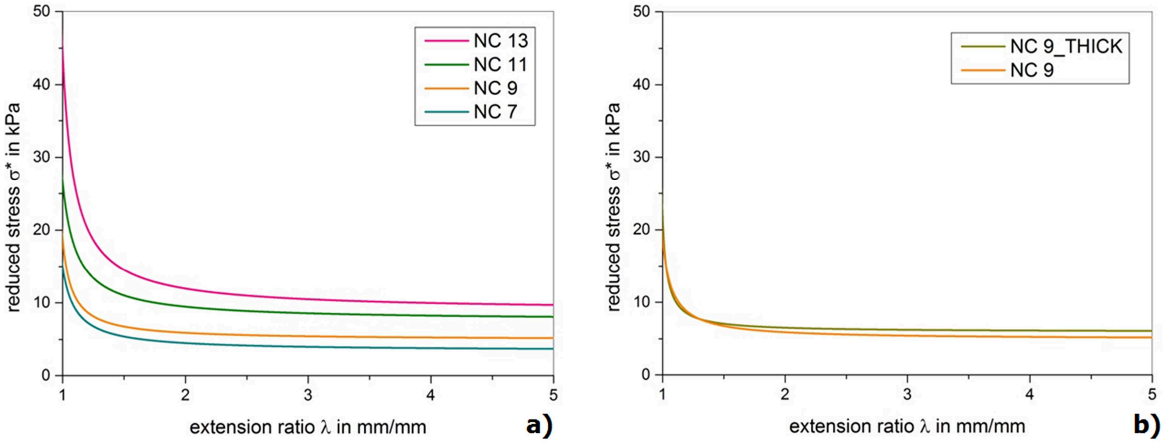

Figure 4.16: Fitted hyperbolas for Mooney-Rivlin Theory according to Eq. 4.1 **a)** for samples NC7, NC9, NC11, NC13 **b)** for samples NC9, NC9_THICK.

Parameter A increases with increasing clay content. Both parameters B and C do not exhibit a dependency on the clay content. It is thus concluded that the curves only deviate in terms of the (reduced) stress level while the shape of the curve is equal for each sample. The influence of sample thickness is discussed using samples NC9 and NC9_THICK. All parameters A, B and C are probably independent of sample thickness as they are similar for samples NC9 and NC9_THICK.

It is concluded that while the material behaviour of organically cross-linked hydrogels can readily be described with Simple Rubber Elasticity Theory, none of the applied theories ideally describes the material behaviour of nanocomposite hydrogels considered within this study. This might be due to the structure of the inorganic/organic-network and the complicated interactions between clay and polymer as described above.

4.3.2 Fracture Toughness

In order to determine fracture toughness parameters trouser-leg tear tests as well as pure shear tests are conducted. As the trouser leg tear test could not yield fracture of the samples, the test is discontinued and no evaluation is conducted. The reason for the incapability of yielding fracture in this test is the tensile testing machine’s limitation of crosshead travel. The crack does not propagate even though the legs of the test specimens are stretched until the top of the crosshead travel is reached. Instead the crack completely blunts. Additionally, standards regulate that the trouser tear test is invalid if substantial extension in the trouser legs can be observed (Greensmith and Thomas, 1955). As large deformation is present for the samples under consideration, no valid results could be obtained even when employing a larger tensile testing machine. In consequence the trouser leg tear test is evaluated as inappropriate testing method for the characterization of fracture toughness for samples considered within this thesis. Thus focus is on pure shear test in order to gain comprehensive information on fracture toughness of nanocomposite hydrogels.

In the following paragraphs initially the development process of sufficient sample preparation for pure shear tests will be discussed. Since the pure shear test requires a high ratio of initial sample width to initial sample length, the dimensions are defined as 5 mm of length and 70 mm of width. Thus this specimen type does not exhibit shoulders such as the dumbbell specimen type. In addition the starting length is very small. Hence, clamping is an inherent problem with this test approach. As to obtain the required specimen dimensions bigger samples of approximately 25 to 30 mm in length and 70 mm in width are cut and then glued on plastic microscopy slides using off-the-shelf super glue with a distance of 5 mm as schematically shown in Figure 4.17. By this means the initial length of 5 mm is assured. In order to guarantee reproducible set-up for all samples a frame is built that holds the microscopy slides while gluing.

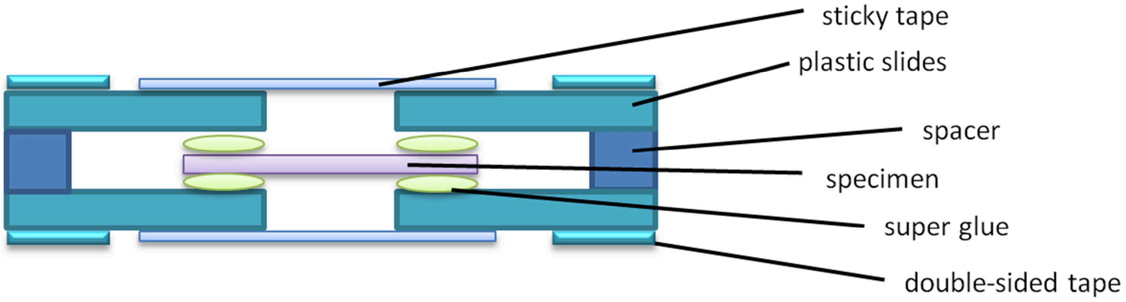

Figure 4.17: Set-up of sample holder including sample for pure shear test.

In order to keep the set-up stable while mounting on the tensile testing machine and prevent the sample from stretching out, sticky tape is added between the microscopy slides. Before starting the test, the sticky tape is clipped. The microscopy slides are found to slip from the grips of the tensile testing machine. Hence, double-sided tape is applied to enhance adhesive forces to the grips. As the sample is squashed when the grips are closed, spacers are inserted between the microscopy slides to keep them at a defined distance. For the notched samples a cut of a length of approximately 45 mm is introduced by employing particularly sharp scissors. Thereafter the notch is sharpened with a razor blade. No particular importance is attached to the exact length of the notch as test and results are independent of the notch length (Sun et al., 2012). The material sticks together immediately after removing scissors or razor blade. To overcome this problem both scissors and razor blade are in advance coated with silicone oil.

No sufficient adhesion between sample and microscopy slides can be achieved with this approach. Material is pulled out between the slides before fracture occurs. Instead of fracture of the sample, failure occurs at either the sample-glue interface or the glue-slide interface. To overcome this problem plastic microscopy slides are replaced by glass slides. However they split in the test grips. Additionally, several different brands and types of super-glue are tested, including low viscosity as well as high viscosity glues and such glues that obtain their adherence after more than a day as well as glues that exhibit instant adherence. However, the type of glue significantly affects load-extension curves. No proper results can be obtained following this approach. An exemplary load-extension curve (sample NC7, unnotched) is displayed in Figure 4.18. The stepwise decreases in force beginning from extensions of about 40 mm in the example given correlate with visual observations of material being pulled out between the grips. Thus the approach reported in literature (Sun et al., 2012) that employs the combination of conventional superglue and plastic microscopy slides is not appropriate for the samples under consideration in this thesis.

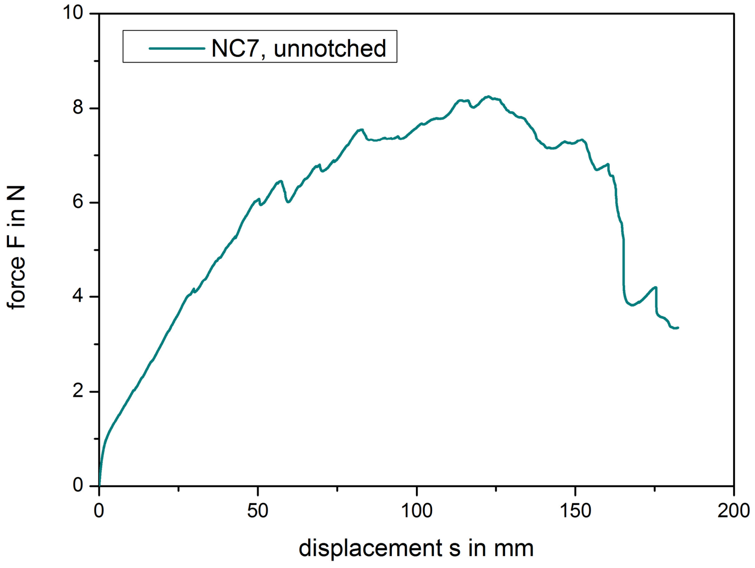

Figure 4.18: Exemplary load-extension curve for material that slips from grips.

In a new design of the sample-holding set-up the plastic microscopy slides are ground with sandpaper (coarseness P80) to allow the superglue to better attach to the surface. Hence the improvement is thought to arise from an increase in the surface area between the glue and the sample. This approach as well as gluing the samples directly on sand-paper with different levels of coarseness leads to similar results as depicted in Figure 4.18. Additionally, different types of clamps for the tensile testing machine are tested with the result that the broadest clamps yield the best (most stable) mounting of the slides.

Ultimately, special 3D-printed grips are designed including the testing of prototypes. The final design is defined as illustrated in Figure 4.19. 3D-printing is performed applying a printing system "Objet Eden 260" by ANFF (Australian National Fabrication Facility, Materials Node at University of Wollongong, AUS). The grips consist of a material known by the trade name "FullCure 720". The specimen is laid on one grip (Figure 4.20 a)). Sub-sequently a second mirrored grip is laid on top. The pins (Figure 4.19, left) of the first grip that fit into the holes of the second grip (Figure 4.19, right) are utilized to perfectly align upper and lower grips. Spacers to keep the material from being squashed are present. The spacers that connect the left and the right slide assure their distance of 5 mm and the stability of the composition. They are clipped with sharp scissors directly before testing is started. Figure 4.20 c) shows the mounted sample-holder including a sample during the test without spacers. The surface of the grips consists of alternating small pins and holes (diameter of 1 mm). The pins are utilized to enhance the hold of the material while the holes allow the application of low-viscosity glue from the back of the grips (Figure 4.20 b)). As the grips are particularly designed for samples with a thickness of 2 mm, sample NC9_THICK is not tested regarding fracture toughness. Additionally no fracture toughness testing is conducted on sample OR9. This is due to the fragility of this sample which makes mounting in the designed grips impossible. Attempts to mount sample OR9 are followed by crumbling of the sample.

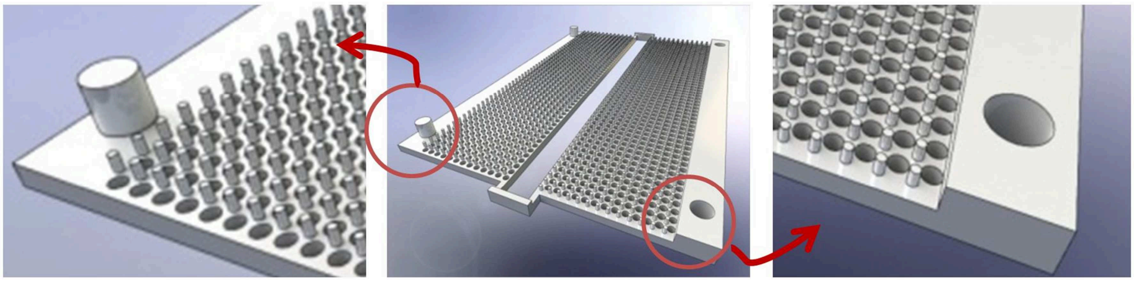

Figure 4.19: 3D-printed grips to hold samples for pure shear test.

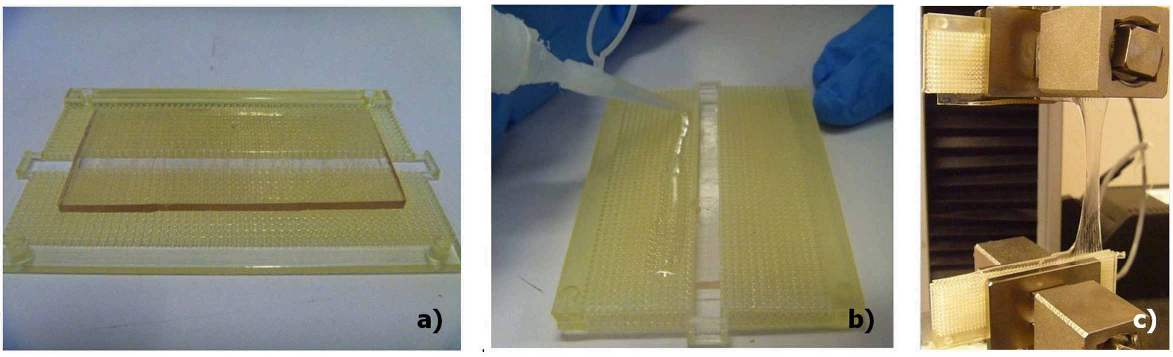

Figure 4.20: a) mounting and **b)** gluing of specimen in 3D-grips; **c)** grips in tensile testing clamps.

Results presented in the following are obtained from testing of notched and unnotched samples. Unnotched samples are tested up to extensions equal to extension-at-break of corresponding notched samples. Extensions-at-break for notched samples are given in Table 4.4. Representative force-displacement curves for samples NC7, NC9, NC11 and NC13 are displayed in Figure 4.22. The large strains prior to fracture shall be emphasised as the diagrams only depict extensions. The notched samples exhibit a strain-at-break between 1450 % and 2500 %. Further, it is worth noting that observations during experiments reveal that blunting of the cracks starts immediately. The large difference in force between notched and unnotched samples as displayed in Figure 4.22 is due to the reduced width of the notched samples. This is due to the relationship between stress and force with the inverse cross-section acting as correlation parameter. Nanocomposite hydrogel samples are insusceptible to flaws and the notches do not yield a stress concentration. Hence, both notched and unnotched samples exhibit similar stresses at the same strain level. As the notched samples exhibit a smaller width in comparison to unnotched samples, the force is correspondingly lower for notched samples.

Evaluation regarding fracture toughness yields the parameter G_c as described in subchapter 2.2.4.4 and subchapter 3.3.2. G_c as a material parameter has to be independent of sample geometry. As all fracture toughness tests has been performed using the same type of sample, no final proof can be given. However, the initial notch length is believed not to influence test results. Hence, notches were introduced without special focus on their length. Figure 4.21 displays force-displacement curves for sample NC13 with different initial notch length. It is apparent, that a longer notch does not lead to a smaller displacement. Instead differences in the curves probably arise from the error in measurement. In addition, Sun et al. (2012) reports for a certain type of hydrogel that pure shear test, double-peeling test and the so called 'tensile test with multiple samples containing notches of various lengths' reveal the same fracture toughness. This supports the assumption that the pure shear test as performed in this thesis allows an estimation of G_c as material constant.

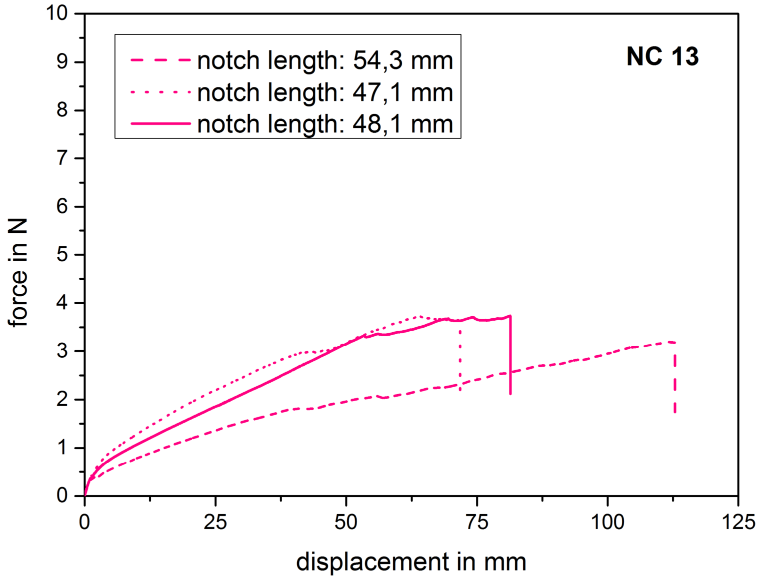

Figure 4.21: Correlation between initial notch length and displacement.

Evaluation yields a fracture toughness G_c of 2400±16 J/m^2 for sample NC7, 4300±241 J/m^2 for sample NC9, 6600±390 J/m^2 for sample NC11 and 6800±312 J/m^2 for sample NC13. Averages are rounded to hundreds to compensate for observed scattering in the curves. Increasing clay content leads to higher fracture toughness. This is in agreement with expectations arisen from low strain measurements. However, the strongest increase in fracture toughness is observable for clay contents up to 11 mole% per L water. Further increase in clay concentration to 13 mole% per L water yields marginal changes in fracture toughness. Hence, it is assumed that a further increase in clay content would not result in significantly higher fracture toughness than observed for sample NC13. Figure 4.23 displays the dependency of fracture toughness on clay content. The diagram includes the standard deviations of the average.

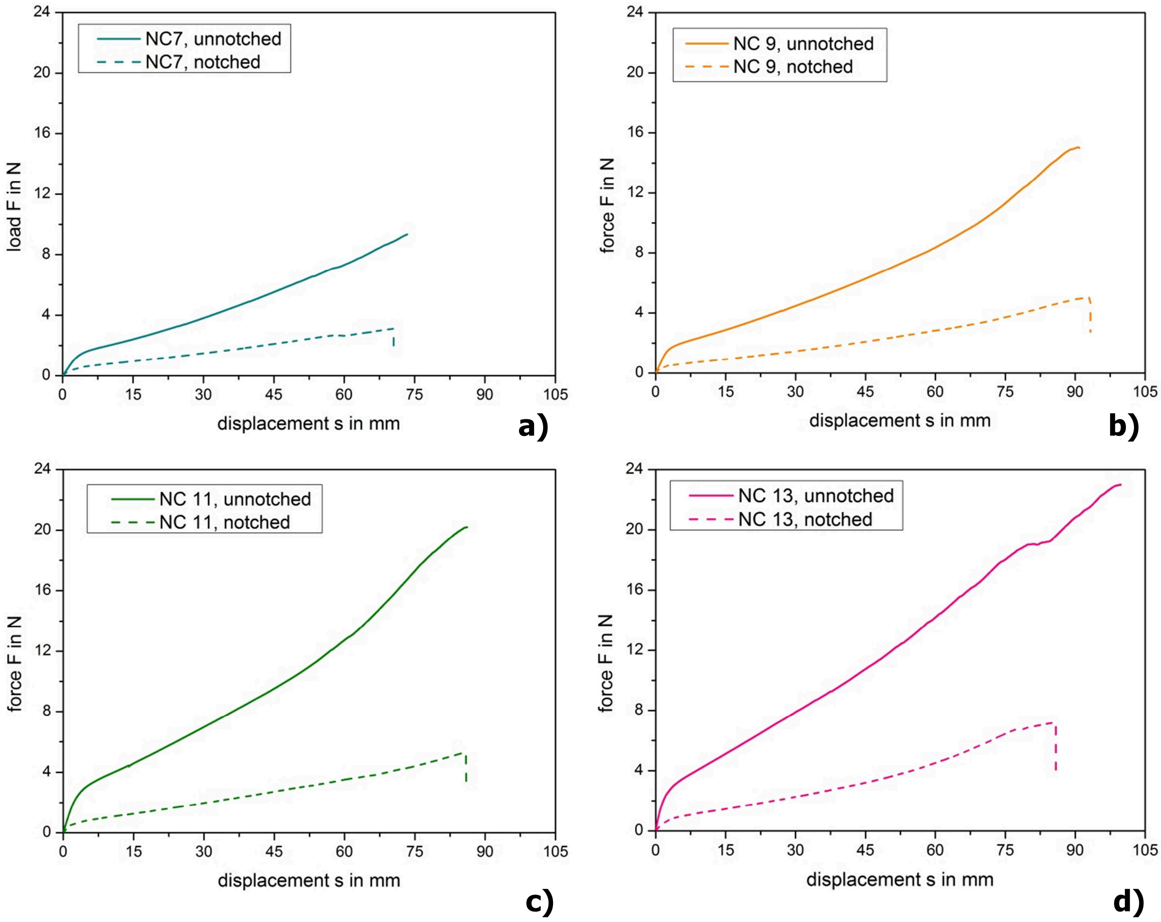

Figure 4.22: Force-displacement curves (full lines: notched specimen; dashed lines: unnotched specimen) for samples **a)** NC7, **b)** NC9, **c)** NC11, **d)** NC13.

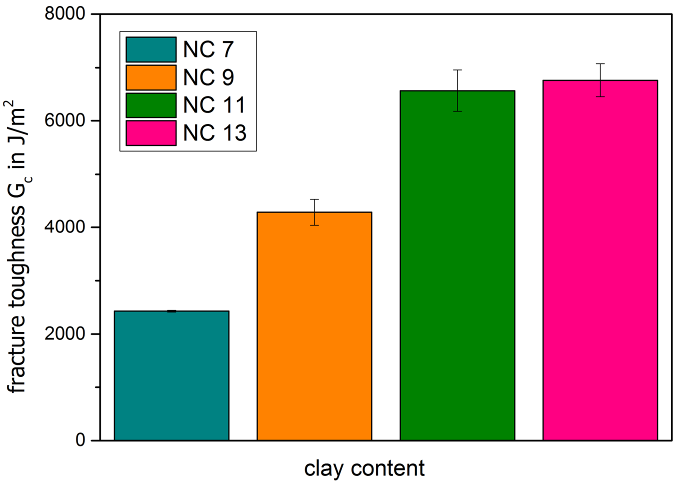

Figure 4.23: Fracture toughness as a function of clay content for samples NC7, NC9, NC11, NC13.

A comparison with reported fracture toughnesses for other types of gels reveals that fracture toughness of nanocomposite hydrogel samples considered in this thesis are extraordinarily high. Tanaka et al. (2005) have stated fracture energies between 100 and 1000 J/m^2 for PAMPS-PAAm[2] double-network hydrogels. Seitz et al. (2009) have reported fracture energies between 10 and 100 J/m^2 for acrylic triblock gels[3]. Sun et al. (2012) have reported to have synthesized an extraordinary tough gel consisting of both ionically cross-linked alginate and covalently cross-linked polyacrylamide. The stated fracture toughness values with a maximum of 8700 J/m^2 is comparable with the results for samples under consideration in this thesis. Probably the high fracture toughness of nanocomposite hydrogels is due to long chains between the cross-linking clay and the multifunctionality of this particular kind of cross-linker. If one polymer chain of one bond between polymer and clay is broken, nanocomposite hydrogels are capable of transferring its load to many other chains as a consequence of multifunctionality (Seitz et al., 2009). Hence, formation of microcracks and voids as typically occurring in organically cross-linked hydrogels is oppressed (Huang et al., 2007).

Table 4.4: Extension-at-break and fracture toughness for samples NC7, NC9, NC11, NC13.

Sample	Extension-at-Break	Fracture Toughness
-	mm	J/m^2
NC 7	73	2400
NC 9	93	4300
NC 11	86	6600
NC 13	89	6800

As nanocomposite hydrogel samples are capable of quickly dissipating large amounts of energy, their viscoelastic properties shall be studied and discussed in the following chapter.

4.4 Characterization of Viscoelastic Properties

This chapter aims to characterize and discuss viscoelastic properties of the nanocomposite and organically cross-linked hydrogels considered in this thesis. Results of step cycle

---

[2] PAMPS is short for poly(2-acrylamido-2-methylpropanesulfonic-acid), PAAm is short for poly(acrylamide)

[3] Triblock gels consist of poly(methylmethacrylate) endblocks and a poly(n-butylacrylate) midblock

testing, stress relaxation experiments, DMA and rheometry will be discussed. Step cycle testing as well as stress relaxation experiments cannot be performed on sample OR9. This is due to the brittleness of sample OR9 which causes the sample to fracture at strains of approximately 10 % as discussed in subchapter 4.3.1. As both step cycle tests and stress relaxation experiments require the application of high strains up to 400 % for the former and 100 % for the latter, they are not applicable for sample OR9.

4.4.1 Step Cycle Testing

Step cycle testing is performed to study and discuss material behaviour during cycling loading and unloading. The behaviour is also compared to a monotone loading and unloading which is from now on referred to as 'single step testing'. Further, step cycle testing allows the splitting of total strain into elastic and plastic fractions.

Figure 4.24 compares a representative curve gained from step cycle testing to one gained from single step testing exemplarily using sample NC11. The points marked with an 'X' represent the peaks of each cycle of the step cycle test. At each peak loading is interrupted by unloading to 0 kPa stress, followed by the next loading. It has to be remarked that both step cycle and single step testing are performed up to a tensile strain of 350 % measured for the length between the clamps. However, Figure 4.24 shows significantly higher strains. This is because it displays strain recorded with a video extensometer as explained in subchapter 3.3. At strains lower than 150 % single step testing yields slightly lower tensile stresses than step cycle testing. However, this discrepancy between the two curves is regarded as insignificant. In the strain range from 150 % to about 250 % step cycle and single step testing are in good agreement with one another. At strains higher than 150 % single step testing causes no apparent softening or hardening effect in the material, while step cycle testing results in strain hardening as evident by the above average increase in tensile stress. Hence, cyclic application of load changes stretching properties of the material. The hardening effect is perhaps due to orientation of clay platelets combined with effects from sample geometry and is discussed in more detail in the following paragraphs.

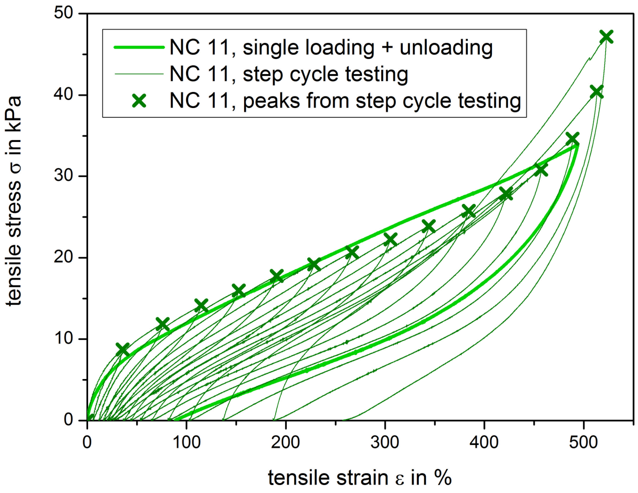

Figure 4.24: Step cycle testing vs. single load testing for sample NC11.

Curves obtained from step cycle testing are further analysed regarding the Mullins effect. It is found for strains up to about 450 % that most loading cycles intersect with the previous cycle at marginally lower strains than the peak of the latter. However, as the intersections are very close to the peak this is not interpreted as being a major discrepancy from the Mullins Effect. This is displayed in both Figure 4.24 and Figure 4.26. Additionally the tensile stress of a new loading curve always exhibits a lower level than the tensile stress observed for the previous loading. Hence a good agreement with the Mullins Effect is present for strains to about 450 %. For filled elastomers, this effect is attributed to the debonding of polymer chains from fillers. Hence, for nanocomposite hydrogels the cause is probably a debonding of polymer chains from clay platelets. As debonded chains do not contribute to material's strength, a decrease of tensile stress is observed in each subsequent cycle. The Mullins Effect is not present at strains higher than 450 %.

Figure 4.25 a) to d) show representative true stress-strain curves for samples NC7, NC9, NC11 and NC13 as obtained from step cycle testing. Fifteen loading/unloading cycles are displayed for each sample. In the following paragraphs the terms 'strain' and 'stress' refer to true strain and true stress respectively if not explicitly stated elsewise.

Maximal stresses increase with increasing clay content as previously observed in low strain measurements. Further, for several cycles the stress level of a new loading lies in between that of loading and unloading of the previous cycle and intersects at around its peak. At a certain extent of applied strain the new loading curve instead intersects the previous loading curve already in its loading part. The occurrence is displayed in detail for exemplary sample NC9 in Figure 4.26.

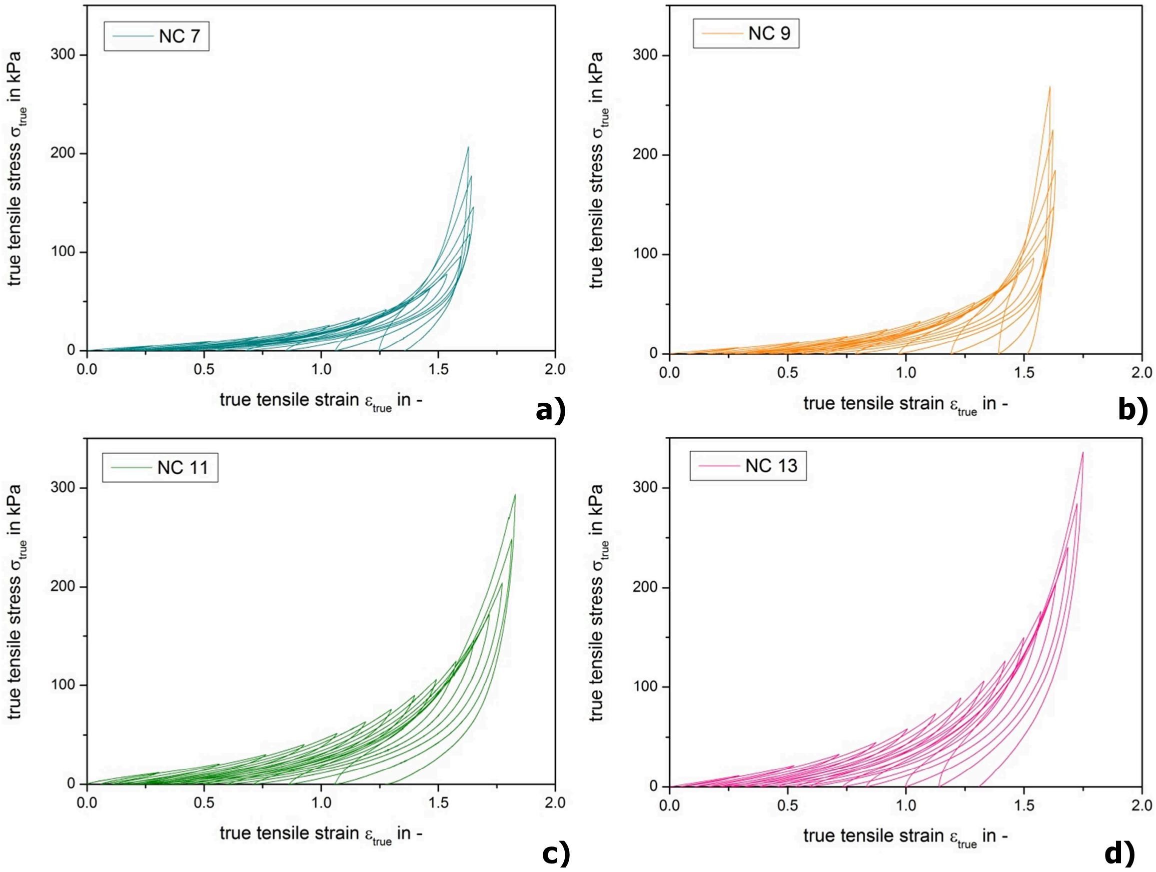

Figure 4.25: True stress-strain curves from step cycle test for samples **a)** NC7, **b)** NC9, **c)** NC11, **d)** NC13.

The number of cycles before this phenomenon occurs is increasing with increasing clay content. However, it occurs at about the 11th cycle which corresponds to about 300 % of engineering tensile strain. Figure 4.26 shows that the loading-curve of cycle 10 intersects with cycle 9 at its peak while the loading-curve of cycle 11 intersects cycle 10 already at the loading-curve of cycle 10.

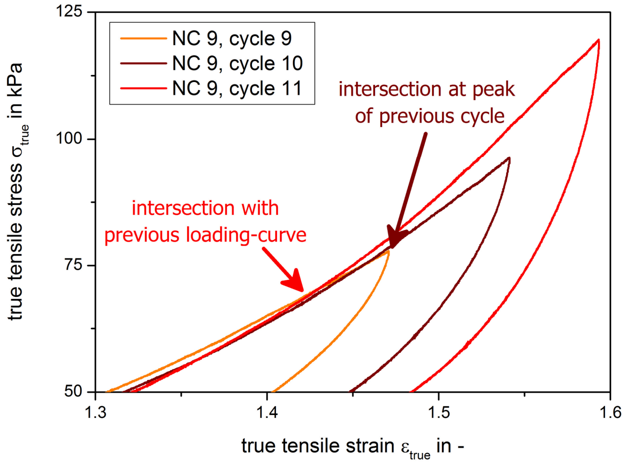

Figure 4.26: Detail of step cycle curve for sample NC9.

Further, the recorded total strain slightly decreases at high applied strains in contrast to the increasing of engineering strain by 25 % for each cycle. The effect is not detectable if crosshead strain is used for evaluation instead of the strain recorded with the video extensometer ('video strain'). Two different effects that might lead to this occurrence shall be outlined in the following paragraph.

The first effect probably causing the decay of the total true strain is (strain) hardening. The tensile testing machine is programmed to move strain-controlled. It is monitored that the tensile strain between the clamps is correctly increased by 25 % at each cycle. This leads to a corresponding tensile stress which – as a consequence – increases at each cycle, too. Tensile stress and video strain are correlated by a parameter. At very low strains the correlation parameter is the Young's Modulus. At any higher strains the Young's Modulus is replaced by a different type of modulus. It is believed that once hardening occurs, the correlation between tensile stress and strain changes significantly, which means that the modulus rises by a notable degree. Hence an increase in tensile stress as provoked by the crosshead strain does not necessarily lead to an equal increase in video strain. Instead it can even be followed by a decay of strain as shown in Figure 4.27. Hardening in nanocomposite hydrogels is probably due to orientation of clay particles. One approach to confirm this assumption would be the employment of wide-angle X-ray diffractometry.

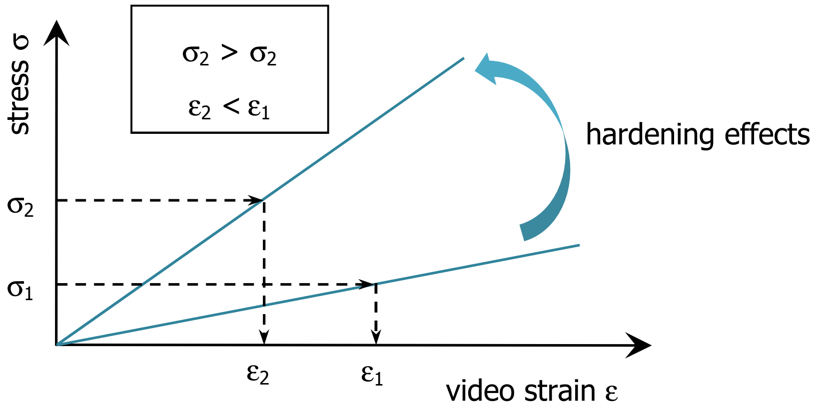

Figure 4.27: Illustration of a possible effect of (strain) hardening.

The second effect that might contribute to the decrease of the total strain at high strains is the sample geometry. While testing the specimens there is substantial deformation in the shoulders of the specimens as depicted in Figure 4.28. Thus additional material contributes to the strain that is recorded for the crosshead strain. In contrast the video extensometer only records strain in the thin part of the dumbbell specimen between the red marks in Figure 4.28.

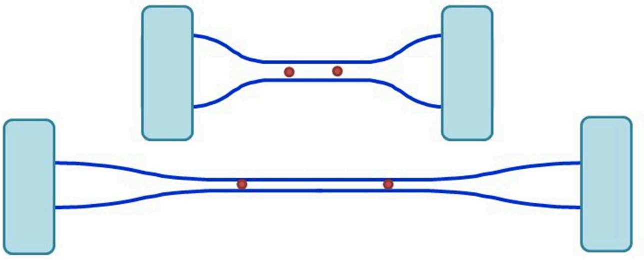

Figure 4.28: Illustration of deformation of dumbbell specimen while stretching.

It is assumed that it is necessary that both effects, deformation outside of gauge length as well as strain hardening, have to be present to yield the phenomenon as discussed above.

Figure 4.29 shows the splitting of the strain into elastic and plastic parts as percentage of the total strain and in each case as a function of the total strain. Both elastic and plastic strain exhibit a plateau up to a total strain of about 1.2 to 1.5. Thus, the ratio between elastic and plastic strain is nearly constant in this strain range. The total strain consists of an elastic fraction of approximately 75 % to 85 % and a plastic fraction of approximately 15 % to 25 %. This phase is followed by a steep – almost vertical – decrease in the elastic fraction, naturally accompanied by an as steep increase in the plastic fraction. Hence, at a certain degree of applied strain, the plastic strain fully dominates and increases to almost 100 % due to cyclic loading. This is supported by the visual observations: After applying low to moderate strains the material can recover most of its original shape while the application of very high strains leads to permanently deformed samples. Hence, it is expected that plastic deformation occurs throughout the whole sample. In the presence of a crack, plastic deformation is probably large in the proximity of the crack tip. Thus, a significant amount of energy is presumably dissipated by plastic deformation. An interesting observation is that the total (true) strain slightly diminishes at very high engineering strains. This is displayed in Figure 4.29 a) and b) at total true strains of about 1.5 as backwards slope in the curves. The finding equals the phenomenon described above that at a certain degree of strain a new loading curve intersects the previous cycle in its loading curve (in contrast to lower strains where it intersects at the peak or the unloading section).

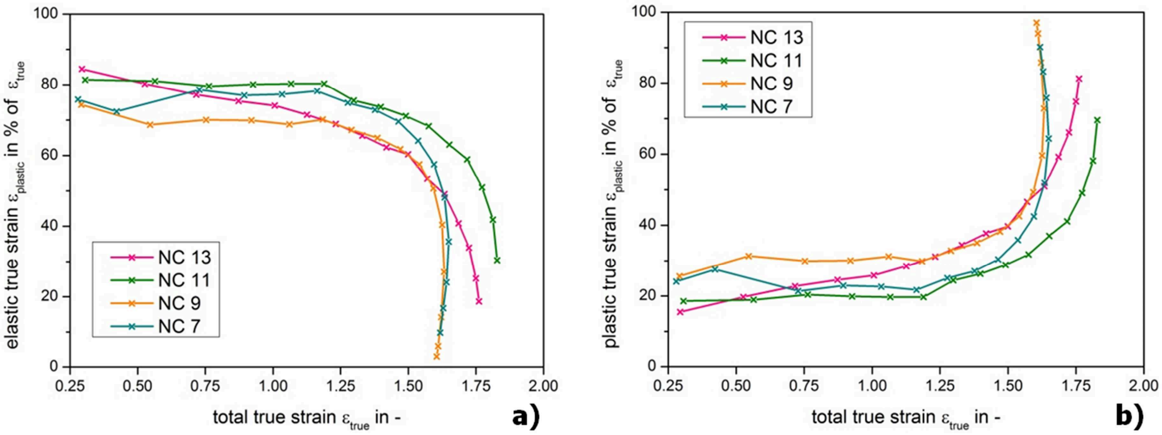

Figure 4.29: a) Elastic true strain and **b)** Plastic true strain as a function of total true strain for samples NC7, NC9, NC11, NC13.

As to show effects of sample thickness on material behaviour in cyclic loading, Figure 4.30 compares a) elastic and b) plastic strain as a function of total strain for samples NC9 and NC9_THICK. No effect of sample thickness on the general shape of the curve is discernible. The elastic fraction of sample NC9_THICK is approximately 15 % higher than for sample NC9. Thus it is concluded that the dissipation of energy is less pronounced for nanocomposite hydrogels with a larger thickness. In addition, the strong increase in plastic strain (displayed Figure 4.30 b) as almost vertical curves) is present at a total strain of approximately 1.6 and 1.8 for samples NC9 and NC9_THICK, respectively. The higher value for sample NC9_THICK means that plastic strain takes the major fraction of total strain at higher strains than sample NC9.

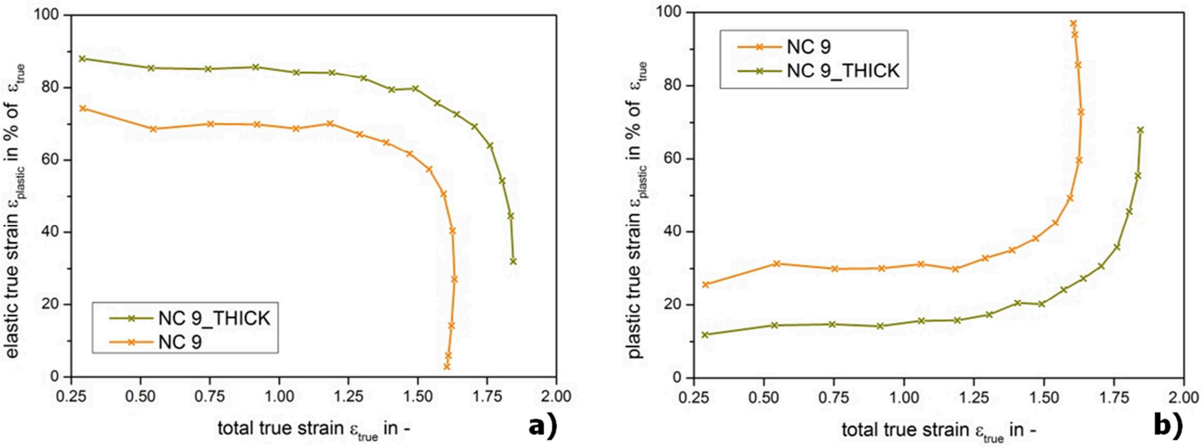

Figure 4.30: a) Elastic strain and **b)** Plastic strain as a function of total strain for samples NC9, NC9_THICK.

4.4.2 Stress Relaxation

Figure 4.31 a) displays the stress relaxation curves for samples NC7, NC9, NC11 and NC13 following stretching to 100 % strain. The stress reaches a plateau as known for cross-linked polymers in contrast to thermoplastic polymers for which stress at infinite time reaches zero stress. The relaxation effect is due to the special molecular structure of polymers. The chains cannot follow the instant deformation simultaneously. Instead they need time for rotation and unwinding to adopt a position allowing for a lower stress-level in the strained state. For cross-linked polymers the entanglements and primary bonds are dominant in defining relaxation characteristics (Brinson and Brinson, 2008). Figure 4.31 a) shows that initial and therefore maximal stress increases with increasing clay content (depicted in Figure 4.33 a)). This correlates with results from low strain measurements as well as from step cycle testing. Sample NC13 and sample NC11 exhibit initial Relaxation Moduli of 26.7 kPa and 22.1 kPa, respectively, while sample NC9 and sample NC7 show initial Relaxation Moduli of 12.4 kPa and 8.4 kPa, respectively. Analogously it is observed that the long-term stress level is increasing with increasing clay content.

Figure 4.31 b) displays the influence of sample thickness on stress relaxation using the example of samples NC9 and NC9_THICK. Sample NC9_THICK exhibits a higher stress level than sample NC9 throughout the whole experiment. This is in agreement with results from low strain measurement and step cycle testing, where sample NC9_THICK also exhibited a higher stress level than sample NC9.

The ratio of infinite stress to initial stress is found to range between 0.48 and 0.54 for all samples with a thickness of 2 mm. The ratio between infinite stress and initial stress represents the stress loss. No effect of clay concentration is ascertained. In contrast, the ratio of infinite stress to initial stress for sample NC9_THICK is found to be 0.61. He et al. (2013) associates high stress loss with long and flexible polymer chains. Energy can be dissipated by movement of flexible polymer chains. Hence it is concluded that sample NC9_THICK exhibits longer polymer chains between cross-links than samples with a thickness of 2 mm.

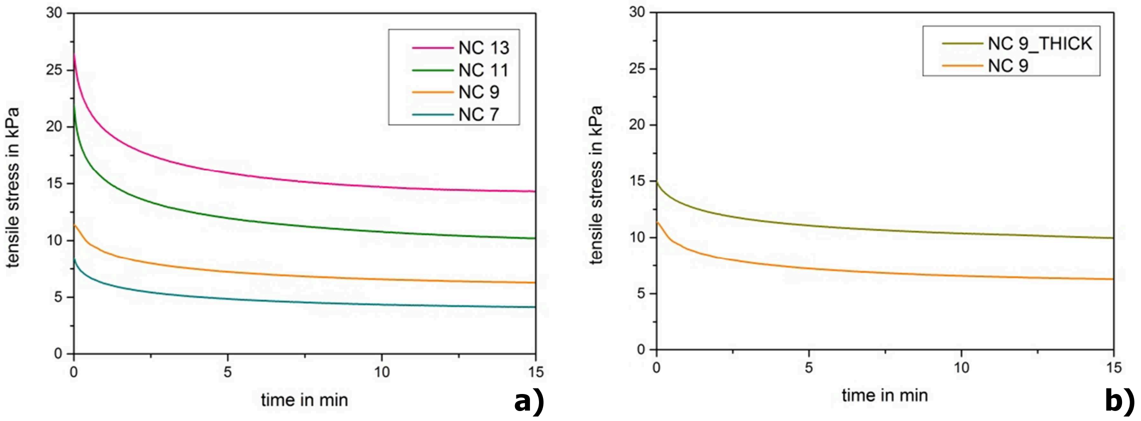

Figure 4.31: Stress relaxation curves **a)** for samples NC7, NC9, NC11, NC13 and **b)** for samples NC9, NC9_THICK.

The fitting of two-element Kelvin models yields two relaxation times, τ_1 and τ_2, as well as Relaxation Moduli E_∞, E_1 and E_2 for samples NC7, NC9, NC11, NC13 and NC9_THICK. The quality of the fits is represented in Figure 4.32. Each fit matches its corresponding curve perfectly. Correlation coefficients of the two-element Kelvin model are typically found at values as high as 0.998 for all tested nanocomposite hydrogels.

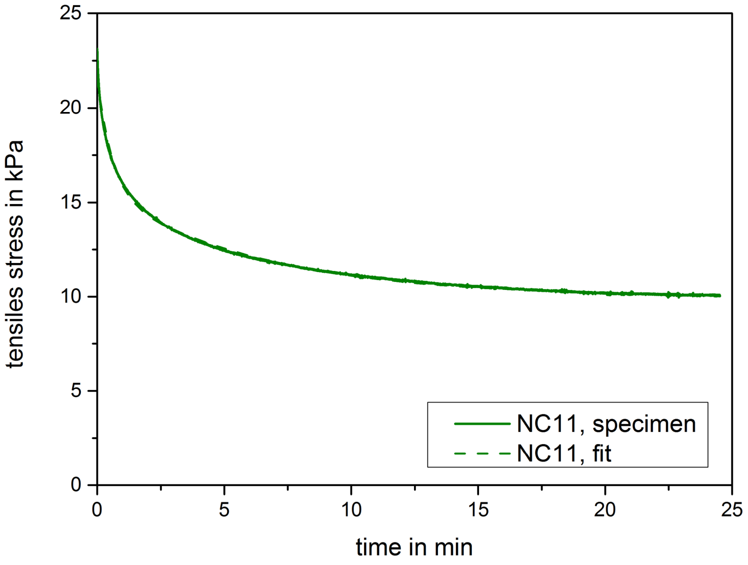

Figure 4.32: Exemplary stress relaxation curve providing evidence for quality of fits.

Averages of the determined parameters including the standard deviations of the average are displayed as bar diagrams in Figure 4.33 a) and b) for relaxation times and Relaxation Moduli, respectively.

The sum of $(E_1 + E_2 + E_\infty)$ represents the stiffness present instantly after applying an external load. After time τ_1 has passed, the stiffness decreases to $(E_2 + E_\infty)$. E_∞ on its own represents the long-term (infinite) Modulus which means that it describes the Modulus after the sample has relaxed. Both Moduli, E_∞ and E_1, increase with increasing clay content. Also E_2 increases with increasing clay content, however, samples NC11 and NC13 exhibit similar values.

The influence of sample thickness on Relaxation Moduli is discussed using the example of samples NC9 and NC9_THICK. The samples exhibit nearly the same values for E_1 and E_2 while E_∞ is significantly higher for sample NC9_THICK. In general the difference between E_1 and E_2 is small compared with the value of E_∞ for all nanocomposite hydrogel samples. Both τ_1 and τ_2 are independent of clay content. Thus all relaxation times for samples NC7, NC9, NC11 and NC13 are averaged. The resulting τ_1 is 293 s with a standard deviation of the average of 14 s. The resulting τ_2 is 30 s with a standard deviation of the average of 1 s. In contrast the relaxation times for sample NC9_THICK are much higher. Relaxation time τ_1 is 734 s with a standard deviation of the average of 199 s while τ_2 is 69 s with a standard deviation of 12 s. Hence, the sample preparation of the thicker material might yield slightly longer polymer chains between the cross-links. The dependency of relaxation behaviour on molecular weight is described in literature. Natural rubber that shows a distinct increase in relaxation time with increasing molecular weight serves as an example (Gao et al., 2011). Most probably the extent of τ_2 is unreliable. This is because the time required to apply the initial strain is larger than τ_2. From stress relaxation experiments it is concluded that viscoelastic dissipation occurs for nanocomposite hydrogel samples as considered here, with a maximum dissipation occurring at a time of about 290 s. Presumably this might correspond to a peak in the loss factor at 0.003 Hz (1/290 Hz). It is further concluded that the cross-links are fixed over long time periods as relaxation takes places.

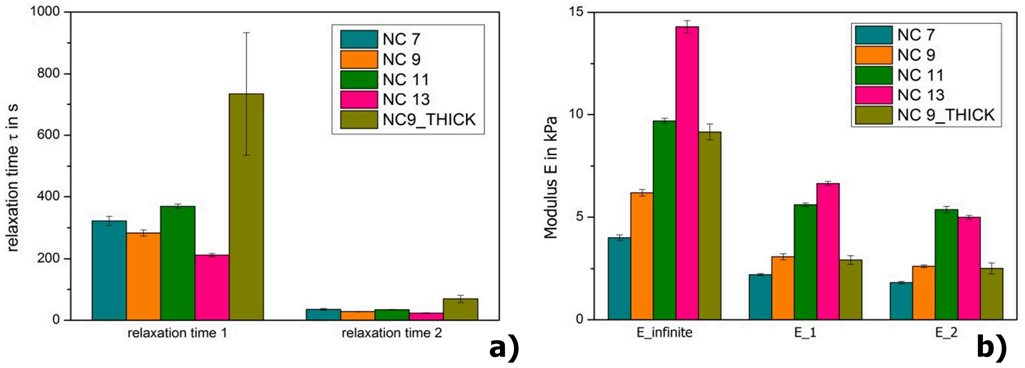

Figure 4.33: a) Comparison of relaxation times 1 and relaxation times 2. **b)** Comparison of modulus E_∞, E_1 and E_2 for samples NC7, NC9, NC11, NC13, NC9_THICK.

4.4.3 Dynamic Mechanic Analysis

Figure 4.34 to Figure 4.36 display the effects of clay content, sample thickness and cross-linker type with regard to the dynamic-mechanical properties. The signals are instable above approximately 50 Hz. Therefore any features of the graphs at higher frequencies as this are discussed further.

Figure 4.34 a) shows the Storage Modulus as a function of frequency for samples NC7, NC9, NC11 and NC13 to study effects of clay content on dynamic mechanic properties. The Modulus increases with increasing frequency as well as with increasing clay content. At 1 Hz the Storage Modulus is 3.6 kPa and 4.8 kPa for samples NC7 and NC9, respectively and 6.5 kPa and 7.8 kPa for samples NC11 and NC13, respectively. This dependence of the Storage Modulus on clay content is an indication for the strong bonds between polymer chains and clay particles resulting in effective (physical) cross-links. The results for the Storage Modulus are in good agreement with results reported in (Haraguchi, 2007) for a similar nanocomposite hydrogel (same monomer, similar type of clay and similar clay content).

Figure 4.34 b) compares the loss factor as a function of frequency for samples NC7, NC9, NC11 and NC13. For all samples the loss factor lies between 0.17 and 0.05 which are comparably small values. Hence the samples are essentially elastic. Further, the loss factor decreases with increasing frequency with a tendency to reach a plateau at higher frequencies. However, as the signal gets instable at frequencies higher than about 50 Hz as stated above, no further statements can be made. For low frequencies up to approximately 1 Hz, the dependency of the loss factor on the clay content is almost insignificant, whereas for higher frequencies the loss factor increases with decreasing clay content. At 1 Hz the loss factor ranges between 0.078 for sample NC13 and 0.097 for sample NC7. As the loss factor can be considered as degree for a material’s toughness, this result indicates that the fracture toughness of the nanocomposite hydrogels in consideration is only slightly dependent on their clay content. A high loss factor indicates a high ability to absorb energy, particularly in cyclic loading. Hence, samples with high clay content are expected to exhibit marginally lower fracture energies than with lower clay content. However, as the differences between the values for the loss factor are minor and the scattering is high, no final prediction can be made. Additionally, this assumption contradicts expectations from low strain measurements. In contrast to DMA results, fracture toughness tests show that fracture toughness increases with increasing clay content.

Concisely, DMA measurements reveal that firstly high clay content yields a higher Modulus which is consistent with the greater number of cross-links. Secondly high clay content is followed by a lower dissipation of energy at high frequencies. This is in agreement with the assumption that a high cross-linking density results in a more elastic system (i.e. lower loss factor).

Different than what is expected from stress relaxation experiments, no peak at around 0.003 Hz can be observed. Possibly the peak is present at lower frequencies than 0.001 Hz which are not in included in the measurement interval. The plateau that can be observed in Figure 4.34 b) for sample NC13 could be interpreted as representative for a peak as the number of measurement points is small in this region.

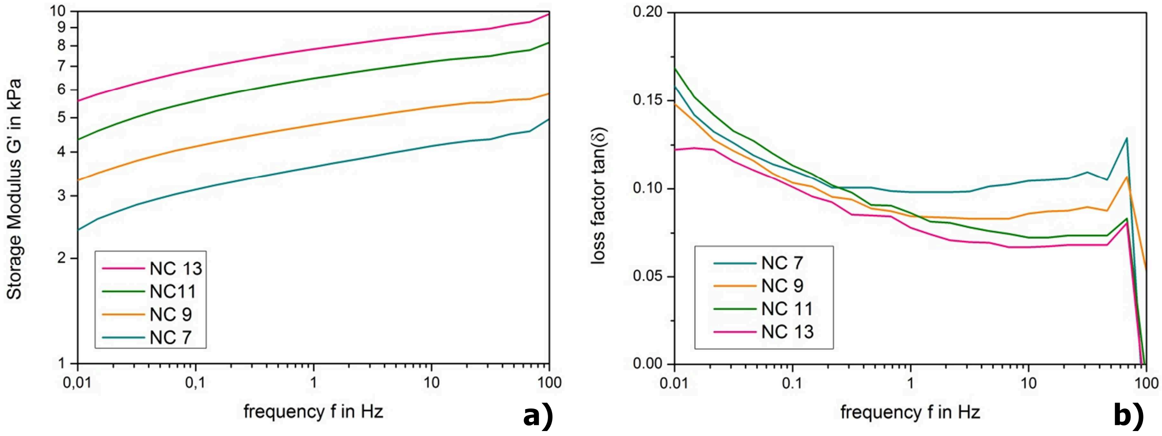

Figure 4.34: a) Storage Modulus and **b)** loss factor as a function of frequency for samples NC7, NC9, NC11, NC13.

Effects of sample thickness on dynamic mechanic properties are studied using samples NC9 and NC9_THICK. Figure 4.35 a) compares the Storage Modulus as a function of frequency for samples NC9 and NC9_THICK. Sample NC9_THICK exhibits a considerably higher Modulus than sample NC9 while the trend of the curve throughout the whole frequency range is in accordance with that of sample NC9. This result corresponds to results gained from low strain tensile testing and stress relaxation. Therefore, sample NC9_THICK probably exhibits a higher molecular weight than sample NC9. However, it has to be remarked that testing is performed employing shear sandwich clamps. As different clamps according to the sample thickness (distance of 1 mm and 2 mm for samples with a thickness of 2 mm and 3 mm, respectively) have to be utilized, the clamping pressure is possibly not equal for all tested samples. The thick samples are squashed to a higher strain to fit in the clamps which might significantly contribute to a higher Storage Modulus. The shear sandwich has a large surface area to thickness ratio which aggravates the effect of squashing. The Storage Modulus at 1 Hz is 4.8 kPa and 7.0 kPa for samples NC9 and NC9_THICK, respectively. Figure 4.35 b) compares the loss factor as a function of frequency for samples NC9 and NC9_THICK. For low frequencies between 0.01 Hz and 3 Hz the level of the loss factor is to a small degree higher for sample NC9_THICK than for sample NC9. Then the curves intersect and the loss factor is marginally higher for sample NC9 at frequencies higher than 3 Hz.

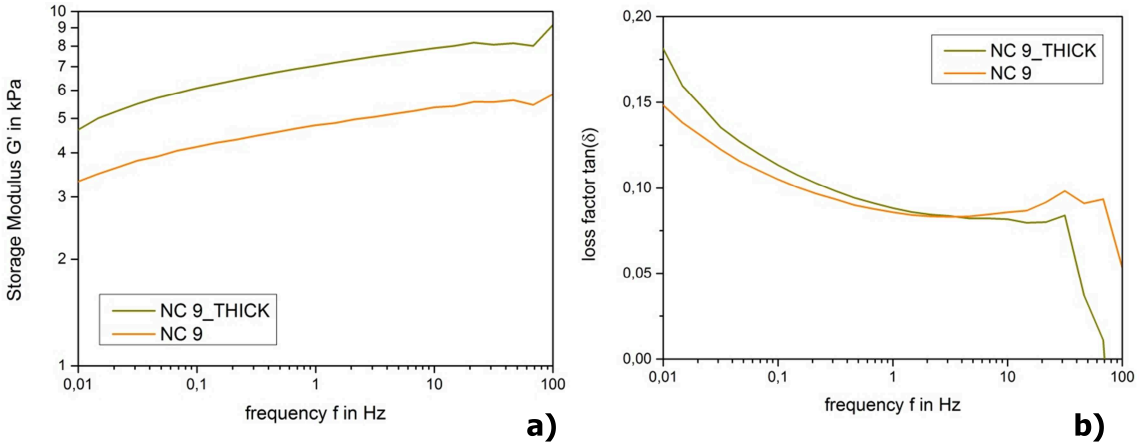

Figure 4.35: a) Storage Modulus and **b)** loss factor as a function of frequency for samples NC9, NC9_THICK.

Effects of cross-linker type on dynamic mechanic properties are studied using samples NC9 and OR9. Figure 4.36 a) compares the Storage Modulus as a function of frequency for samples NC9 and sample OR9. The Storage Modulus for sample OR9 is more than half a magnitude higher than that of sample NC9 throughout the whole frequency range. At 1 Hz, sample NC9 exhibits a Storage Modulus of 4.8 kPa while sample OR9 exhibits a Storage Modulus of 20.4 kPa. In contrast to nanocomposite hydrogels, sample OR9 does not show an increase in Storage Modulus with increasing frequency. This result is consistent with literature as hydrogels are assumed to be elastic and thus exhibit no dependency of their Modulus on frequency. Figure 4.36 b) compares the loss factor as a function of frequency for samples NC9 and OR9. The samples show converse trends in their curve progression. While the loss factor of sample NC9 decreases with increasing frequency between 0.01 Hz and approximately 1 Hz, the loss factor of sample OR9 exhibits a plateau in this frequency range. This section is followed by a plateau for sample NC9 while the loss factor of sample OR9 advances considerably. Up to high frequencies sample NC9 exhibits a significantly higher level in its loss factor compared to sample OR9. At 0.01 Hz the loss factor is found to be 0.148 for sample NC9 and 0.018 for sample OR9. At 1 Hz the difference is smaller with 0.084 for sample NC9 and 0.018 for sample OR9. Since the loss factor represents the ratio between Loss Modulus and the Storage Modulus, values below unity throughout the whole frequency range implies that the Loss Modulus never exceeds the Storage Modulus. This means that elastic properties dominate over viscous properties and a gel- or solid-like character is present. As discussed above the loss factor is an indication for samples toughness. It is thus concluded that sample OR9 exhibits a remarkably lower (fracture) toughness than nanocomposite hydrogel samples as considered in this thesis. This is conform to results from low strain measurements. As no fracture toughness could be performed on sample OR9, no final verification of this assumption can be made. However, the cause for the incapability to perform fracture toughness tests on sample OR9 is their brittleness which is in agreement with the presumption of their low fracture toughness.

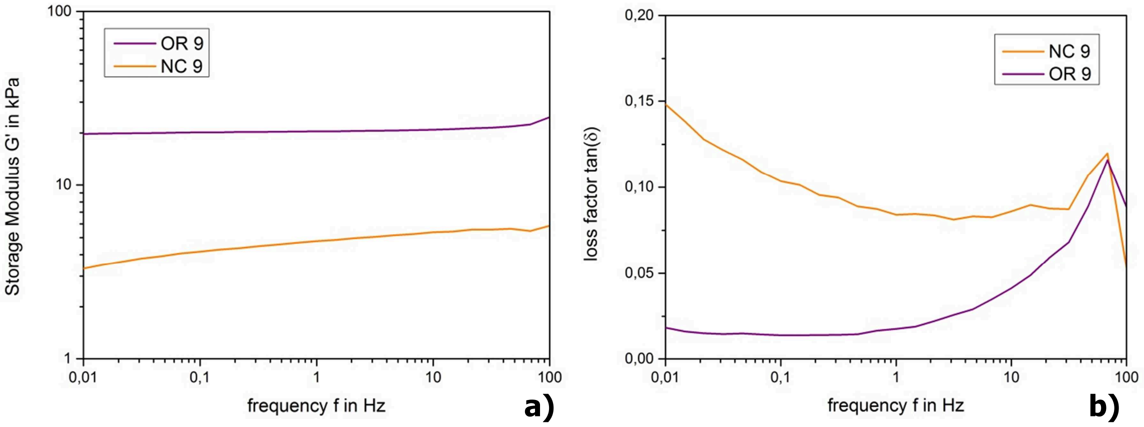

Figure 4.36: a) Storage Modulus and **b)** loss factor as a function of frequency for samples NC9, OR9.

4.4.4 Rheometry

In the following subchapters results gained from rheometry experiments are discussed. Firstly, viscoelastic properties are considered and compared to results gained from DMA. Secondly, the Payne Effect is studied in order to compare material behaviour of nanocomposite and organically cross-linked hydrogels to filled elastomers.

4.4.4.1 Determination of Viscoelastic Properties

Figure 4.37 to Figure 4.39 display the effects of clay content, sample thickness and cross-linker type with regard to the dynamic mechanical properties as tested in a rheometer. Although measurements are performed in a frequency range from 0.01 Hz to 100 Hz, frequencies are only displayed up to 10 Hz as the signal becomes instable at approximately this frequency. 'Instable' in this context means that the instrument is measuring the inertia of the clamp and is no longer sensitive to the sample. Figure 4.37 a) shows the Storage Modulus as a function of frequency for samples NC7, NC9, NC11 and NC13. The Storage Modulus increases with increasing frequency as well as with increasing clay content, which accords to results from DMA. Storage Moduli at 1 Hz are 6.3 kPa and 7.6 kPa for samples NC7 and NC9, respectively and 9.4 kPa and 14.3 kPa for sample NC11 and NC13, respectively. The rapid decrease observed for samples NC7, NC9 and NC11 at approximately 7 Hz are not further discussed as they are perhaps not related to the material but to a measurement error. The instrument’s manual suggests that measurements are not valid where the raw phase angel exceeds 175 °, as observed here. Although the relationship is not displayed here, the Loss Modulus increases with increasing clay content for all nanocomposite hydrogel samples considered. Furthermore, the Loss Modulus is independent of frequency. Figure 4.37 b) shows that the loss factor decreases with increasing frequency. Samples NC7, NC9 and NC11 exhibit no dependency between clay content and loss factor. Sample NC13 exhibits a slightly lower level in the loss factor than the other nanocomposite hydrogel samples. The values range between approximately 0.18 at 0.01 Hz and 0.09 at 6 Hz for samples NC7, NC9 and NC11. However, they range between 0.17 at 0.01 Hz and 0.07 at 6 Hz for sample NC13. Different than what is expected from stress relaxation experiments but according to results from DMA, no peak at around 0.003 Hz is present.

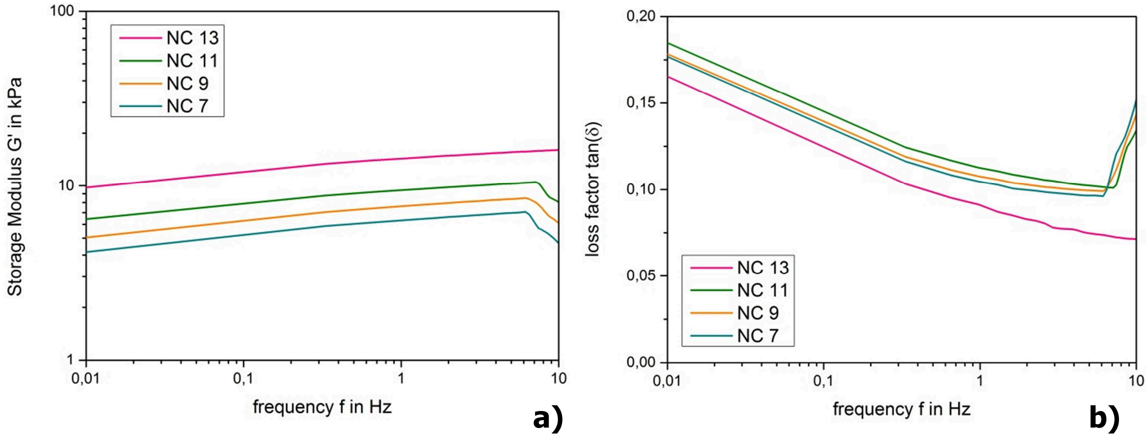

Figure 4.37: a) Storage Modulus and **b)** loss factor as a function of frequency for samples NC7, NC9, NC11, NC13.

Figure 4.38 a) shows the Storage Modulus as a function of frequency for sample NC9 and NC9_THICK as to discuss effects of sample thickness. The Storage Modulus for sample NC9_THICK exhibits higher values throughout the whole measured frequency range. At 1 Hz the Storage Modulus is 7.6 kPa for sample NC9 and 8.7 kPa for sample NC9_THICK, which correlates to results from all other tests performed in this study. The higher Storage Modulus of sample NC9_THICK is probably as a consequence of the sample preparation, which might yield slightly higher molecular weights for samples with a thickness of 3 mm than for samples with a thickness of 2 mm. As stated above the decrease at about 7 Hz for sample NC9 might be a measurement error. Except this feature, the curves for samples NC9 and NC9_THICK exhibit the same trend with a marginally stronger increase in the Storage Modulus with increasing frequency for sample NC9. Figure 4.38 b) shows the loss factor as a function of frequency for samples NC9 and NC9_THICK. Sample NC9_THICK presents a considerably lower loss factor. In contrast to DMA measurements no intersection between the curves at a frequency lower than 10 Hz is present.

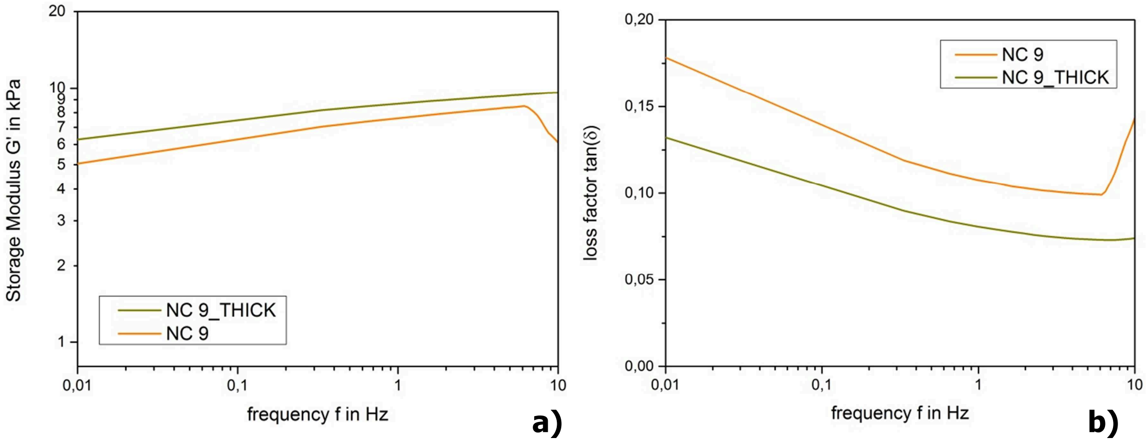

Figure 4.38: a) Storage Modulus and **b)** loss factor as a function of frequency for samples NC9, NC9_THICK.

Samples NC9 and OR9 are utilized to discuss effects of cross-linker type on results gained from rheometry-measurements. Figure 4.39 a) shows the Storage Modulus as a function of frequency for samples NC9 and OR9. The Storage Modulus of sample OR9 exhibits values that are approximately a magnitude higher than those for sample NC9. At 1 Hz, sample NC9 presents a Storage Modulus of 7.6 kPa while sample OR9 exhibits a Storage Modulus of 50.1 kPa. Further it is observed that while the Storage Modulus for all nanocomposite hydrogel samples increases with increasing frequency, the Storage Modulus for sample OR9 is independent of frequency. These results are consistent with findings from DMA measurements. Figure 4.39 b) shows the loss factor as a function of frequency for samples NC9 and OR9. The loss factor of sample OR9 is considerably lower than that of sample NC9. Sample OR9 exhibits a plateau at 0.023 between 0.01 Hz and approximately 0.04 Hz which is followed by an increase at higher frequencies. In contrast, the loss factor of sample NC9 lies at 0.178 at 0.01 Hz and decreases continuously with increasing frequency until approximately 7 Hz which is believed to be the end of the reliable measurement range. At 1 Hz the loss factor is 0.108 for sample NC9 and for sample OR9 0.031. The results are consistent with results gained from DMA measurements.

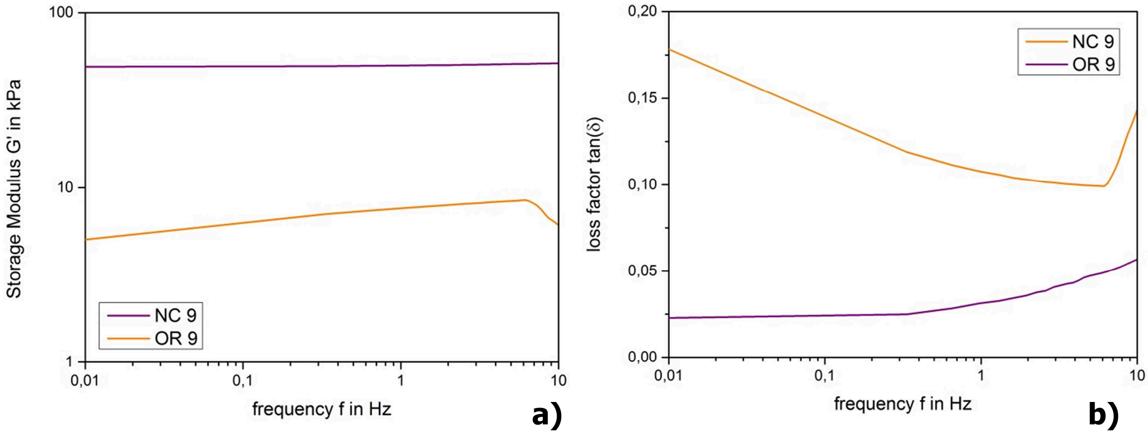

Figure 4.39: a) Storage Modulus and **b)** loss factor as a function of frequency for samples NC9, OR9.

4.4.4.2 Payne Effect

In order to compare the samples considered in this thesis to filled elastomers, strain-sweeps at 1 Hz are performed to study the Payne Effect. The Payne Effect is a characteristic feature typically exhibited by filled elastomers. The experimental characteristic observed in rheometry measurements is a steep decrease in the Storage Modulus accompanied by an increase in the Loss Modulus usually at low strains. Thus the following paragraphs describe curve progressions for Storage Modulus and Loss Modulus as a function of strain to determine whether the Payne Effect is present.

Figure 4.40 a) and b) show Storage Modulus and Loss Modulus, respectively, as a function of strain for samples NC7, NC9, NC11 and NC13. Both, Storage and Loss Moduli, are independent of strain to about 50 %. The downwards slope of the Storage Modulus close to 100 % cannot be interpreted as being real. It is observed during the measurements that at such high strains the specimen is ejected between the parallel plates of the rheometer. Thus, it is concluded that the Payne Effect is absent for samples NC7, NC9, NC11 and NC13. This means that these samples cannot be treated as filled elastomers, which is in agreement with results from low strain tensile testing and DMA measurements.

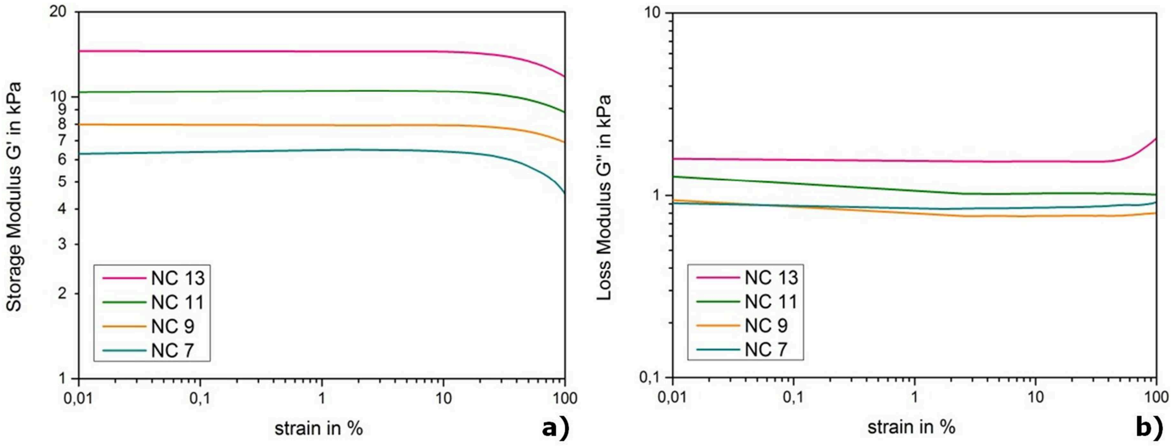

Figure 4.40: a) Storage Modulus and **b)** Loss Modulus as a function of strain for samples NC7, NC9, NC11, NC13.

Figure 4.41 a) and b) show the Storage Modulus and the Loss Modulus, respectively, as a function of strain for samples NC9 and NC9_THICK. The Storage Modulus exhibits a slightly higher level for sample NC9_THICK than for sample NC9. This result corresponds with previously discussed frequency sweeps. While sample NC9_THICK shows a Loss Modulus that is completely independent of strain, sample NC9 shows a marginal decrease in its Loss Modulus with increasing strain. In other respects no discrepancies are discernible between samples of different thickness. Hence, as for nanocomposite hydrogel samples with 2 mm thickness, the Payne Effect cannot be observed for sample NC9_THICK.

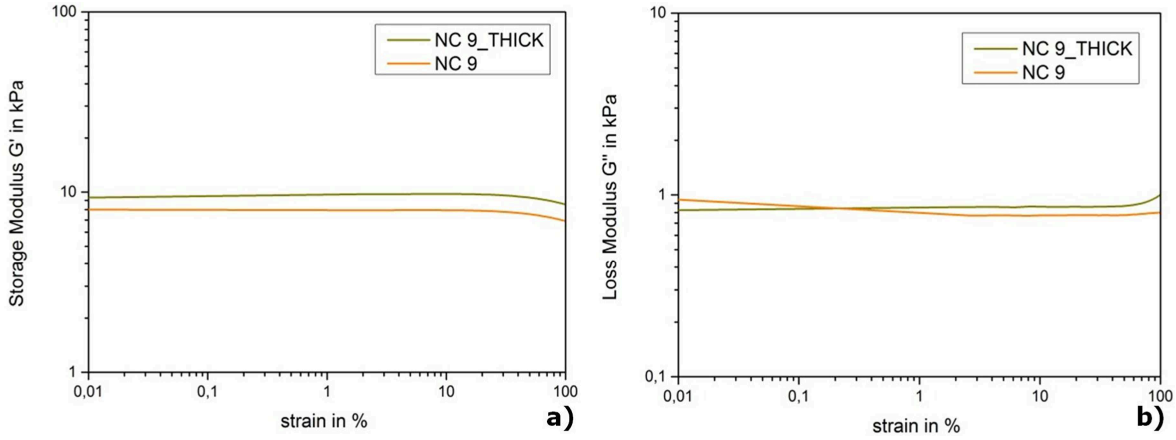

Figure 4.41: a) Storage Modulus and **b)** Loss Modulus as a function of strain for samples NC9, NC9_THICK.

Figure 4.42 a) and b) show Storage Modulus and Loss Modulus, respectively, as a function of strain for samples NC9 and OR9. In contrast to sample NC9, sample OR9 shows a manifest decrease in its Storage Modulus at about 10 % strain. This is accompanied by a considerable increase in the Loss Modulus that reaches a maximum at about 25 % strain. This characteristic is interpreted as the Payne Effect. Thus, organically cross-linked hydrogels as presented in this thesis are closely related to some filled elastomers.

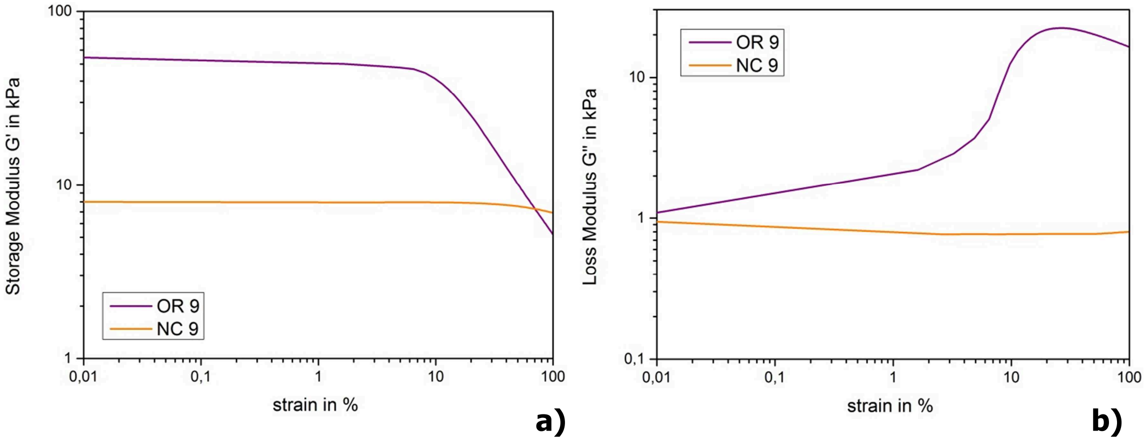

Figure 4.42: a) Storage Modulus and **b)** Loss Modulus as a function of strain for samples NC9, OR9.

4.5 Linking of Key Results and Classification of Nanocomposite Hydrogels

As described in literature, conventional/traditional hydrogels exhibit a brittle behaviour which limits employment of this material class in advanced applications such as biomedical application (e.g. artificial muscles). The poor mechanical properties of traditional hydrogels arise from the low functionality of organic cross-linkers that are used to prepare these hydrogels. Thus, these organic cross-linkers were substituted by clay which is an inorganic cross-linker with a presumably high functionality. Consequently, the mechanical behaviour of these so called nanocomposite hydrogels should be high in comparison to organically cross-linked hydrogels. In the present thesis, both traditional and nanocomposite hydrogels were successfully prepared and subsequently characterized extensively. In this subchapter the conjunction of key results shall be discussed. Moreover nanocomposite hydrogels shall be classified using an Ashby-Plot which compares fracture toughness and Storage Modulus.

From tensile testing stress-strain curves were determined for organically cross-linked as well as for nanocomposite hydrogels. Since for nanocomposite hydrogels (samples NC7, NC9, NC11, NC13, NC9_THICK) no fracture occurred within the crosshead travel, no quantitative evaluation for toughness could be obtained from the area under the stress-strain curve. However, a qualitative comparison of the stress-strain curves of nanocomposite hydrogels and the stress-strain curves of organically cross-linked hydrogels – where fracture occurred at approximately 10% – is possible. Thus it is concluded that the toughness of nanocomposite hydrogels is significantly higher than that of traditional hydrogels. It was hence assumed that also fracture toughness should be considerably higher for nanocomposite hydrogels. Since nanocomposite hydrogels prepared in this study exhibit an extraordinary high extensibility, common fracture toughness tests such as SENT (single edge notch tension) could not be carried out. However, fracture toughness of samples NC7, NC9, NC11 and NC13 could be determined by conducting pure shear tests. As the sample holder was especially designed for samples exhibiting a thickness of 2 mm, no samples of other thickness were tested. No valid test results could be obtained for organically cross-linked samples as they were too brittle to be tested. In contrast, samples NC7, NC9, NC11 and NC13 exhibit a high fracture toughness between 2400 and 6800 J/m^2. Hence it is verified that a significant improvement of fracture toughness was achieved by substituting the organic cross-linker by clay as inorganic cross-linker.

In order to understand the reasons for the high fracture toughness of nanocomposite hydrogels, viscoelastic characterization was carried out. This is because data from measurements regarding viscoelasticity allow studying the dissipation of energy in polymeric materials. Hence, step-cycle testing, stress relaxation experiments and dynamic-mechanical analysis as well as rheometry experiments were conducted. Step-cycle testing revealed that strain is split into an elastic fraction and a plastic fraction. At low to moderate strains (up to a total true strain of about 1.2 to 1.5) the ratio between the fractions is widely constant with an elastic fraction of approximately 75 % to 85 % of the total strain and a plastic fraction of the remaining 15 % to 25 %. At higher strains plastic deformation occurs most probably throughout the whole sample. Furthermore the shape of the stress-strain curves from step-cycle testing suggests the occurrence of hardening which is probably due to orientation of clay-particles. Stress relaxation experiments showed viscoelastic dissipation for nanocomposite hydrogels. The maximum of this dissipation was found at 290 s. Dynamic-mechanical analysis and rheometry experiments showed coherent results. One of the most important findings is the high level of the loss factor for nanocomposite hydrogels in comparison to organically cross-linked hydrogels. A high loss factor indicates the ability to absorb energy during dynamic loading.

Hence, investigations revealed different mechanisms contributing to the high fracture toughness of nanocomposite hydrogels. Firstly, blunting prevents expansion of existing cracks. Secondly plastic deformation provides absorption of energy. Thirdly, viscoelastic dissipation contributes to the superior fracture toughness. The improved mechanical characteristics of nanocomposite hydrogels in comparison to conventional hydrogels are a consequence of the multifunctionality of clay as well as the establishment of a very stable, physical, inorganic/organic, three-dimensional network.

As fracture toughness was determined and widely explained, the position of nanocomposite hydrogels in an Ashby-plot comparing Modulus and fracture toughness as shown in chapter 2 was investigated. Thus research regarding the Storage Modulus was conducted. As in this thesis four different methods are employed to determine the Storage Modulus, they shall now be compared. The first method utilizes the slope of the stress-strain curve and the relationship $E = 2 * G * (1 + \nu)$ commonly found to link the elastic constants E and G. The second method employs Simple Rubber Elasticity Theory by plotting stress as a function of $\left(\lambda - \frac{1}{\lambda^2}\right)$ and evaluating the slope. The third method utilizes DMA. The fourth method utilizes rheometry. However, when comparing the Moduli, one has to keep in mind that the latter two methods measure the dynamic Storage Modulus. Figure 4.43 compares the Moduli determined by the different methods. DMA and rheometry values are taken at 1 Hz. Moduli gained from tensile testing are considerably higher than those gained from dynamic measurements. Furthermore, DMA yields lower Moduli than rheometry. The differences between results from individual measurements tend to be larger for samples with high clay content. Additionally it is observed that sample OR9 exhibits particularly low values when tested by utilizing DMA.

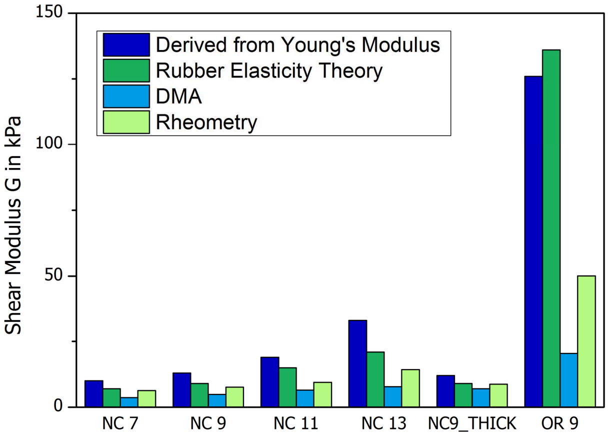

Figure 4.43: Comparison of Shear Modulus derived from different measurements and calculations.

Taking the different methods for the determination of the Storage Modulus as well as the dependency of both fracture toughness and Storage Modulus on the clay content into account, nanocomposite hydrogels as considered in this thesis shall be added to the

Ashby-plot that was already shown in chapter 2. This classification is displayed in Figure 4.44. It can be seen that the position of the considered nanocomposite hydrogels is unique. The improvement of hydrogels by use of clay as inorganic cross-linker regarding fracture toughness is evident. However, a higher Modulus might be desirable. The Ashby-Plot clearly depicts that a variation of clay content allows a regulation of fracture toughness of nanocomposite hydrogels in a broad range. This is especially notable since as mentioned above no other materials are existent in this region of the Ashby-Plot.

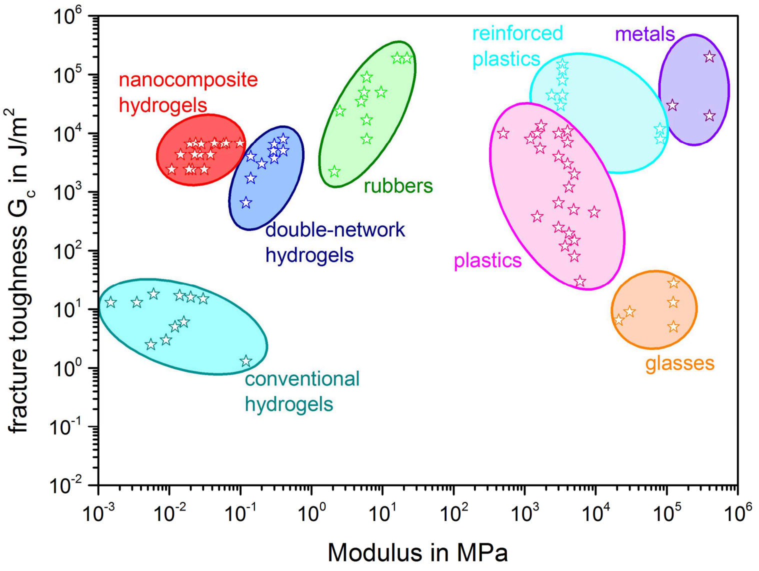

Figure 4.44: Ashby-Plot including the nanocomposite hydrogels studied in this thesis.

Furthermore, with the intention of describing the prepared organically cross-linked and nanocomposite hydrogel's material behaviour different theories were investigated. In order to do so, tensile testing was performed to a tensile strain of approximately 400 %. Subsequently, the resulting stress-strain curves were compared to the theories under consideration. Simple Rubber Elasticity Theory nearly ideally describes the material behaviour of organically cross-linked hydrogels. In contrast, nanocomposite hydrogels could neither be described by Simple Rubber Elasticity nor by Mooney-Rivlin Theory. Probably the complicated structure of the polymer/clay-network as well as to a large extent uninvestigated interactions between polymer and clay require more complex theoretical approaches to describe the material behaviour.

5 SUMMARY, CONCLUSIONS AND PROSPECTS

Hydrogels represent a material class of unique characteristics such as an extraordinary high capability of absorbing water and their transparency. Moreover they are often environmentally sensitive which makes them attractive for medical applications such as disposable diapers. Traditional/conventional hydrogels are chemically cross-linked by employing an organic cross-linker. Their utilization as advanced materials is limited as they are inherently brittle and fragile. In order to overcome problems attributed to low mechanical properties such as low tensile strength or low fracture toughness, nanocomposite hydrogels are developed. Hence, sophisticated applications such as artificial muscles should potentially be enabled. The enhancement of mechanical properties of nanocomposite hydrogels in comparison to conventional hydrogels originates in the substitution of the organic cross-linker by clay – an inorganic cross-linker – which results in the formation of a unique three-dimensional physical clay/polymer network structure. A major difference between the organic cross-linker and the clay is that the former exhibits a low functionality of four while the latter exhibits multifunctionality.

The present thesis is engaged in preparing nanocomposite hydrogels and characterizing them regarding their composition and microstructure as well as regarding their mechanical and viscoelastic properties. Special emphasis is laid on the effects of clay content and sample thickness of prepared nanocomposite hydrogels. Additionally, comparison between nanocomposite hydrogels and organically cross-linked hydrogels was performed.

Nanocomposite hydrogels were successfully prepared by employing Laponite XLS®, synthetic clay of type hectorite, and monomer N-N-Dimethylacrylamide and allowing in-situ free radical polymerization. Thus a physical network consisting of (inorganic) clay and (organic) polymer was created without intermolecular covalent bonds. Sample variables were clay content (7 mole%, 9 mole%, 11 mole% and 13 mole%) and sample thickness (1 mm, 2 mm, 3 mm). In addition, traditional hydrogels employing the organic cross-linker N,N′-methylenebis(acrylamide) and the same kind of monomer were prepared with a cross-linker content of 9 mole% and a thickness of 2 mm. Evaluation of visual and tactile assessment revealed that the developed sample preparation process was inadequate for samples with a thickness of 1 mm. The reason is probably an incomplete polymerization process as evidenced by infrared spectroscopy and tensile extension-at-break. All other hydrogels exhibited a high transparency and only few bubbles that were smaller than 1 mm in diameter. As determined by thermo-gravimetric analysis, the water content was approximately 75 % by weight. The exfoliation of clay, which is crucial for the establishment of the physical network, was confirmed by employing transmission electron microscopy and X-ray diffraction. In all nanocomposite hydrogels, clay particles could be identified. They exhibited an elliptical shape with dimensions of 20 to 30 nm in length and 1 to 1.5 nm in thickness that are in good agreement with the disk-shape geometry as described in literature.

Fourier-transformation infrared spectroscopy resulted in similar spectra for all nanocomposite hydrogels with the exception of the 1 mm thick sample. Thus, it was concluded that the polymerization process lead to the formation of the same functional groups regardless of clay content. Furthermore, no difference between samples of 2 mm thickness and 3 mm thickness was perceived. Absorption bands could be identified and either be ascribed to the clay or to the monomer. The spectrum of the organically cross-linked sample contained the absorption bands that were ascribed to the monomer.

Low strain measurements were performed to characterize mechanical properties such as the Elastic Constants and the functional correlation of tensile stress and tensile strain of nanocomposite hydrogels and traditional hydrogels. Nanocomposite hydrogels with a sample thickness of 2 mm and 3 mm exhibited good mechanical properties. No fracture occurred within the crosshead's travel limit. The strain-at-break was hence higher than 1250 % for all samples. Increasing clay content led to increasing Young's Modulus from about 30 kPa for the nanocomposite hydrogel with the lowest clay content to about 100 kPa for the nanocomposite hydrogel with the highest clay content. The number of network chains between cross-links per unit volume increased analogously from $7.5 \cdot 10^{17}$ cm^{-3} for the nanocomposite hydrogel with the lowest clay content to about $1.9 \cdot 10^{18}$ cm^{-3} for the hydrogel with the highest clay content. Data were compared to the Simple Rubber Elasticity Theory and the Mooney-Rivlin Theory. None of these theories ideally describes the material behaviour of nanocomposite hydrogels as considered in this study. The tensile curves are consistent with those for filled elastomers where the filler forms a continuous network. The traditional hydrogel sample exhibited a comparatively brittle behaviour which became evident through a strain-at-break of approximately 10 %. Its material behaviour can readily be described by the Rubber Elasticity Theory.

Fracture toughness was determined by employing the pure shear test approach. Special grips were designed. This was necessary to overcome the problem of clamping which is inherent due to the required specimen geometry (small initial length, no shoulders or similar for mounting) for this test. To the knowledge of the author, fracture toughness has not yet been performed on this type of nanocomposite hydrogel but only been estimated by calculating the area under the stress-strain-curve. Extraordinarily high fracture toughness of 2400 J/m^2 for the nanocomposite hydrogel with the lowest clay content to 6800 J/m^2 for the nanocomposite hydrogel with the highest clay content were determined. Hence, nanocomposite hydrogels as considered in this thesis can quickly dissipate large amounts of energy. One dissipation mechanism that was observed during fracture toughness tests was blunting of the crack. In order to detect further dissipation mechanisms, viscoelastic properties were characterised. Hence, step cycle testing, stress relaxation experiments and dynamic mechanical analysis as well as rheometry experiments were conducted.

Step cycle testing firstly revealed that for true strains up to 120 % to 150 % the ratio between elastic and plastic strain remains constant. However, at a certain strain, plastic strain almost completely dominates the deformation behaviour. Therefore it is concluded that the plastic deformation is presumably large in the whole sample and also close to adjacencies of a crack tip if a crack is present. This phenomenon probably contributes to the high fracture toughness of nanocomposite hydrogels. Furthermore, it is concluded from step cycle testing that at high strains clay platelets probably orientate and hence yield hardening of the samples.

Stress relaxation experiments were evaluated by fitting a two-element Kelvin model. It is deduced that relaxation times are independent of clay content. The time at which maximal viscoelastic dissipation occurs is equivalent to the stress relaxation time and lies at 290 s. Since the relaxation time is similar to the time necessary to rupture samples in fracture toughness tests viscoelastic dissipation accounts for high fracture energies. Samples with a thickness of 3 mm yield a longer relaxation time of 730 s than those with a thickness of 2 mm. This is attributed to the sample preparation that probably yields slightly longer polymer chains for samples with a thickness of 3 mm.

Dynamic mechanical analysis and rheometry experiments were performed to obtain curve progressions of the Storage Modulus, the Loss Modulus and the loss factor as a function of frequency. Storage Moduli of nanocomposite hydrogels increase with increasing clay content as well as with increasing frequency. In general the Storage Modulus is found around 10 kPa. In contrast, the Storage Modulus of organically cross-linked hydrogels is independent of frequency and lies at approximately 20 to 50 kPa. The loss factor of nanocomposite hydrogels ranges between 0.18 and 0.07 which is high in comparison to organically cross-linked hydrogels where the loss factor ranges from 0.02 to about 0.11. The loss factor is a measure for the ability to dissipate energy. Hence, it is concluded that toughness of nanocomposite hydrogels is probably significantly higher than toughness of traditional hydrogels. This is in good agreement with fracture toughness tests which revealed high fracture energies of 2400 J/m^2 to 6800 J/m^2 for nanocomposite hydrogels but could not be performed on traditional hydrogels due to their fragility.

This study further attempted to compare nanocomposite hydrogels' and traditional hydrogels' material behaviour to that of filled elastomers. Hence, the Payne Effect and the Mullins-Effect, both characteristic effects occurring in filled elastomers, were studied. The Mullins-Effect which was surveyed in step cycle testing was present for nanocomposite hydrogels for low and moderate strains. The presence of the Payne Effect was examined employing rheometry. As the Payne Effect was not discernible for nanocomposite hydrogels but for traditional hydrogels, it is concluded that the material behaviour of the latter is presumably similar to filled elastomers. However, nanocomposite hydrogels can probably not be classified as similar to filled elastomers.

Concisely, this study successfully prepared and characterized microstructural, mechanical and viscoelastic properties of nanocomposite hydrogels. High fracture toughness was found to originate in three major dissipation mechanisms: blunting, plastic deformation and viscoelastic dissipation. Rounded off with a comprehensive literature review it is concluded that nanocomposite hydrogels are a highly attractive material class with a high potential for future applications such as artificial muscles, synthetic mammal tissue and drug release agents.

An interesting potential for future research could be the examination of orientation of clay particles at high strains as this is probably a reason for strain-hardening in cyclic loading. Further the interaction between clay and polymer network could be explored and described in more detail. Additionally, optimization of the preparation procedure is desirable in order to allow the production of high quality samples with small dimensions such as a low thickness. Furthermore, the introduction of a second network into nanocomposite hydrogels considered in this study might yield a nanocomposite double-network hydrogel with attractive properties. Presently, step cycle tests with smaller steps of 2 % are performed to analyse the splitting of total strain in elastic and plastic fractions in more detail.

6 LITERATURE

American Museum of Natural History (2009). http://www.amnh.org/learn-teach/young-naturalist-awards, 24/06/2013.

Abdurrahmanoglu S., et al. (2008). "Equilibrium swelling behavior and elastic properties of polymer–clay nanocomposite hydrogels", Journal of Applied Polymer Science 109, 3714-3724.

aerogel.org (2006). www.aerogel.org, 12/07/2013.

Akagi Y., et al. (2011). "Examination of the theories of rubber elasticity using an ideal polymer network", Macromolecules 44, 5817-5821.

Akashi R., et al. (2002). "Polymer gel light-modulation materials imitating pigment cells", Advanced Materials 14, 1808-1811.

Almdal K., et al. (1993). "What is a 'gel'?", Makromolekulare Chemie. Macromolecular Symposia 76, 49-51.

Anderson T.L. (2005). "Fracture Mechanics: Fundamentals and Applications", CRC Press, Boca Raton.

Ashby M., et al. (2007). "Materials - Engineering, Science, Processing and Design", Elsevier Ltd., Oxford.

ASM International (2003). "Characterization and Failure Analysis of Plastics".

Bueche F. (1960). "Molecular basis for the mullins effect", Journal of Applied Polymer Science 4, 107-114.

Bueche F., Halpin, J.C. (1964). "Molecular theory for the tensile strength of gum elastomers", Journal of Applied Physics 35, 36-41.

Carlsson L., et al. (2010). "Nano-hybrid self-crosslinked PDMA/silica hydrogels", Soft Matter 6, 3619-3631.

Carrillo J.M.Y., et al. (2013). "Nonlinear elasticity: From single chain to networks and gels", Macromolecules 46, 3679-3692.

NDT Education Resource Center (2012). http://www.ndt-ed.org/EducationResources/CommunityCollege/Materials/Mechanical/Toughness.htm, 13/03/2013.

Dai H., et al. (2006). "A temperature-responsive copolymer hydrogel in controlled drug delivery", Macromolecules 39, 6584-6589.

Das D., et al. (2012). "Gel-nanocomposites: materials with promising applications", Soft Matter 8, 2348-2365.

Eichinger B.E. (1990). "Elasticity theory. 6. Molecular theory of the Mooney-Rivlin equation and beyond", Macromolecules 23, 4270-4281.

Fei R., et al. (2013). "Ultra-strong thermoresponsive double network hydrogels", Soft Matter 9, 2912-2919.

Flory P.J. (1984). "Network topology and the theory of rubber elasticity", British Polymer Journal 17, 96-102.

Flory P.J. (1953). "Principles of Polymer Chemistry", Cornell University Press, New York.

Gao T., et al. (2011). "Characterization the relationship between rheology behavior and molecular weight of natural rubber with different protein content", Advanced Materials Research 337, 285 - 288.

Gdoutos E.E., et al. (2003). "Fracture Mechanics of Rubber", Facta Universitatis 3, 13.

Gent A.N., Wang, C. (1991). "Fracture mechanics and cavitation in rubber-like solids", J Mater Sci 26, 3392-3395.

Gong J.P., et al. (2003). "Double-network hydrogels with extremely high mechanical strength", Advanced Materials 15, 1155-1158.

Greensmith H.W., Thomas, A.G. (1955). "Rupture of rubber. III. Determination of tear properties", Journal of Polymer Science 18, 189-200.

Grellmann W., Seidler, S. (2007), Fracture Toughness Measurements in Engineering Plastics, in: G. Wolfgang, S. Sabine (Eds.) Polymer Testing, Carl Hanser Verlag GmbH & Co. KG, 231-283.

Griffith A.A. (1921). "The Phenomena of Rupture and Flow in Solids", Philosophical Transactions of the Royal Society of London. Series A, Containing Papers of a Mathematical or Physical Character 221, 163-198.

Guenther M., et al. (2007). "Chemical sensors based on multiresponsive block copolymer hydrogels", Sensors and Actuators, B: Chemical 126, 97-106.

Halary J.-L., et al. (2010). "Polymer Materials, Macroscopic Properties and Molecular Interpretations", Wiley, Hoboken.

Hao J., Weiss, R.A. (2013). "Mechanical behavior of hybrid hydrogels composed of a physical and a chemical network", Polymer (United Kingdom) 54, 2174-2182.

Hao J., Weiss, R.A. (2011). "Viscoelastic and mechanical behavior of hydrophobically modified hydrogels", Macromolecules 44, 9390-9398.

Haraguchi K. (2007). "Nanocomposite Gels: New Advanced Functional Soft Materials", Macromolecular Symposia 256, 120-130.

Haraguchi K., et al. (2003). "Compositional effects on mechanical properties of nanocomposite hydrogels composed of poly(N,N-dimethylacrylamide) and clay", Macromolecules 36, 5732-5741.

Haraguchi K., Li, H.-J. (2006). "Mechanical Properties and Structure of Polymer−Clay Nanocomposite Gels with High Clay Content", Macromolecules 39, 1898-1905.

Haraguchi K., et al. (2005). "Mechanism of Forming Organic/Inorganic Network Structures during In-situ Free-Radical Polymerization in PNIPA−Clay Nanocomposite Hydrogels", Macromolecules 38, 3482-3490.

Haraguchi K., Takehisa, T. (2002). "Nanocomposite hydrogels: A unique organic-inorganic network structure with extraordinary mechanical, optical, and swelling/De-swelling properties", Advanced Materials 14, 1120-1124.

Haraguchi K., et al. (2006). "Control of Cell Cultivation and Cell Sheet Detachment on the Surface of Polymer/Clay Nanocomposite Hydrogels", Biomacromolecules 7, 3267-3275.

Haraguchi K., et al. (2002). "Effects of Clay Content on the Properties of Nanocomposite Hydrogels Composed of Poly(N-isopropylacrylamide) and Clay", Macromolecules 35, 10162-10171.

Haraguchi K., et al. (2011). "Self-healing in Nanocomposite Hydrogels", Macromolecular Rapid Communications 32, 1253-1258.

Haraguchi K., et al. (2010). "Molecular Characteristics of Poly(N-isopropylacrylamide) Separated from Nanocomposite Gels by Removal of Clay from the Polymer/Clay Network", Macromolecular Rapid Communications 31, 718-723.

Hattori T., et al. (2013). "A fluorescence study on the local environment of hydrogels: Double-network hydrogels having extraordinarily high mechanical strength and its constituent single-network hydrogels", Chemical Physics 172-177.

He C., et al. (2013). "Tough and super-resilient hydrogels synthesized by using peroxidized polymer chains as polyfunctional initiating and cross-linking centers", Soft Matter 9, 2837-2844.

Hellweg T., et al. (2000). "Colloidal crystals made of poly(N-isopropylacrylamide) microgel particles", Colloid and Polymer Science 278, 972-978.

HelvacIoğlu E., et al. (2011). "High strength poly(acrylamide)-clay hydrogels", Journal of Polymer Research 18, 2341-2350.

Hoemann C.D., et al. (2005). "Tissue engineering of cartilage using an injectable and adhesive chitosan-based cell-delivery vehicle", Osteoarthritis and Cartilage 13, 318-329.

Hoffman A.S. (2002). "Hydrogels for biomedical applications", Advanced Drug Delivery Reviews 54, 3-12.

Hong K., et al. (2004). "A model treating tensile deformation of semicrystalline polymers: Quasi-static stress-strain relationship and viscous stress determined for a sample of polyethylene", Macromolecules 37, 10165-10173.

Horgan C.O., Saccomandi, G. (2006). "Phenomenological hyperelastic strain-stiffening constitutive models for rubber", Rubber Chemistry and Technology 79, 152-169.

Hu X., et al. (2009). "Preferential Adsorption of Poly(ethylene glycol) on Hectorite Clay and Effects on Poly(N-isopropylacrylamide)/Hectorite Nanocomposite Hydrogels", Langmuir 26, 4233-4238.

Huang G., et al. (2004). "Controlled drug release from hydrogel nanoparticle networks", Journal of Controlled Release 94, 303-311.

Huang T., et al. (2007). "A Novel Hydrogel with High Mechanical Strength: A Macromolecular Microsphere Composite Hydrogel", Advanced Materials 19, 1622-1626.

Hui C.Y., et al. (2003). "Crack blunting and the strength of soft elastic solids", Proceedings of the Royal Society A: Mathematical, Physical and Engineering Sciences 459, 1489-1516.

Kasgoz H., et al. (2012). "Structurally enhanced hydrogel nanocomposites with improved swelling and mechanical properties", Journal of Macromolecular Science, Part A: Pure and Applied Chemistry 49, 92-99.

Kroon M., et al. (1998). "Structure and Formation of a Gel of Colloidal Disks", International Journal of Thermophysics 19, 887-894.

Lake G.J., Thomas, A.G. (1967). "The Strength of Highly Elastic Materials", Proceedings of the Royal Society of London. Series A. Mathematical and Physical Sciences 300, 108-119.

Lee W.F., Fu, Y.T. (2003). "Effect of montmorillonite on the swelling behavior and drug-release behavior of nanocomposite hydrogels", Journal of Applied Polymer Science 89, 3652-3660.

University of South Carolina (2000). http://faculty.uscupstate.edu/llever/, 27/03/2013.

Li P., et al. (2009a). "Improved mechanical and swelling behavior of the composite hydrogels prepared by ionic monomer and acid-activated Laponite", Applied Clay Science 46, 414-417.

Li P., et al. (2009b). "Poly(acrylamide/laponite) nanocomposite hydrogels: Swelling and cationic dye adsorption properties", Journal of Applied Polymer Science 111, 1786-1798.

Li Z., et al. (2013). "Preparation and characterization of pH- and temperature-responsive nanocomposite double network hydrogels", Materials Science and Engineering C 33, 1951-1957.

Lillie M.A., Gosline, J.M. (2002). "The viscoelastic basis for the tensile strength of elastin", International Journal of Biological Macromolecules 30, 119-127.

Lin H.-R. (2001). "Solution polymerization of acrylamide using potassium persulfate as an initiator: kinetic studies, temperature and pH dependence", European Polymer Journal 37, 1507-1510.

Linnes M.P., et al. (2007). "A fibrinogen-based precision microporous scaffold for tissue engineering", Biomaterials 28, 5298-5306.

Liu Y., et al. (2006). "High clay content nanocomposite hydrogels with surprising mechanical strength and interesting deswelling kinetics", Polymer 47, 1-5.

Lupi F.R., et al. (2013). "A rheological characterisation of an olive oil/fatty alcohols organogel", Food Research International 51, 510-517.

M. F. Ashby, Jones, D.R.H. (2012). "Engineering Materials 1, An Introduction to Properties, Applications, and Design", Elsevier Ltd. , Oxford.

Ma J., et al. (2008). "Preparation and characterization of porous poly (N-isopropylacrylamide) /clay nanocomposite hydrogels", Polymer Bulletin 61, 593-602.

Maatar W., et al. (2013). "Cellulose based organogel as an adsorbent for dissolved organic compounds", Industrial Crops and Products 49, 33-42.

Mark J.E., et al. (2013). "The Science and Technology of Rubber", Elsevier Science, Amsterdam.

Meissner B., Matějka, L. (2000). "Description of the tensile stress–strain behavior of filler-reinforced rubber-like networks using a Langevin-theory-based approach. Part I", Polymer 41, 7749-7760.

Mielenz R.C., et al. (1953), in: Second National Conference on Clays and Clay Minerals, Columbia, Missouri, 285-314.

Miyaji J., The Yokohama Rubber Co., Ltd., et al. (2001). "Rubber composition for laminate having improved anti-fracture characteristics", EP1160280 A1.

Naficy S., et al. (2011). "Progress Toward Robust Polymer Hydrogels", Australian Journal of Chemistry 64, 1007-1025.

Okay O. (2010), General Properties of Hydrogels, in: G. Gerlach, K.-F. Arndt (Eds.) Hydrogel Sensors and Actuators, Springer Berlin Heidelberg, 1-14.

Okay O., Oppermann, W. (2007). "Polyacrylamide-clay nanocomposite hydrogels: Rheological and light scattering characterization", Macromolecules 40, 3378-3387.

Overstreet D.J., et al. (2013). "Temperature-responsive graft copolymer hydrogels for controlled swelling and drug delivery", Soft Materials 11, 294-304.

Ren H.Y., et al. (2011). "Characteristic swelling-deswelling of polymer/clay nanocomposite gels", Macromolecules 44, 8516-8526.

Rickaby S.R., Scott, N.H. (2013). "A cyclic stress softening model for the Mullins effect", International Journal of Solids and Structures 50, 111-120.

Rivlin R.S., Thomas, A.G. (1953). "Rupture of rubber. I. Characteristic energy for tearing", Journal of Polymer Science 10, 291-318.

Seitz M.E., et al. (2009). "Fracture and large strain behavior of self-assembled triblock copolymer gels", Soft Matter 5, 447-456.

Sharifi S., et al. (2012). "Biodegradable nanocomposite hydrogel structures with enhanced mechanical properties prepared by photo-crosslinking solutions of poly(trimethylene carbonate)-poly(ethylene glycol)-poly(trimethylene carbonate) macromonomers and nanoclay particles", Acta Biomaterialia 8, 4233-4243.

Shi Z., et al. (2011). "Synthesis and properties of a novel conducting hydrogel with enhanced mechanical properties", 332-334, 1714-1717.

Shibayama M. (1998). "Spatial inhomogeneity and dynamic fluctuations of polymer gels", Macromolecular Chemistry and Physics 199, 1-30.

Slugovc C. (2011). "Polymerisationsmechanismen", TU Graz, Institute for Chemistry and Technology of Materials.

Smeltz K.C., Dyer, E. (1952). "The Effect of Oxygen on the Polymerization of Acrylonitrile1", Journal of the American Chemical Society 74, 623-628.

Smith T.L. (1967). "Large deformation tensile properties of elastomers. I. Temperature dependence of c1 and c2 in the mooney-rivlin equation", Journal of Polymer Science Part C: Polymer Symposia 16, 841-858.

Sun J.Y., et al. (2012). "Highly stretchable and tough hydrogels", Nature 489, 133-136.

Tanaka Y., et al. (2005). "Determination of Fracture Energy of High Strength Double Network Hydrogels", The Journal of Physical Chemistry B 109, 11559-11562.

Treloar L.R.G. (2005). "The Physics of Rubber Elasticity", Oxford.

Wang X., et al. (2009). "Method for clay exfoliation, compositions therefore, and modified rubber containing same", 7,576,155 B2.

Wang Y., et al. (2011). "PDMAA/Clay nanocomposite hydrogels based on two different initiations", Colloids and Surfaces A: Physicochemical and Engineering Aspects 390, 20-24.

Wu D.Q., et al. (2008). "Biodegradable and pH-sensitive hydrogels for cell encapsulation and controlled drug release", Biomacromolecules 9, 1155-1162.

Xiang Y., et al. (2006). "A new polymer/clay nano-composite hydrogel with improved response rate and tensile mechanical properties", European Polymer Journal 42, 2125-2132.

Xiong L., et al. (2008). "Network chain density and relaxation of in situ synthesized polyacrylamide/hectorite clay nanocomposite hydrogels with ultrahigh tensibility", Polymer 49, 5064-5071.

Yin H., et al. (2013). "Double network hydrogels from polyzwitterions: high mechanical strength and excellent anti-biofouling properties", Journal of Materials Chemistry B 1, 3685-3693.

Zhang Q., et al. (2009). "Preparation and performance of nanocomposite hydrogels based on different clay", Applied Clay Science 46, 346-350.

Zhu M., et al. (2006). "A novel highly resilient nanocomposite hydrogel with low hysteresis and ultrahigh elongation", Macromolecular Rapid Communications 27, 1023-1028.

Zhu M., et al. (2010). "High tensibility and pH-responsive swelling of nanocomposite hydrogels containing the positively chargeable 2-(dimethylamino)ethyl methacrylate monomer", Reactive and Functional Polymers 70, 267-271.

7 APPENDIX

7.1 Number of Network Chains between Cross-links per Unit Volume

The following paragraphs outline the calculation of the number of network chains between cross-links per unit volume for exemplary sample NC11. A straight line is fitted in the range of ($1 < \lambda < 4$) in the Rubber Theory Plot (correlation coefficient larger than 0.999). The slope is found to be 7.15 kpa. Equation 7.1 follows from Eq. 2.2 and 2.4. Hence, $\mathrm{k} * \mathrm{n} * \mathrm{T}$ equals the slope.

$$\sigma = \mathrm{k} * \mathrm{n} * \mathrm{T} * (\lambda - \frac{1}{\lambda^2}) \tag{7.1}$$

where σ is the tensile stress, k is the Boltzmann Constant, n is the number of network chains per unit volume, T is the absolute temperature and λ is the elongation ratio.

With $k = 1.3806 * 10^{-23}\, J/K$ and $T = 298.15\, K$ n can be calculated as follows:

$$n = \frac{0.00715}{1.3806 * 10^{-23} * 298.15} = 1.738 * 10^{18}\, network\ chains\ per\ cm^3$$

7.2 Determination of Molecular Weight of Polymer Chains between Cross-links

The following paragraphs outline the theoretical and experimental calculation of the molecular weight of polymer chains between cross-links in details for samples NC9 and OR9.

The experimental molecular weight of polymer chains between cross-links M_c is determined employing Eq. 3.2. The volume fraction of polymer φ for nanocomposite hydrogels is estimated as given in Eq. 7.2. The mass of polymer $m_{polymer}$ is assumed to equal the mass of monomer $m_{monomer}$.

$$\varphi = \frac{m_{polymer}}{m_{polymer} + m_{water} + m_{cross-linker}} \tag{7.2}$$

where m_{water} and $m_{cross-linker}$ are the mass of water and cross-linker, respectively. From synthesis it is know that:

$$m_{polymer} \approx m_{monomer} = V_{monomer} * \rho_{monomer} = 4.5\, mL * 0.962 \frac{g}{mL} = 4.329\, g$$

where $V_{monomer}$ and $\rho_{monomer}$ are volume and density of monomer, respectively.

$m_{water} = 21.5\ g$

$m_{clay} = 1.47492\ g$

$m_{organic\ cross-linker} = 0.298319\ g$

$$\varphi_{NC9} = \frac{4.329}{4.329 + 21.5 + 1.47492} = 0{,}158$$

$$\varphi_{OR9} = \frac{4.329}{4.329 + 21.5 + 0.298319} = 0.167$$

where m_{clay} and $m_{organic\ cross-linker}$ are the mass of clay and organic cross-linker, respectively, and φ_{NC9} and φ_{OR9} are the volume fractions of polymer for samples NC9 and OR9, respectively.

The density of the gel ρ is estimated to be $1\ g/mL$ as the main component is water. Avogadro's constant N_A is approximated with $6.022 * 10^{23} mole^{-1}$. The number of network chains is gained from experiment with an exemplary calculation given above. Hence, M_c can be calculated for samples NC9 (M_{NC9}) and OR9 (M_{OR9}) as follows:

$$M_{NC9} = \frac{1 * 0.158 * 6.022 * 10^{23}}{1.1 * 10^{18}} = 86798\ g/mole$$

$$M_{NC9} = \frac{1 * 0.167 * 6.022 * 10^{23}}{3.3 * 10^{19}} = 3024\ g/mole$$

The theoretical molecular weight of polymer chains between cross-links M_c is determined employing Eq. 3.3.

The amount of substance $x_{cross-linker}$ is equal for NC9 and OR9 and defined as $9 * 10^{-2}\ moles\ per\ 1\ L\ water$. The amount of substance of monomer $x_{monomer}$ can be calculated as follows with a molecular weight of the monomer of $99.13\ g/mole$, $m_{monomer} = 4.329g$ and $m_{water} = 21.5g$ as shown previously.

$$x_{cross-linker} = \frac{4.329 * 1000}{21.5} * \frac{1}{99.13} = 2.03 = 2.03 * 10^{2}\ moles\ per\ 1\ L\ water$$

Hence, the theoretical molecular weight between cross-links can be calculated as follows:

$$M_{NC9} = M_{OR9} = \frac{1}{2} * \frac{x_{monomer}}{x_{cross-linker}} * mm_{monomer} = \frac{1}{2} * \frac{2.03 * 10^{2}}{9} * 99.13 = 1119\ g/mole$$